Reconstruction of cosmic-ray intensity in the past from measurements of radiocarbon in tree rings

樹木年輪中放射性炭素14濃度測定による過去の宇宙線強度の復元

Fusa Miyake

三宅　芙沙

Doctoral Thesis

Nagoya University

Abstract

Measurements of cosmogenic nuclides, which are radioisotopes produced by cosmic rays, can provide important information regarding extraterrestrial high-energy events. Until now, ^{14}C in tree rings as well as ^{10}Be and nitrate in ice cores have been used for this purpose, and some evidence of high-energy events has been reported. However, no clear signal has been found by the ^{14}C method at a time resolution of one year or better, comparable to the time scale of high-energy astrophysical events. Here we present ^{14}C measurements in annual rings of Japanese cedar trees from AD 750 to 820, with 1- and 2-year resolutions. We found a rapid increase of about 12‰ in the ^{14}C content from AD 774 to 775. This value is about 20 times larger than the change due to ordinary solar modulation. The short-term increase of radioactive nuclide production were also found in tree rings of Germany and New Zealand. Therefore, it is possible that this increase was recorded all over the world due to a rapid increase in the cosmic ray intensity in AD 775.

Although the follow up studies showed that the cause of this event can be explained by a large solar proton event (SPE) or a short gamma-ray burst, a more detailed discussion of the cause is difficult because the rate of occurrence of such rapid ^{14}C events remains unknown. After that we have measured the ^{14}C content in Japanese cedar and cypress tree-rings during extended periods from AD 550 to 1100, and discovered a second rapid increase of ^{14}C content from AD 993 to 994. The ^{10}Be flux in the Antarctic ice core shows peaks corresponding to these two ^{14}C events. The proportions of flux increase ($^{14}C/^{10}Be$) of the two events are consistent with each other. Therefore, it is highly possible that these events have the same origin. Considering the occurrence rate of ^{14}C increase events, solar activity is a plausible cause of the ^{14}C increase events.

Contents

Chapter 1

Introduction

Carbon-14 is produced in the Earth's atmosphere by nuclear interactions with galactic cosmic rays, most of which are charged particles. The flux of cosmic rays to the Earth is modulated by the solar magnetic activity and the geomagnetic field. Radiocarbon oxidizes in the atmosphere to form $^{14}CO_2$ and is taken up by trees as part of the global carbon cycle. As ^{14}C is a radioisotope with a half-life of 5730 years, the ^{14}C content in tree rings provides a record of cosmic ray intensity and solar activity over a few tens of millennia.

While the solar magnetic activity and the geomagnetic field modulate the cosmic ray background, extra-terrestrial high-energy phenomena such as supernova explosions and large solar proton events can produce a large number of cosmic rays all at once.

In the 1960s, *Konstantinov and Kocharov* [1965] proposed an idea that gamma-rays from a supernova (SN) explosion can produce a detectable amount of ^{14}C. Accurately dated tree rings constitute a natural archive of hard gamma-rays arriving in the Earth's atmosphere. *Damon et al.* [1995, 2000] claimed to have found evidence of a supernova explosion in the ^{14}C content of tree rings around AD 1006, which might correspond to the supernova SN1006, one of the nearest to the Earth. There exist some written historical records of this event, mainly from East Asia [*Storm*, 2004; *Burrows*, 2000]. However *Menjo et al.* [2006] claimed that the increase of ^{14}C content around AD 1006 is not prominent, and could be explained by normal solar activity. Similarly, yearly ^{14}C data in recorded years of other supernova explosions in our galaxy (SN1054, SN1572, and SN1604) did not show the evidence of supernovae [*Damon et al.*, 2000; *Menjo et al.* 2006; *Stuiver et al.* 1998b]. Therefore, in order to detect an increase of ^{14}C content due to a supernova explosion, the total energy flux of gamma-rays entering earth's atmosphere should be larger than that of these supernovae.

A solar particle burst may also produce a detectable increase in ^{14}C content. Major solar eruptions are accompanied by massive ejections of protons (this is called a Solar Proton Event, or SPE). During an SPE the flux of low-energy particles near the Earth may increase by orders of magnitude, but it has been found that typical SPEs have little effect on the ^{14}C content of the atmosphere [*Castagnoli*, 1980]. *Usoskin et al.* [2006] computed the changes in ^{14}C content that could be caused by SPEs identified in ^{10}Be data in the ice core during the last 500 years, and concluded that no SPE events had produced a detectable change in ^{14}C content. Therefore, to produce a detectable

increase of ^{14}C content, the total energy in protons entering the Earth's atmosphere should be greater than that produced by the largest flare in the recorded history. In fact, very large, energetic "super flares" have been detected on normal solar-type stars [*Schaefer et al.* 2000; *Maehara et al.* 2012]. Therefore it has been discussed whether super flares could occur on our Sun.

Some studies show the past high-energy events, which are detected by nitrate ion (NO_3^-) in ice cores. Nitrate is produced by ionization process, and it is proposed that high energy cosmic-rays also produce nitrate. Nitrate in ice cores have been used for searching for high energy events. *Rood et al.* [1979] initially suggested the possibility that nitrate profile could detect some historical supernovae, and *Motizuki et al.* [2009] claimed the existence of nitrate ion spikes in Antarctic ice core corresponds to SN1006 and SN1054. Also *McCracken et al.* [2001] reported some SPEs including the largest Carrington flare in AD 1859 can be identified by nitrate spikes in Greenland ice core (however, the following studies show these spikes in Greenland are occurred by biomass burning plumes [*Wolff et al.* 2012]). Although some other evidence of high-energy events has been reported [Brakenridge 2011; LaViolette 2011], no clear signal has been found by the ^{14}C method at a resolution of one year or better, comparable to the time scale of high-energy astrophysical events.

If either type of high-energy phenomenon occurred in the past, it might affect the Earth. For example, it is said that a mass extinction can be explained by a gamma-ray burst in our galaxy [*Mellot et al.* 2001]. If a super flare occurred on our Sun, it might have had an adverse effect on humans [*Schaefer et al.* 2000]. So searching for past high-energy events of this nature is important in terms of understanding the relationship between high-energy phenomena and human lives.

In order to search for such high-energy phenomena that created a rapid ^{14}C content increase within single year, we examined IntCal09 dataset [*Reimer et al.* 2009], which is a quinquennial ^{14}C content dataset over a period of approximately ten thousand years. Figure 1 shows the IntCal09 data for the past 3000 years of this dataset. Only three periods in this time series show a rate of increase (change in the amount of ^{14}C content / time) larger than 3 ‰ over 10 years, at approximately BC 675 to 655, AD 760 to 785, and AD 1790 to 1820 as indicated by the arrows in figure 1. These three periods may therefore record high-energy events, but their time resolution is low and measurements with higher resolution are necessary to confirm that the increase really happened on a one-year time scale. The ^{14}C content for AD 1790 to AD 1820 [*Stuiver et al.* 1998b] and BC 675 to BC 655 [*Takahashi et al.* 2007] have already been measured with high time resolution and these studies did not find rapid increases. In this thesis, I report the measurement of ^{14}C content in Japanese cedar tree-rings for the period including AD 760 to AD 785 (the remaining period), with 1- to 2-year resolution.

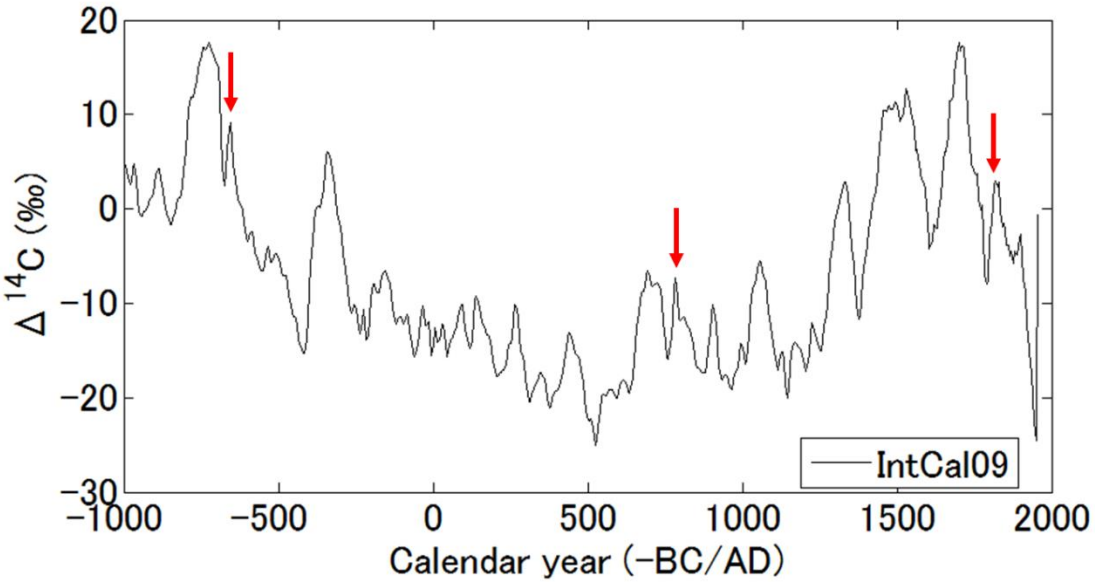

Figure 1: IntCal09 dataset of ^{14}C content covering the past 3000 years [*Reimer et al.* 2009], each points representing a five-year interval. The arrows indicate periods when the rate of increase was larger than 3 [‰/10yrs].

Chapter 2

Previous measurements

There are many periods when the ^{14}C content was measured with several time resolutions. Here, we show these previous measurements of ^{14}C content.

2-1 IntCal datasets

Libby et al. discovered ^{14}C in the atmosphere in AD 1947, and then, they established the method of the measurement of ^{14}C content in AD 1949. As ^{14}C is a radioisotope with a half-life of 5,730 years, we can see the ^{14}C record up to about 60,000 years ago. Carbon-14 causes the β^- decay as shown in the following formula:

$$^{14}\mathrm{C} \rightarrow {}^{14}\mathrm{N} + e^- + \nu_e$$

The ^{14}C measurement has been utilized for the age estimation of archaeological organic materials by using the decay of ^{14}C. For this purpose, the calibration curves for the radiocarbon dating had been made. They are some IntCal datasets (the IntCal98, the IntCal04, and the IntCal09), which are the most representative continuous ^{14}C data.

After an IntCal international working group started in the early 1980s, the decadal ^{14}C content data in tree-rings from the Northern Hemisphere for last 12,000 years have been collected. This results were published as the IntCal98 [*Stuiver et al.* 1998a]. After that, the ^{14}C data were extended to 24,000 years ago by using the foraminifer and coral data, and were published as the IntCal04 [*Reimer et al.* 2004]. The latest result is IntCal09 which was expended to 50,000 years ago [*Reimer et al.* 2009]. Although the time interval of the measured ^{14}C data is 10 years, the data resolution of the IntCal04 and the IntCal09 was improved to be 5 years during about last 12,000 years by using the random walk model [*Reimer et al.* 2004, 2009]. Table 1 shows the resolution and the periods for each IntCal series, and figure 2-1 shows the comparison of three IntCal datasets.

Table 1: The time interval of the IntCal (98, 04, and 09) datasets.

Resolution	INTCAL98 [BP]	INTCAL04 [BP]	INTCAL09 [BP]
5 years		-5 ~ 12,500	-5 ~ 11,200
10 years	-5 ~ 15,585	12,500 ~ 15,000	11,200 ~ 15,000
20 years		15,000 ~ 26,000	15,000 ~ 25,000
50 years			25,000 ~ 40,000
100 years			40,000 ~ 50,000
1,000 years	16,000 ~ 24,000		

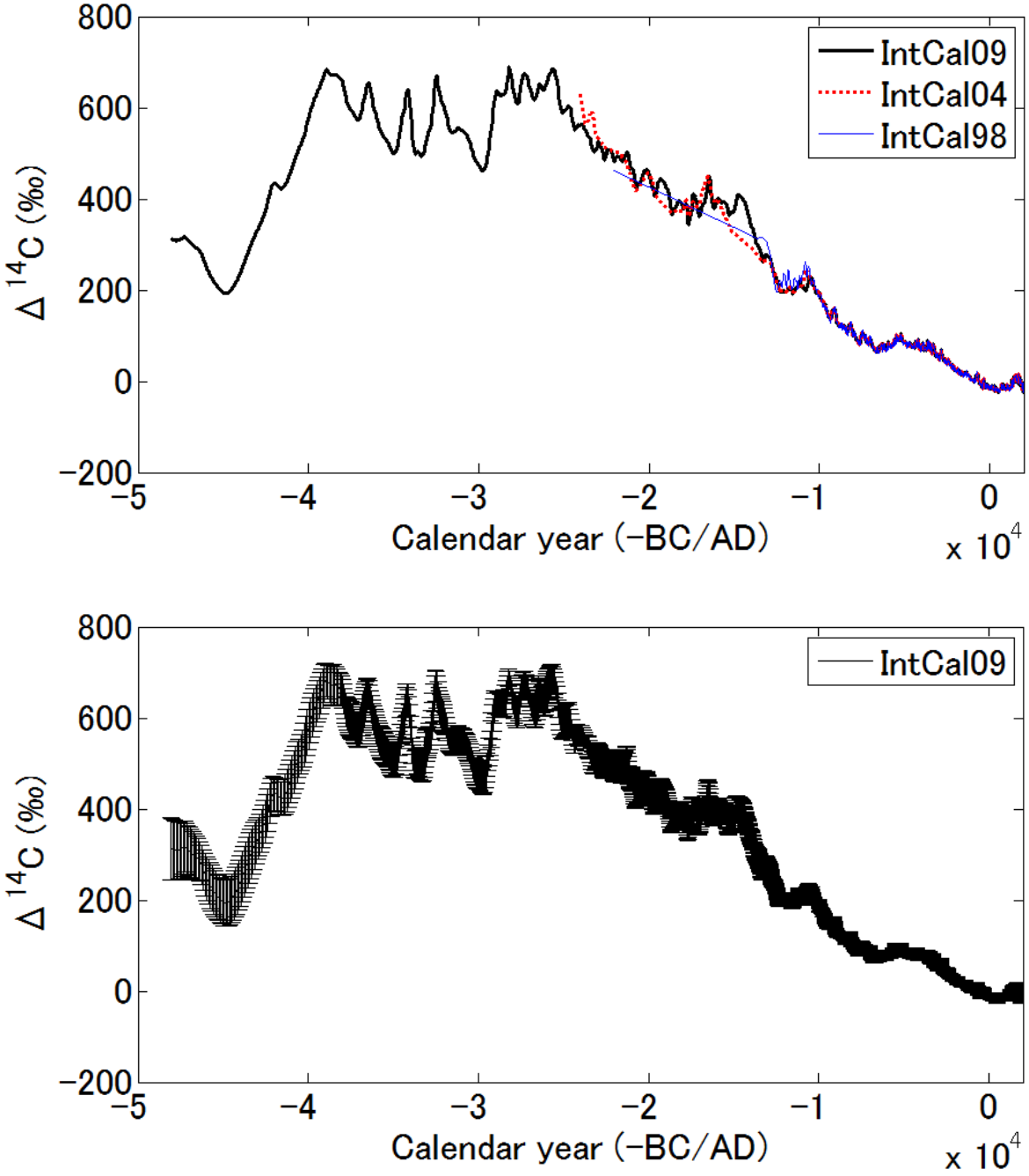

Figure 2-1: Comparison of the three IntCal (98, 04, and 09) datasets for the last 50,000 years [*Stuiver et al.* 1998a; *Reimer et al.* 2004, 2009]. (Upper) The black thick line shows the IntCal09, the red dotted line shows the IntCal04, and the blue thin line shows the IntCal98. (Bottom) The error range of the IntCal09 for the last 50,000 years.

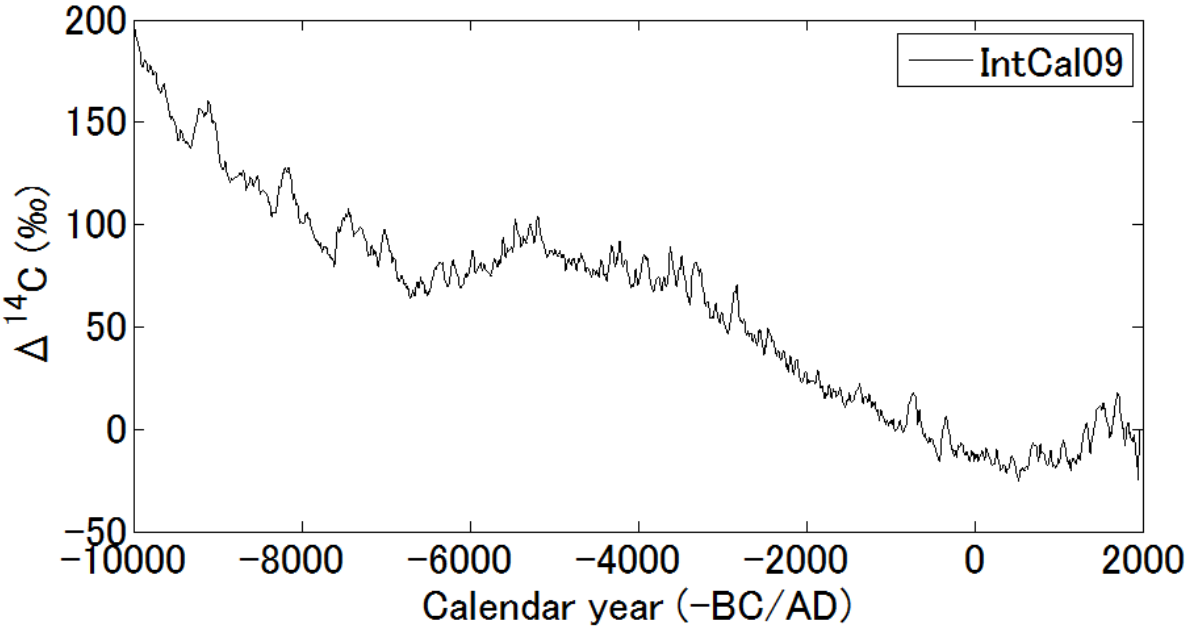

Figure 2-2: IntCal09 data for the last 12,000 years [*Reimer et al.* 2009]. The variation of the ^{14}C content is caused by the change of the cosmic ray intensity, which is mainly modulated by the solar magnetic activity and the geomagnetic field.

2-2 Yearly ^{14}C data

Although the IntCal data cover the measurement periods over more than 10,000 years, the annual or biannual ^{14}C content data was only measured in limited periods (sum total: ~2,000 years). These yearly measurements were conducted by some studies. We show these series in table 2.

Among these series, a representative yearly dataset measured first is the Stuiver series [*Stuiver et al.* 1998b], which uses North American trees. Figure 2-3 shows the ^{14}C content of the Stuiver series. A measurement range of this series is approximately 400 years from AD 1510 to 1954 in total. As the series following the Stuiver, there have been the Miyahara1&2, the Kuwana, the Kitazawa [*Miyahara et al.* 2004, 2006, 2010], the Menjo [*Menjo et al.* 2006], the Nagaya [*Nagaya et al.* 2012], and the Yoshimitu [*Nakamura et al.* 2013] series which are measured in Solar Terrestrial Environmental Laboratory (STEL), Nagoya University. These STEL series use Japanese trees. On the other hand, the Damon series is collected using North American trees to check the influence that recorded supernova explosions (SN1006 and SN1054) gives in ^{14}C content. Figure 2-4 ~ 2-7 shows the results of ^{14}C content measurement of the STEL series and the Damon series.

Table 2: Information of the annual or biannual ^{14}C series.

Series	Periods	Resolution	Sample	Reference
Stuiver	AD 1510-1954	1 year	North American trees	[73]
Kitazawa	AD 1346-1424	1 year	Yaku-B	[45]
Miyahara1	AD 1413-1554	1 year	Yaku-B	[43]
Miyahara2	AD 1617-1745	2 year	Muroji	[41]
Kuwana	AD 1557-1629	2 year	Yaku-B	[44]
	AD 880-964	1 year	Yaku-A	[44]
Damon	AD 998-1025,	1 year	North American tree	[13&14]
	AD 1065-1150			
Menjo	AD 992-1072	2 year	Yaku-A	[40]
		(AD 1000-1020: 1 yr)		
Yoshimitu	AD 72-202	2 year	Yaku-A	[56]
	AD 330-382			
Nagaya	BC 431- 281	2 year	Miyazaki_Kusu	[50]

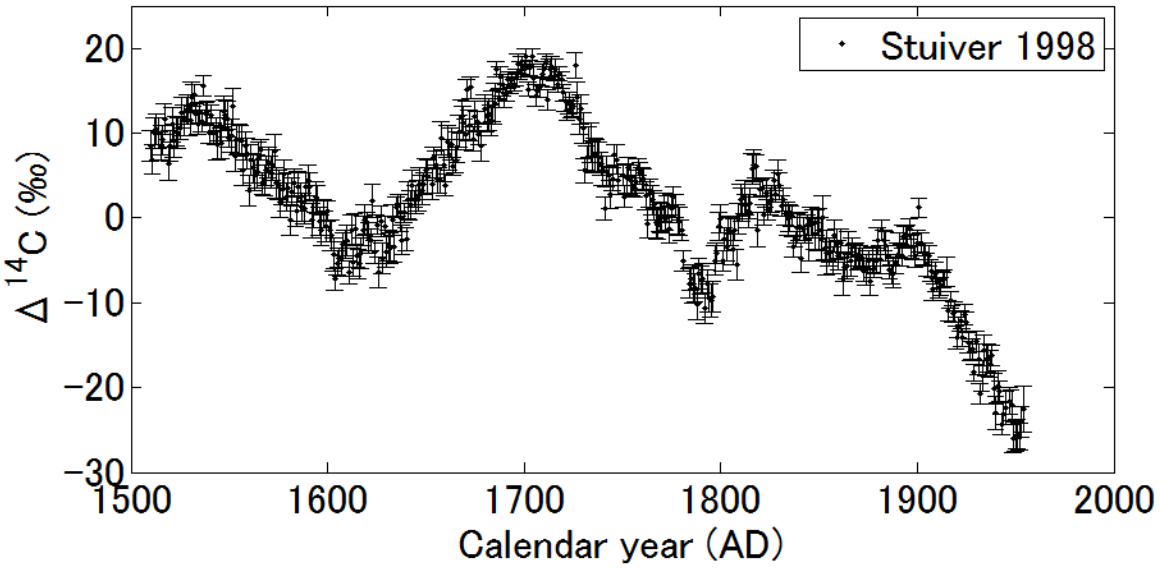

Figure 2-3: Yearly ^{14}C content data from AD 1510 to AD 1954 by *Stuiver et al.* [1998b]. Data for AD 1518, 1652, 1679, 1749, 1782, 1783, and 1946 do not exist.

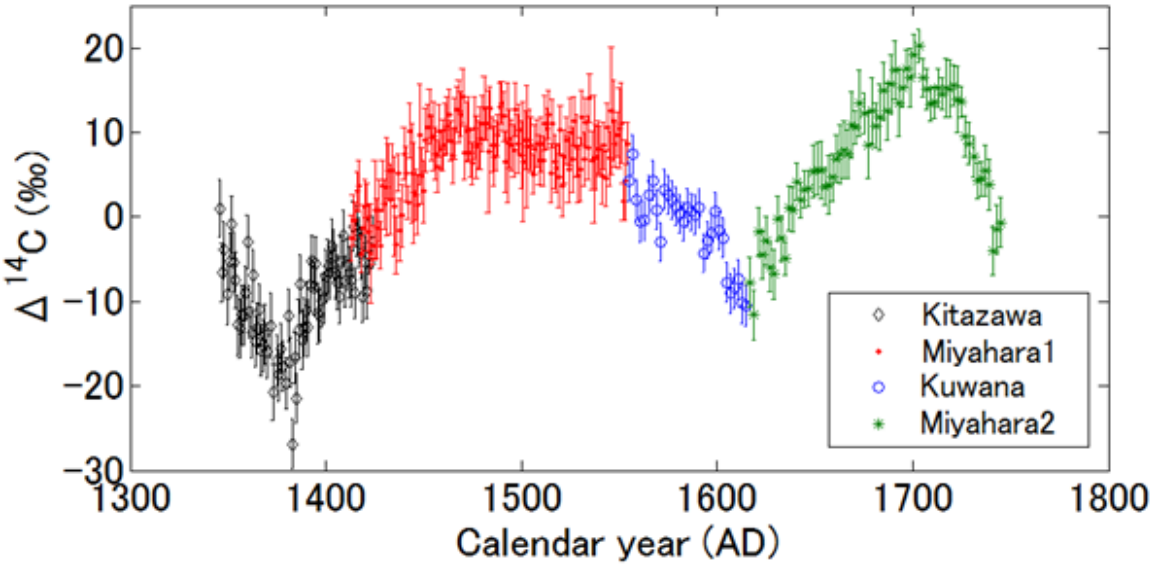

Figure 2-4: Annual and biannual ^{14}C content data from AD 1346 to AD 1745. These series are the STEL results using Japanese trees. The black open diamonds are the Kitazawa series, the red dots are the Miyahara1 series, the blue open circles are the Kuwana series, and the green stars are the Miyahara2 series (missing points of Kitazawa sereis: AD 1349,1371,1374, and 1379).

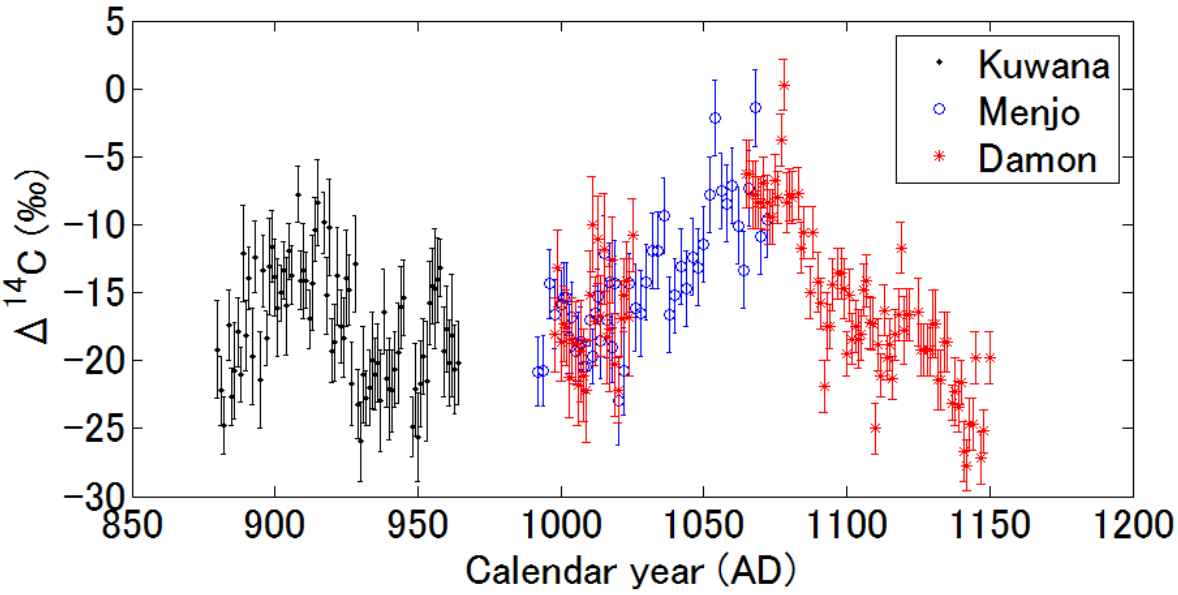

Figure 2-5: Yearly ^{14}C content data from the 9th to the 12th centuries. The black dots are the Kuwana series, the blue open circles are the Menjo series, and the red stars are the Damon series.

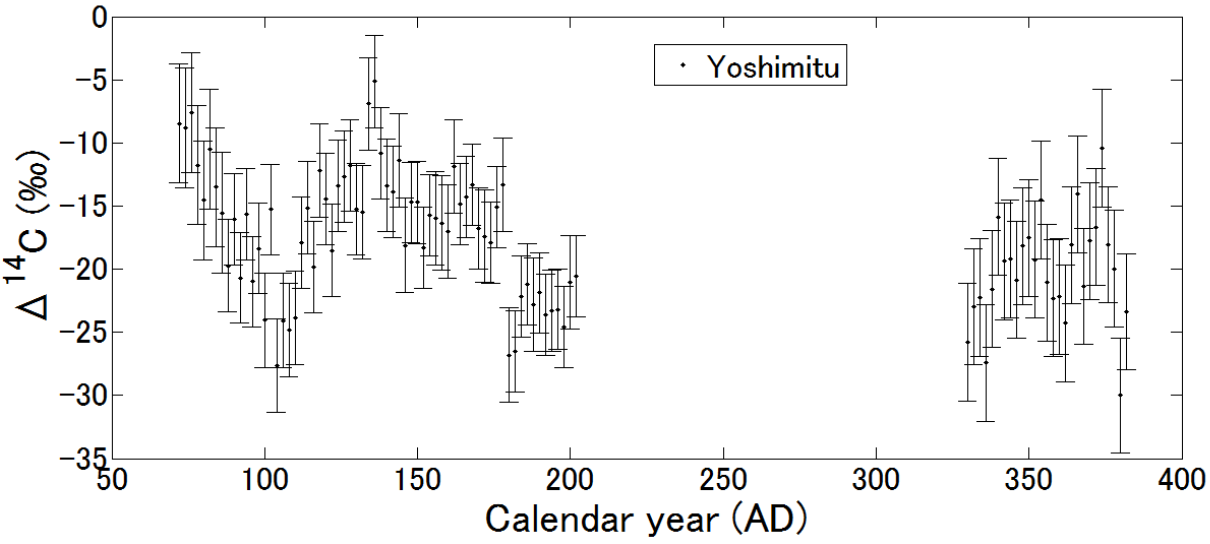

Figure 2-6: Biannual ^{14}C content data for the 1st to 4th centuries. The black dots are the Yoshimitu series [*Nakamura et al.* 2013].

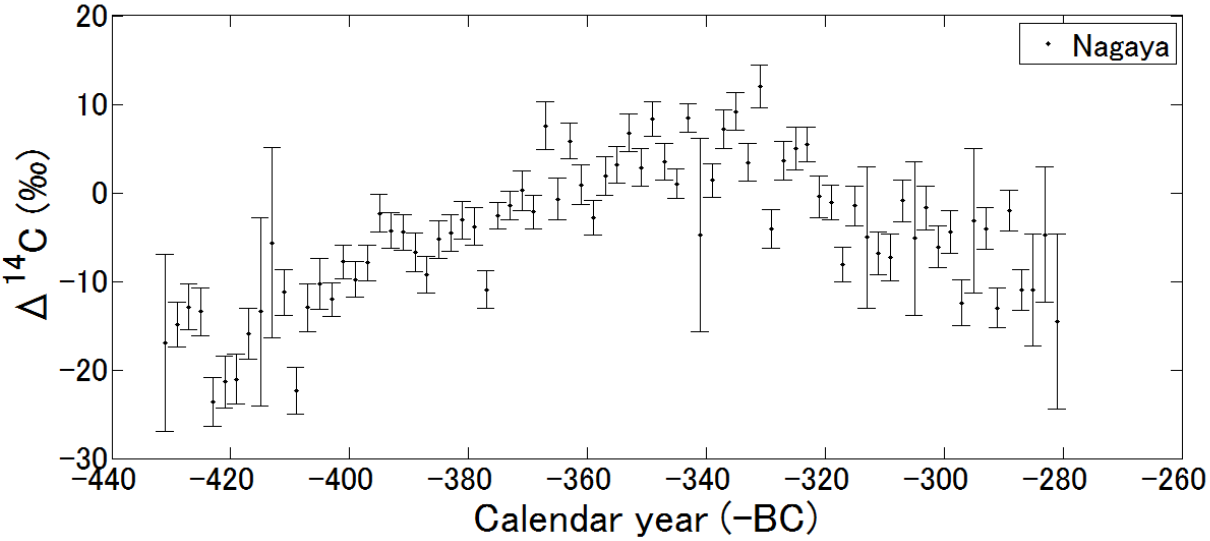

Figure 2-7: Biannual ^{14}C content data for the BC 4th century Minimum. The black dots show the Nagaya series [*Nagaya et al.* 2012].

Chapter 3

Relation between solar activity and ^{14}C

The variation of the ^{14}C content shown in the IntCal data (figure 1, 2-1 & 2-2) is caused by the change of the cosmic ray intensity, which is mainly modulated by the solar magnetic activity and the geomagnetic field. The variation with the timescale more than ~5,000 years is considered to be due to the geomagnetic activity. On the other hand, the variation with the timescale less than ~100 years is occurred by the solar activity.

The activity of our Sun has been studied by various methods. The oldest continuous record of the activity of the Sun is provided by sunspot measurements, which have been made since AD 1610 by telescopes being invented. The sunspot data of the past 400 years show that the sunspot number changes periodically, with a period of 11 years on average. Figure 3-1 shows a variation of sunspot number from AD 1610 to 1995 [*Hoyt and Schatten*, 1998]. This periodicity is called the Schwabe cycle [*Schwabe*, 1843]. The sunspot activity during a time interval in the late 17th century to early 18th century fell to near-zero levels. This period is known as the Maunder Minimum when the solar activity was considered to be very low level.

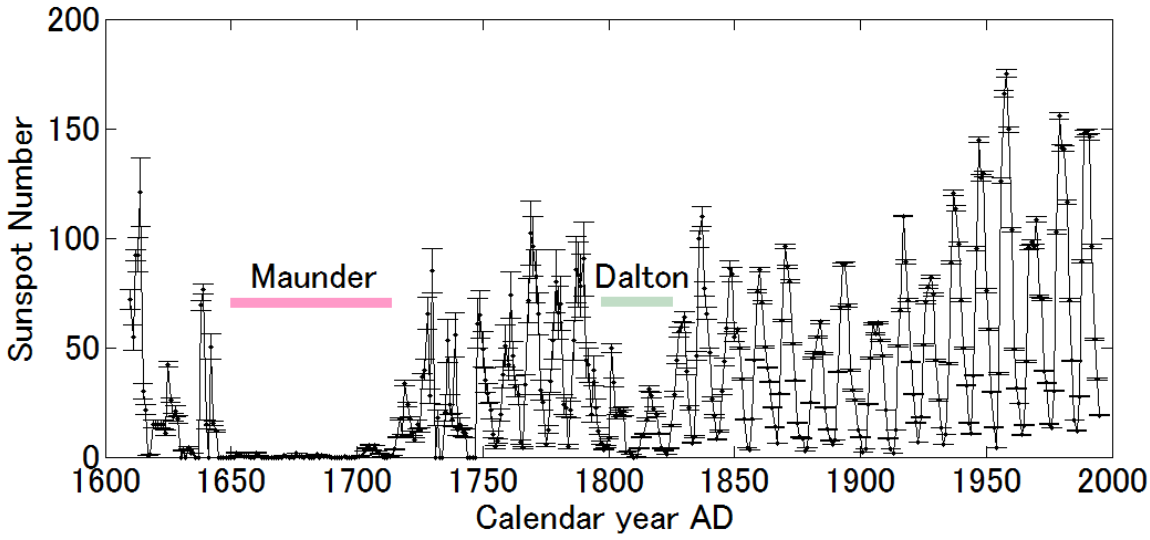

Figure 3-1. Variation in sunspot number from AD 1610 to 1995. The line with error bars shows the yearly-mean group sunspot number [*Hoyt and Schatten*, 1998]. The two lines represent the Maunder Minimum (AD 1645-1715) and the Dalton Minimum (AD 1800-1820), respectively.

Since the IntCal data also show an excursion of the ^{14}C content during the Maunder Minimum (figure 3-2), it is considered that the ^{14}C variation and the solar magnetic activity show an inverse correlation. There are other ^{14}C excursions similar to the Maunder Minimum in the past. These excursions are considered to indicate periods of solar inactivity, large excursions comparable to the Maunder Minimum are called "grand solar minima". There have been some attempts to investigate the occurrence of grand solar minima in the past. These studies have identified six to twenty grand solar minima in the last 5000-years [*Eddy*, 1977; *Stuiver and Quay*, 1980; *Voss et al.*, 1996; *Usoskin et al.*, 2007]. The differences in the number of identified grand solar minima are due to the analytical methods used and the criteria for identifying the minima. Figure 3-2 shows the main grand solar minima during the last 3000 years.

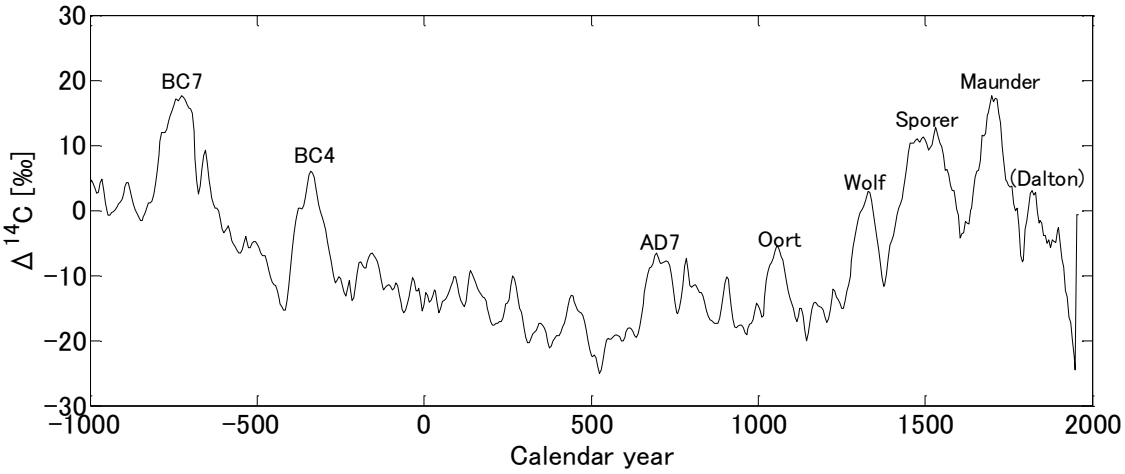

Figure 3-2: $\Delta^{14}C$ data for the past 3000 years (from IntCal09 [*Reimer et al.*, 2009]). The large peaks with names are grand solar minima, identified by *Eddy* [1977], *Stuiver and Quay* [1980], and *Usoskin et al.* [2007]. *Voss et al.* [1996] defined 13 additional grand solar minima, for example the Dalton Minimum around AD 1800.

As described in chapter 2-2, yearly ^{14}C content have been measured in several periods. These measurements were mainly conducted for grand solar minima (the Maunder Minimum, the Spörer Minimum, and the minimum in the 4th century BC [*Stuiver et al.*, 1998b; *Miyahara et al.*, 2004, 2006, 2010; *Nagaya et al.*, 2012]). From these yearly ^{14}C content measurements, it has been suggested that the length of the Schwabe cycle increased to ~14 years during the Maunder Minimum, to ~13 years during the beginning of the Spörer Minimum, and to ~16 years during the 4th century BC Minimum.

The variation in the ^{14}C content in tree-rings reflects the time-shifted and the attenuated solar activity due to the global carbon cycle (figure 3-3). The attenuation rate for the period of the typical Schwabe cycle (i.e. 11years) is calculated to be about 1/100 using the carbon cycle model [*Siegenthaler et al.*, 1980]. If the average ^{14}C production change is ±15% (this value is at the same level as the change of a ground neutron monitor), the amplitude of the Schwabe cycle corresponds to 1.5‰ in the ^{14}C content. When we search for a past high-energy phenomenon by ^{14}C method, it is necessary to consider this 1.5 ‰ of the Schwabe cycle as a background.

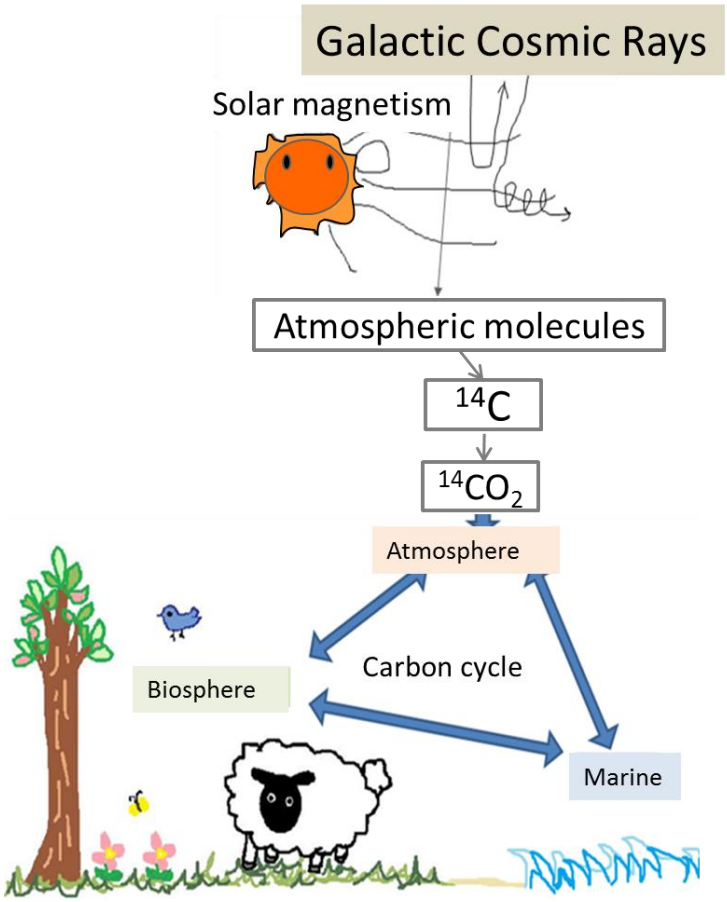

Figure 3-3: Relation between the cosmic ray intensity to the Earth, the solar activity and ^{14}C content. Cosmic rays to the Earth are modulated by solar magnetic activity. Incoming cosmic rays collide with atmospheric nuclides, and produce various particles and nuclides. Nitrogen captures a thermal neutron, which is produced by cosmic rays, and ^{14}C is produced (neutron capture reaction: $^{14}N + n \rightarrow {}^{14}C + p$). ^{14}C is oxidized to form $^{14}CO_2$ and is taken by trees during a global carbon cycle. As a consequence, ^{14}C content is retained in tree-rings and can show a record of the past solar activity and cosmic ray intensity.

Chapter 4

Historical records of cosmic ray events

As described in introduction section, if a cosmic ray event had occurred in the past, it is possible that the ^{14}C content data would record such an event. There are some historical records of the cosmic ray events. They are 7 supernovae records in our galaxy and some large solar flares, which are listed in the table 4-1 and table 4-2. The ^{14}C content during most of the recorded ages of these supernova explosions (SN1006, SN1054, SN1572, SN1604), the emergence years of the largest Carrington flare (AD 1859) and a ^{10}Be increase event around AD 1460 (the cause of this event is claimed as SN or large SPE, but has not been confirmed yet [*Delaygue et al.* 2011; *McCracken et al.* 2004; *Usoskin et al.* 2012]) have been measured with one year resolution by several previous studies [*Stuiver et al.* 1998b; *Miyahara et al.* 2004, 2006, 2010; *Menjo et al.* 2006; *Damon et al.* 1995, 2000]. We also measured the ^{14}C content around SN1006, SN1054 and SPE1859 using the Japanese cedar trees (I will mention these samples in chapter 5-2).

Figure 4-1 shows the ^{14}C content data for these historical events. As shown in figure 4-1, none of the ^{14}C contents show rapid increases within one year. There is also no ^{14}C increase within one-year during the period from AD 1374 to 1954 and some periods when there exist yearly ^{14}C data (see chapter 2-2). There are some yearly jumps of ^{14}C content in the Stuiver's series. I checked whether these ^{14}C jumps are explained as the measurement errors. Figure 4-2 represennts a histogtam of ^{14}C increment shown in sigma (siguma = [increment between two points] / [averaged measurement error]), but it shows the increments is distributed as statistical error. In order to detect a cosmic ray event by using the ^{14}C method, the total energy of cosmic rays incoming to the earth must be something bigger than that of these historical events.

Although I compared the ^{14}C data with the old history record so far, it is better to compare ^{14}C data with the more recent events like the SPE 2003 because we cannot know the accurate scale of these historical events. However, the ^{14}C record after the 1950s is ill-suited to investigate the natural terrestrial event. This is occurred by two serious problems which disturb a ^{14}C change of nature. One of them is a sharp and large ^{14}C content increase after the 1950s due to the atmospheric bomb test, which is called "bomb effect" (more detail in chapter 5-1-1). The other is an effect that ^{14}C content fades away by man-made CO_2 emission from the fossil fuel (= Suess effect). Therefore, we should compare with an event when ^{14}C content is not polluted artificially.

Table 4-1: Historical records of the supernovae which located in our galaxy.

Supernova	Year [AD (date)]	Peak mag. (v)	Type	SN remnant	Distance [ly]	Constellation
SN 185	185 (Dec. 7)	-8	Ia?	RCW 86	9,100	Circinus & Centaurus
SN 393	393	-1	II/Ib	RX J1713.7-3946 ?	3,000	Scorpius
SN 1006	1006 (May 1)	-9	Ia	SN 1006	7,000	Lupus
SN 1054	1054	-6	II	Crab Nebula	6,500	Taurus
SN 1181	1181	0	II?	3C58?	>24,000	Cassiopeia
SN 1572	1572 (Nov.)	-4	Ia	Tycho's Nova	8,000-9,800	Cassiopeia
SN 1604	1604 (Oct. 9)	-2.5	Ia	Kepler's Star	20,000	Ophiuchus

Table 4-2: Historical records of large solar flares.

Solar flare	Year [AD]	Comments
SPE 1460	1460	Detected by ^{10}Be data from the ice core. The cause has not been specified yet.
Carrington flare	1859	The largest solar flare on record. Aurorae were seen around the world (Caribbean, Hawaii, and so on). Telegraph systems failed (Europe & North America).
SPE 1989	1989	Quebec (Canada) blackout, radio interference

SPE 2003	2003	"Halloween storm" the most intense flare ever measured on the GOES sattelite

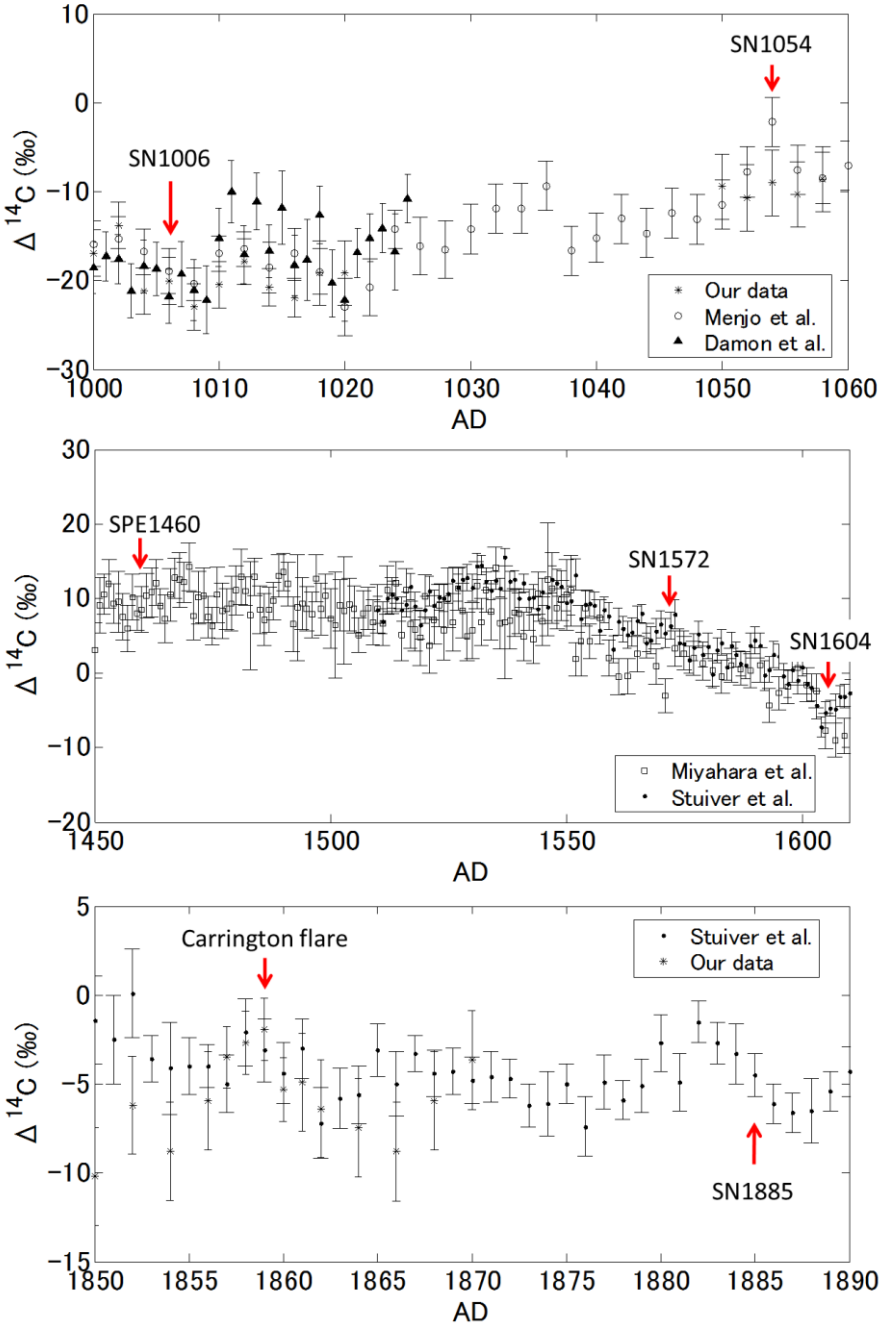

Figure 4-1: Annual or biennual ^{14}C records around recorded years of supernovae and large SPEs. (Upper) $\Delta^{14}C$ records from AD 1000 to 1060. The stars show our data using Yaku-A, the open circles are data of *Menjo et al.* [2005], and the filled triangles are data of *Damon et al.* [1995]. The two arrows indicate SN1006 and SN1054. (Middle) A time profile of $\Delta^{14}C$ from AD 1450 to 1610. The open squares are data of *Miyahara et al.* [2006, 2007], and the dots are data of *Stuiver et al.* [1998b]. The three arrows indicate SPE1460, SN1572, and SN1604. (Bottom) A time profile of $\Delta^{14}C$ from AD 1850 to 1890. The dots show the data of *Stuiver et al.* [1998b] and

the stars show our data using Yaku-B. The two arrows indicate the Carrington flare (SPE1859) and SN1885 (in the Andromeda Galaxy).

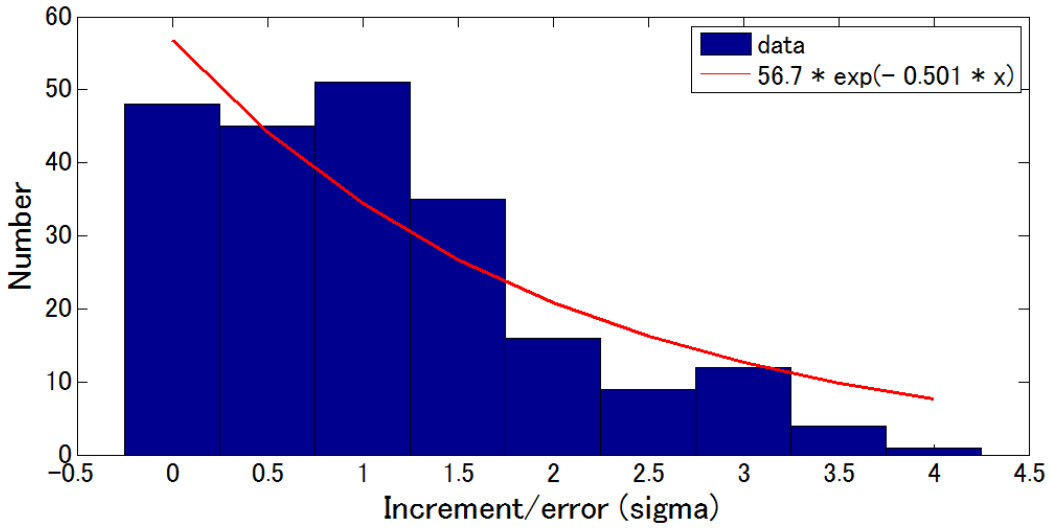

Figure 4-2: A histgram of yearly increase of the Stuiver series [*Stuiver et al.* 1998b]. The horizontal line shows increment between two points over averaged measurement error (sigma). The red line represents the best value of an exponential function fitting.

Chapter 5

Methods

5-1 Age determination

To investigate a past ^{14}C content records, we have to determine dates of sample tree-rings. Main methods of dating of tree-rings utilized are following three:

1) To make the outermost layer of tree-ring the cutting down year

2) To using large ^{14}C peak in AD 1964 (=bomb effect)

3) Dendrochronology

If we know the cutting year of sample tree, we use the method No.1 to determine date of tree rings. Trees in temperate and boreal regions generally form one ring a year (one ring is clearly defined by light-colored earlywood and dark-colored latewood). However, trees sometimes have two or three rings (= false ring) or have no ring in a year (figure 5-1). This is due to growing environment of trees. In these cases, it is difficult to determine dates of inner rings, whereas we can determine the date of the outermost rings. The bomb effect method is same in terms of dates of inner rings than AD 1964 are undetermined. Then using a method of dendrochronology is necessary, and we usually determine the date by combining with these three methods. Detailed explanations for the bomb effect and dendrochronology are next.

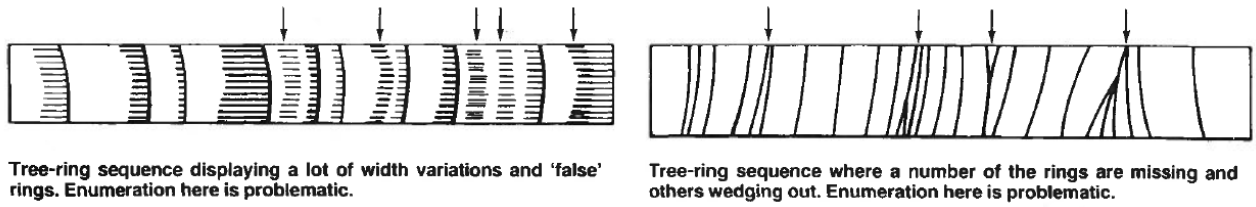

Figure 5-1: Images of false rings (left) and missing rings (right). This figure is cited from *Schweingruber* [1987].

5-1-1 Bomb effect method

The most pronounced increase of atmospheric ^{14}C content in the history was seen in the 1950s to the 1960s. This increase was caused by many tests of nuclear explosion in the atmosphere and is called the "bomb effect". The ^{14}C content increment reached about 100% in AD 1964 compared to the ^{14}C level before nuclear explosions. This increment is much higher than normal variations of ^{14}C content occurred by a natural origin. Since ^{14}C contents in trees around the world record the variation of bomb effect (figure 5-2), we can determine the date of unknown tree sample by comparing ^{14}C content of such tree and previous results.

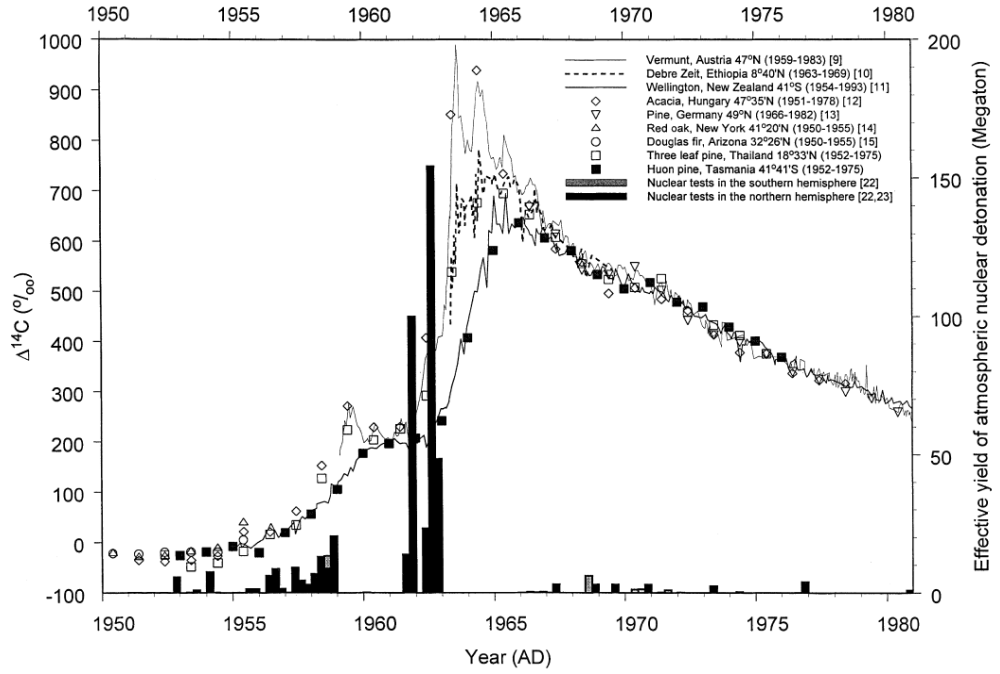

Figure 5-2: Effective yield of atmospheric nuclear detonation and difference by the latitude in ^{14}C content from AD 1950 to 1980. This graph is cited from *Hua et al.* [2000]. Lines and marks represent measured ^{14}C content in atmosphere and tree-ring sample, respectively. Bars show a scale of atmospheric nuclear test in the unit of megaton.

5-1-2 Dendrochronology

A fundamnatal technique of the dendrochronology is called “cross-dating”, which is a pattern matching of the time sequence of ring widths to that of the standard. The standard is created by the next method: (1) First, tree-ring patterns are extracted from living trees or trees that the falling year is known. (2) The living tree chronology is extended by obtaining tree-ring patterns from dead standing trees using the bridging technique shown in figure 5-3 .

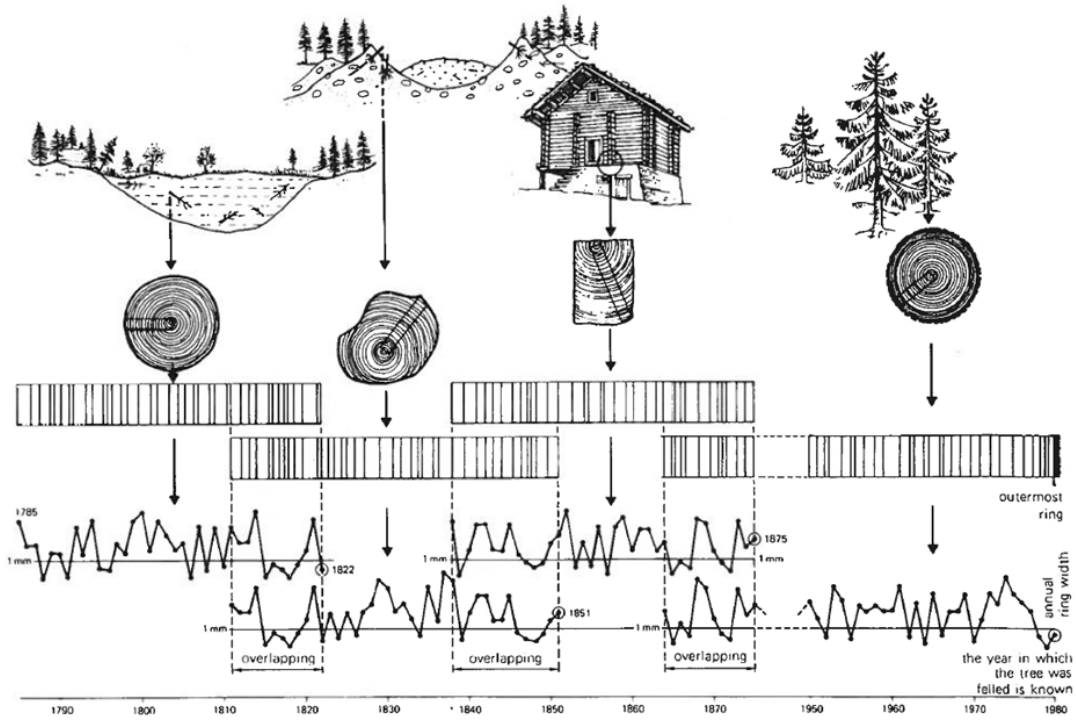

Figure 5-3: A schematic representation of the dendrochronology using the bridging technique. This figure is cited from *Schweingruber* [1987].

5-2 Samples

We used three Japanese cedar trees (*Cryptomeria japonica*) for this study. These trees came from Yaku-island located in the southern Japan, which was designated as a world heritage-listed area in 1993 and a lot of long-lived trees inhabit. We call these trees as Yaku-A (figure 5-4), Yaku-B (figure 5-5), and Yaku-14ANb (figure 5-6) as a matter of convenience. In addition to these samples, we used

Hinoki cypress sample (*Japanese cypress*) from Iida city, Nagano prefecture, Japan. Further information of these trees is listed in table 5-1.

Yaku-A has been cut down by the people of the district forestry office at Yaku Island in AD 1956. The stump of Yaku-A has been laying at logging area for about 40 years, after that, we got this tree in AD 1995. The date of Yaku-A has been determined by the method of dendrochronology. A time sequence of tree-ring width of Yaku-A is shown in figure 5-7. As a result of cross-dating between ring widths sequence of surface 500 years of Yaku-A and that of a standard by K. Kimura (the master series of the ring width has not been released), the date of outermost layer of Yaku-A is AD 1551 (t-value is 6.94). It is thought to be that about 400-years outer circumferential tree-rings have been lost during the period when Yaku-A had been laying at logging area.

A date of Yaku-B is determined by the methods of the bomb effect and the dendrochronology. A result of ^{14}C content measurement in Yaku-B around bomb peak and a time sequence of tree-ring width of Yaku-B are shown in figure 5-8 and figure 5-9, respectively. We used this sample to investigate the ^{14}C variation around the largest Carrington flare which occurred in AD 1859.

Yaku-14ANb was supplied by K. Kimura in AD 2011, who got it at the district forestry office at Yaku Island. Figure 5-6 shows a photo of Yaku-14ANb sample core.

Table 5-1: Information of the Japanese tree samples. The sample of Yaku-14Nb and Hinoki were supplied by K. Kimura (Fukushima University) and T. Mitsutani (National Research Institute for Cultural Properties), respectively.

	Yaku-A	Yaku-B	Yaku-14Nb	Hinoki
Measured period	AD 550-1100	AD 1850-1870	AD 770-779	AD 988-997
Growing age	AD 97-1956	AD 1280-1991		
Usable tree-rings	AD 97-1551	AD 1280-1991	AD 643-854	AD 930-1030
Method of age determination	Dendro-chronology	Bomb effect peak & dendro-chronology	Dendro-chronology	Dendro-chronology
Location	30.2° N, 130.3° E	30.2° N, 130.3° E		35.2°N, 137.6°E
Altitude	885 m			~400 m

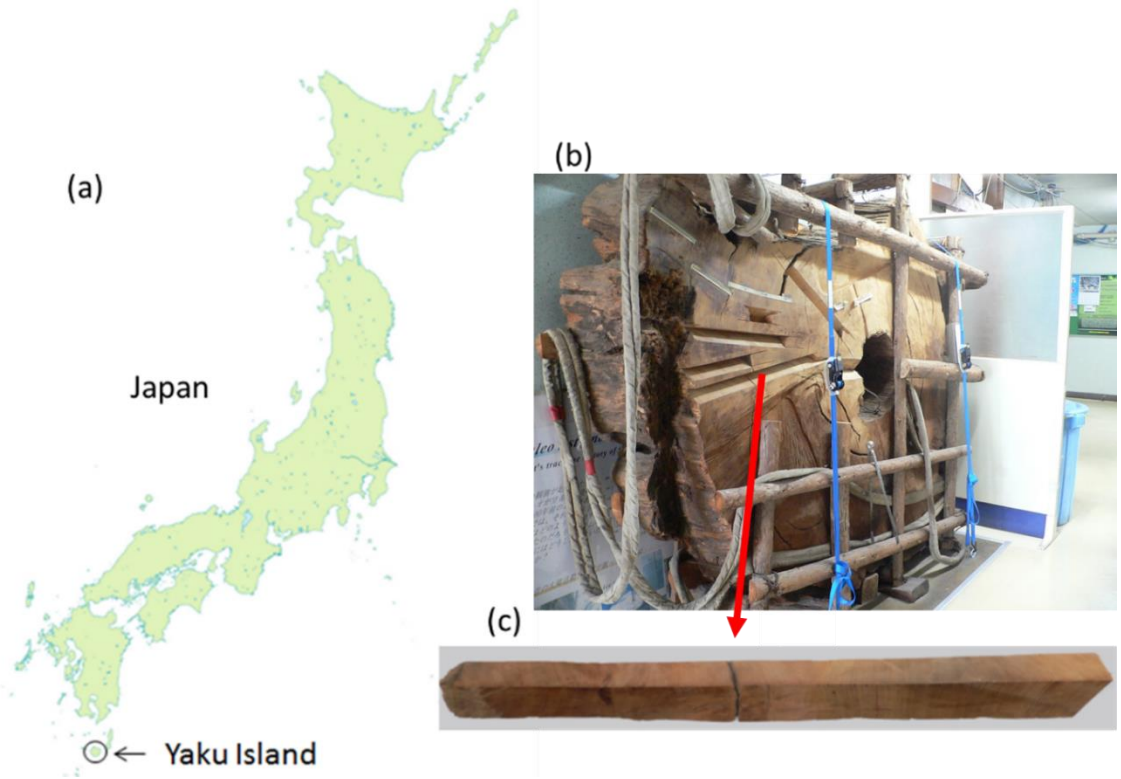

Figure 5-4: (a) Location of Yaku Island. (b) A photo of the stamp of Yaku-A. The diameter is about 1.9m, and the thickness is 30cm. This sample is held in STEL, Nagoya University. (c) Cut core of Yaku-A for this study, from AD 367 to 1172 (triangular pole, about 4 cm x 7 cm x 5 cm x 52 cm).

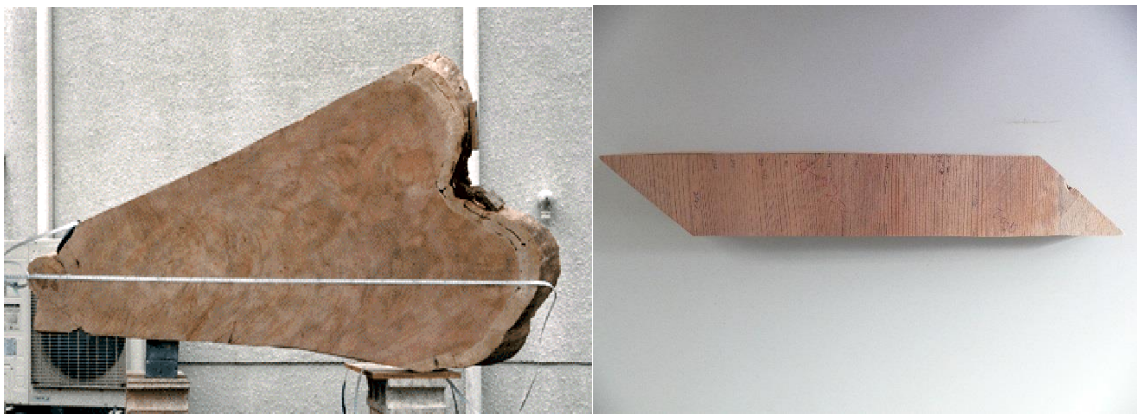

Figure 5-5: (Left) A photo of the stamp of Yaku-B. (Right) The cut core of Yaku-B. Core no. is a'-02-2.

Figure 5-6: A photo of Yaku-14ANb sample core.

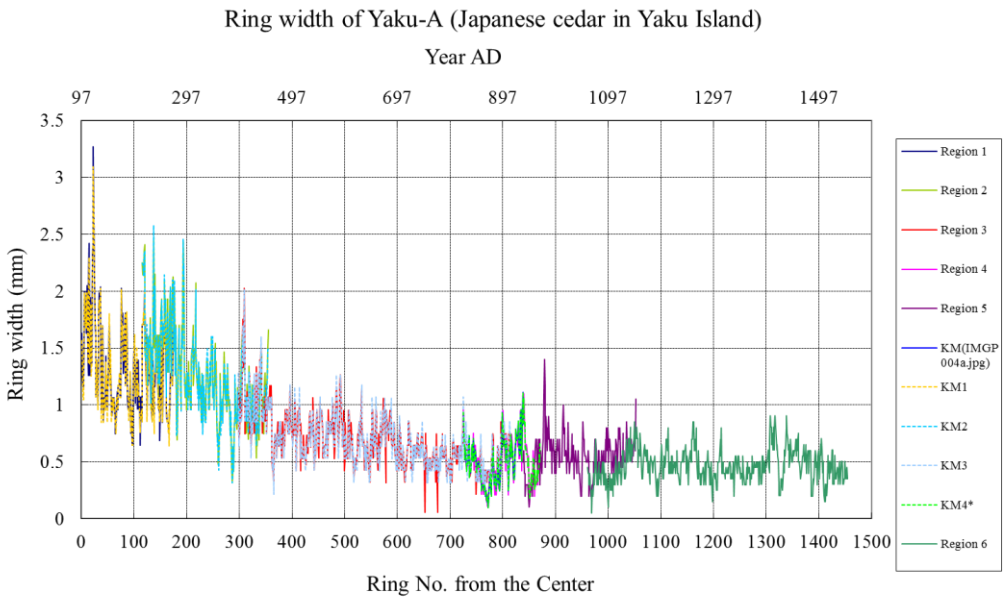

Figure 5-7: A time sequence of tree-ring width of Yaku-A. Different colors of each series show the measured region of Yaku-A. There is a missing layer around AD 956.

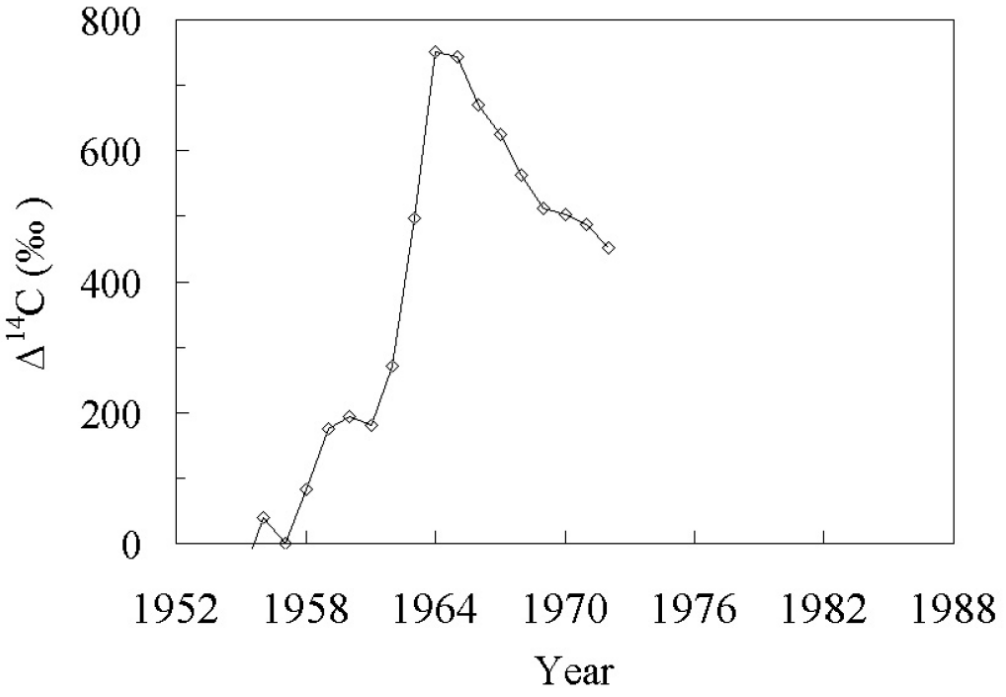

Figure 5-8: Measured carbon-14 content in the tree-rings of Yaku-B around the Bomb peak. This graph is cited from *Miyahara* [2005].

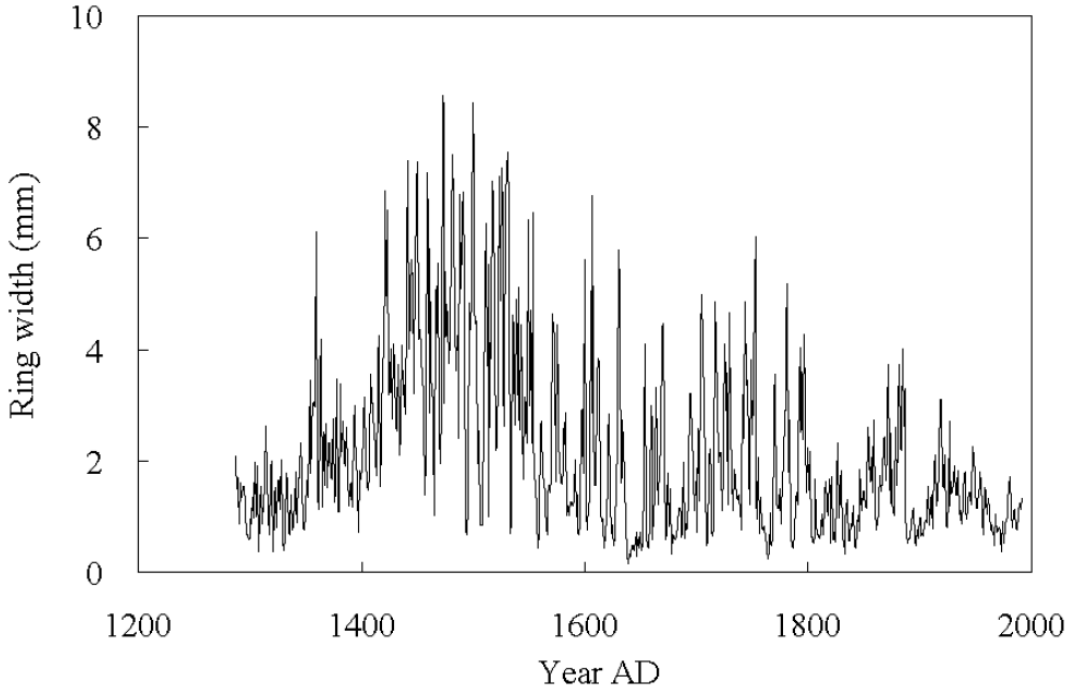

Figure 5-9: A time sequence of tree-ring width of Yaku-B. This graph is cited from *Miyahara* [2005].

5-3 Formation of tree-rings

Tree-rings are formed by repeated cell divisions in the cambium which lies between the bark and the old wood of trees. The cambium produces the phloem and the xylem in parallel. The phloem is a part of inner bark, and become outer bark as time advances. A role of the phloem is mainly the transport of photosynthetic products. The xylem locates inner of the cambium, and is most of the wood. In the softwood, more than 95% of the xylem is the tracheid which is elongated cell and its roles are the water transport and the tree conservation. A cell-wall during a radial growing period of the tracheid (cells divide repeatedly) is called primary wall. When the cell division is finished, thickening of the cell-wall starts (= secondary wall thickening). Finally, the solid cell-wall is left after finishing the secondary wall thickening and disappearing the protoplasm in cells.

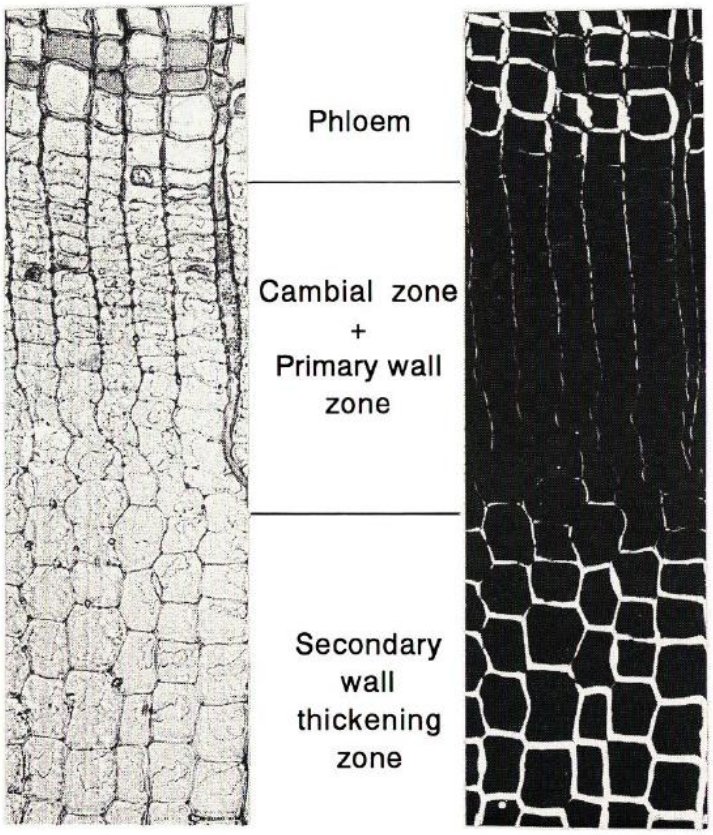

Figure 5-10: Micrographs of *Picea glehnii* (left: light micrographs and right: polarized micrograph).This picture is cited from *Yasue et al.* [1994].

The activity of the cambium changes in a year. During the growing season of spring, the earlywood, which has large diameter cells and has thin cell walls, is formed. On the other hands, the latewood, which has small diameter cells and has thick cell walls, is formed during from summer to autumn. By repeated such cambium activities, tree-rings are formed. Although a rough formation seasons of the earlywood and the latewood is known as above, an accurate ring formation periods are affected by a number of parameters such as temperature, sunshine duration, growing conditions, and so on. We have to know the growing season of trees in Yaku-Island, especially where nearby our sample trees lived.

In order to know a time variation of tree-ring formation process, a dendrometer method and a method of cells observation are usually used. Although the cells observation method can determine the growing season more accurately, only the dendrometer method, which measures the diameter of trees, is applied to Yaku-cedar (Aze, private communication). The time variation data of the diameter of a typical tree for about 2 years are shown in figure 5-11. This tree is living in Ishizuka where Yaku-A has lived. An increasing of the diameter is observed from early-May to mid-October. Then, it is considered that the cell division occurres in this period. However, we must consider the secondary wall thickening which continues after the stop of cell division, because a carbon is fixed during this period. By using a method of the observation of cells of other region trees, it is known that timing of the offset of the secondary wall thickening is about one month later than the cell division stopped. Figure 5-12 shows time variations of number of cells in the various tissue zones of *Picea glehnii* growing in the Teshio Experimental Forest of Hokkaido [*Yasue et al.* 1994]. If this time lag is applied to Yaku-cedar, the period of fixing the carbon is from early-May to mid-November.

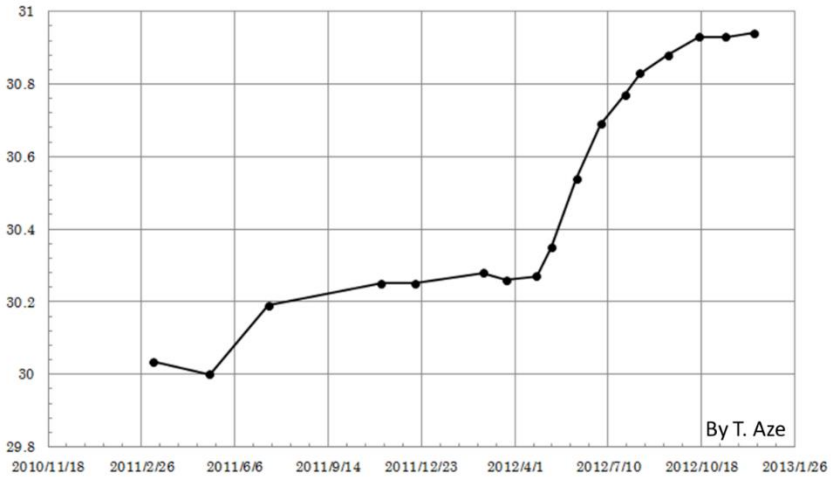

Figure 5-11: Diameter of a typical Yaku-cedar (Ishizuka). The vertical line shows the diameter of the tree in units of centimeter, and the horizontal line shows the date from March 2011 to December 2012. This result is provided by T. Aze.

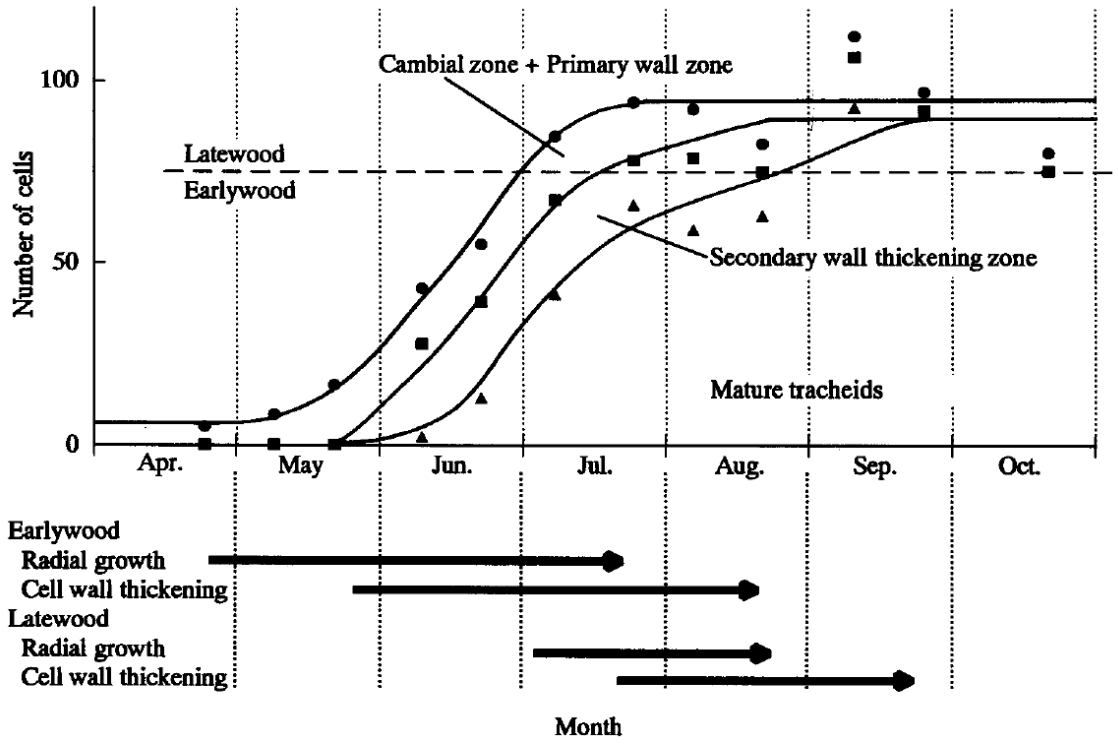

Figure 5-12: Smoothing growth curves of *Picea glehnii*. (triangles: Mature tracheids, squares: mature tracheids and secondary wall thickening, and circles: newly formed tracheids). This graph is cited from *Yasue et al.* [1994].

5-4 Chemical components

Components of wood are divided into major components and minor components. The major components include celluloses, hemicelluloses, and lignins. They are called the big three basic components of woods. In common species of trees, more than 90% of wood structural components account major components. Celluloses and hemicelluloses are composition of the cell wall, and lignins fill the spaces in the cell wall between celluloses and hemicelluloses (figure 5-13).

On the other hands, minor components are composed by aliphatic compound, aromatic compound, nitrogen compound, pectic substance, mineral, and so on. In these components, an order of hardness to move between rings is the cellulose, the hemicellulose, the lignin, and the minor components. Then, we should extract the cellulose which hardly moves between rings, to investigate a

precise ^{14}C level with one-year order. Figure 5-14 shows a diagram of these constituents of wood. Further chemical feature of major components will be described below.

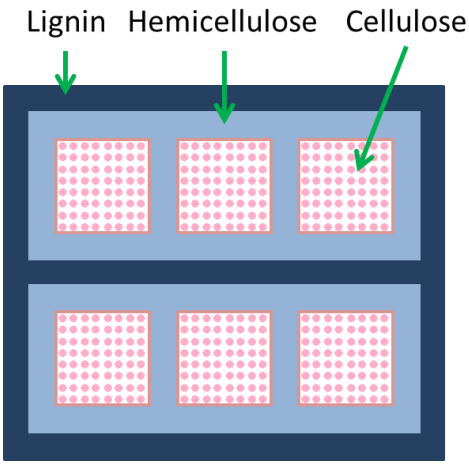

Figure 5-13: Image of cell wall components of wood (cellulose, hemicellulose, and lignin).

5-4-1 Cellulose

Cellulose is a major chemical component of fiber wall. In case of *Cryptomeria japonica*, cellulose is composed about 40% of whole wood. And cellulose is homopolymers composed by linear chains of D-glucose linked by β-1,4-glycosidic bonds. Cellulose forms tight bundles which are very resistant to chemical attack (such as alkali dissolution and acid hydrolysis).

5-4-2 Hemicellulose

Hemicellulose is also polysaccharides, but different from celluloses because hemicellulose contains not only glucose but also other sugars. There are several types of hemicellulose due to types or combinations of sugars. Hemicellulose is not very resistant to chemical attack. Most type of hemicellulose are alkali solubility.

3-4-3 Lignin

Lignin is a phenolic substance of complex polymer, and its main function is the support through strengthening of wood. Lignin is removed from wood usually by treating with agents such as sodium chlorite under acid (=Wise method).

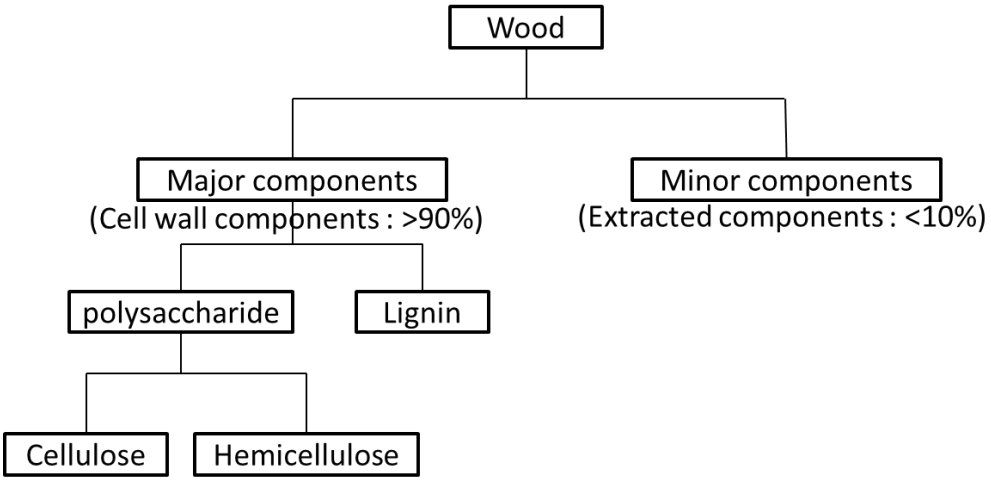

Figure 5-14: Constituents of wood.

5-5 Sample pretreatments

In order to measure the ^{14}C content in tree-rings, we must produce graphite from wood samples. Figure 5-15 shows a flow chart of the sample pretreatments and the AMS measurement. Each process will be explained in the followings.

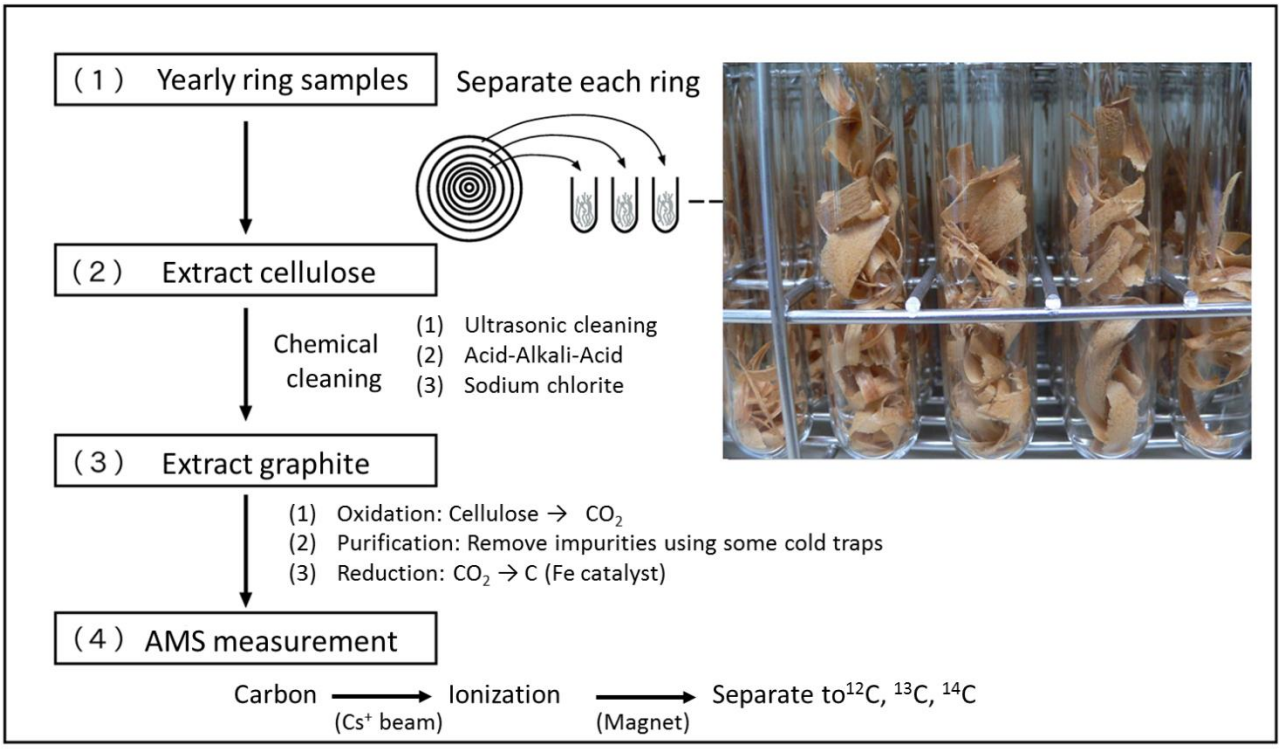

Figure 5-15: Flow chart of the sample pretreatment.

5-5-1 Cutting core and separating rings

Firstly, we cut the sample cores (triangular pole) from the disk of trees using a circular saw. The annual rings were carefully separated from the cut core. Figure 5-16 shows separated annual samples in test tubes. In this process, we used a cutter knife to slice woods uniformly (for sample), and used a metal spatula to remove woods in a ring completely (throwing away).

Figure 5-16: Separated wood samples. Each samples in test tubes are annual ring sample.

5-5-2 Chemical treatment

Since wood is composed by various constituents (figure 5-14), each sliced wood sample was employed to extract cellulose, which doesn't move between annual rings. For this purpose, we applied a chemical treatment which is composed of ultrasonic cleaning, Acid-Alkali-Acid treatment, sodium chlorite treatment, and neutralization.

・Ultrasonic cleaning

The main purpose of this process is to remove fine dusts which is attached to surface of the wood. Firstly, approximately 100mg of each sliced sample is put into a vial, and is washed by ethyl alcohol or/and distilled water in the ultrasonic bath. The temperature in the bath was set to be 55℃. All procedures of the ultrasonic cleaning is followings:

(1) 1 hour ethyl alcohol[1] -> 1 hour distilled water[2] -> 1 hour distilled water or

(2) 1 hour distilled water -> 1 hour distilled water -> 1 hour distilled water

After 1 hour ultrasoic cleaning, old solutions was changed to new ones. When we started our study, we have washed our sample by using a method of (2), which is used only distilled water. However, a Japanese cedar tree containes a lot of resin components which easily move between rings. Then, we applied a method of (1), which includes ethyl alcohol process, to remove resin components.

・Acid-Alkali-Acid (AAA), $NaCl_2O$, Neutralization

Firstly, samples are soaked in HCl[3] (1.2N), NaOH[4] (1.2N) and HCl (1.2N) solutions. This is called an Acid-Alkali-Acid (AAA) treatment. The temperature of the solutions was set to be 60℃, and each process was done for two-hours. The first acid treatment was repeated 3 times, the second alkali treatment was repeated 4 times, and the last acid treatment was left it in the room temperature for all

[1] Ethanol (99.5), Wako

[2] Distilled water, Wako

[3] Hydrochloric acid, assay: 35.0-37.0%, Wako

[4] Sodium Hydroxide, assay min.: 97.0%, Wako

night. Some minor components can be removed by the acid treatment, and hemicellulose is removed by the alkali treatment.

Secondally, samples were bleached with hot $NaCl_2O$ [5] / HCl (1.2N) solution. The mass of $NaCl_2O$ which is put into the HCl solution is 1.6 times larger than an originally wood mass (100mg). The solution temperature was set to be 90℃. Although $NaCl_2O$ shows yellow in acid solutions, changes to be colorless when it reacts with the wood sample completely. Therefore, when the color of solutions became colorless, we stopped the $NaCl_2O$ treatment. The purpose of the $NaCl_2O$ treatment is to remove the lignin.

After that, we also applied Alkali-Acid treatment whose purpose is to be remove the hemicelullose perfectly.

Finally, the samples were washed in hot distilled water (100℃) repeatedly. We finished this neutralization process when the solution became neutral.

Undergoing these processes, we got celluloses which look like white fibers. Usually, approximately 20 mg of cellulose was obtained for each sample. These processes are treated on the hotplate which temperature can be controlled. A flow chart and pictures of above processes are shown in figure 5-17 and figure 5-18, respectively.

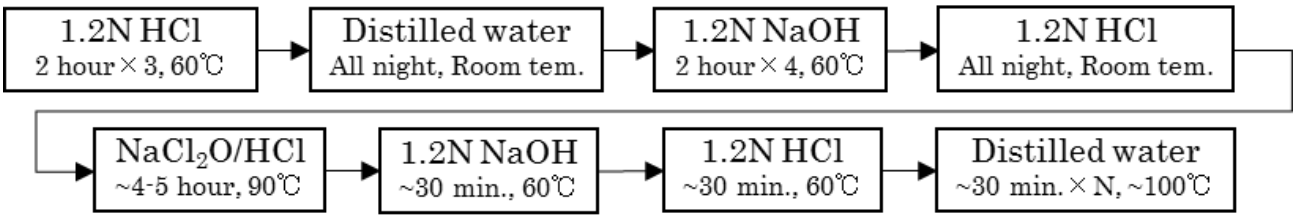

Figure 5-17: Flow chart of chemical cleanings.

Figure 5-18: Photos of chemical cleanings.

[5] $NaCl_2O$, FW: 90.44, Kanto chemical co. inc.

5-5-3 Gasification

In this process, the pretreated material was combusted with CuO in vacuum to CO_2. Firstly, we put a cellulose sample (5.5-5.9 mg), CuO [6] (1.00-1.10 g), and sulfix[7] (Co_3O_4:Ag_2O=1:1, 15-30mg) into a silica glass cup (6mm ϕ, ~3cm). The copper oxide is an oxidizing agent, and the sulfix is sulfur oxides and halogens remover. Then, we have set this cup in the silica glass tube (9mm ϕ, 30cm), and have vacuated the tube by using the vacuum line "D", shown in figure 5-19. After the pressure in the vacuum line becomes below 5×10^{-3} Pa, we cut and sealed the silica tube by using a gas burner, to confine samples in the very low pressure. The sealed tubes were burned in 850℃ for three hours using an electrical furnace[8], and CO_2 was obtained. The reaction formula is following:

$$(C_6H_{10}O_5)_n + 12nCuO \rightarrow 6nCO_2 + 5nH_2O + 12nCu \qquad (1)$$

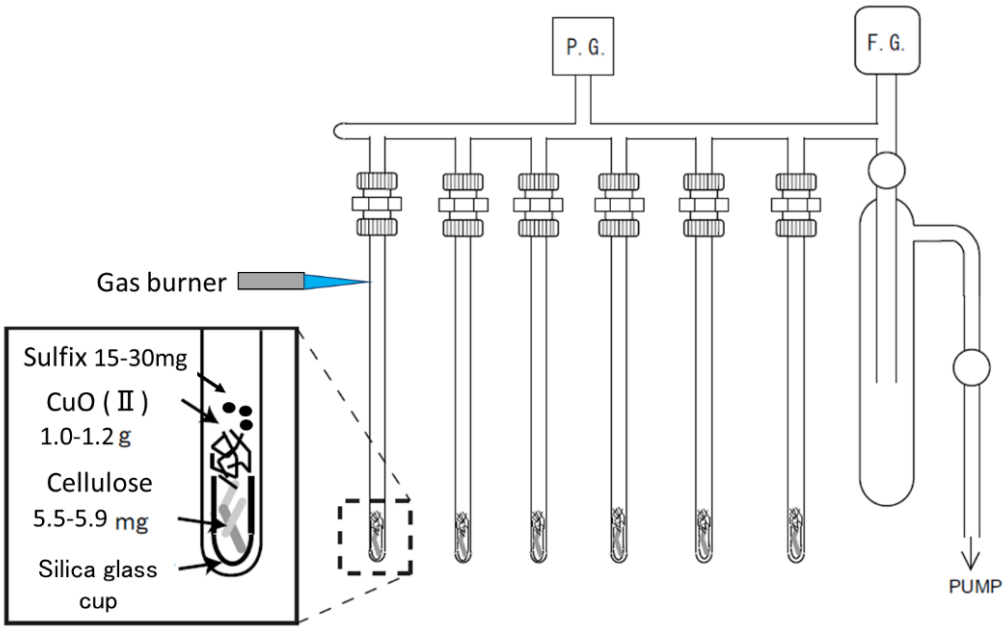

Figure 5-19: The vaccume line D for sealing.

[6] Copper (Ⅱ) oxide, wire, ϕ 0.6mm×2-5mm, Wako

[7] Sulfix, 850-2360 μm, 8-20 mesh, Wako

[8] KBF894, Koyo Thermo Systems Co.

5-5-4 Purification, Graphitization

By looking at the equation (1), we can see not only CO_2 but also H_2O in the sealed tube. Therefore, we should separate CO_2 from H_2O because H_2O prevent a graphitization process. To obtain the purified CO_2, we used the vacuum lines (A & C) and the cold traps. Figure 5-20 shows the vacuum line. First step of the purification is that we set the sealed tube into the snapping part of the vacuum lines. The sealed tube was snapped in the vacuum line and CO_2 and H_2O were released into the line. Using the two type of cold traps, the ethanol trap which is cooled to -100℃ and the liquid nitrogen trap (-196℃), we collected only CO_2 in the silica glass tube (9 ϕ , 35cm) which has iron powder. We also introduced hydrogen gas in the tube, and sealed this tube using the gas burner.

Then, the sealed tube was heated at 650℃ for 6 hours, and CO_2 was graphitised by hydrogen reduction. The reaction formula is following:

$$CO_2 + 2H_2 \xrightarrow{Fe\ cat.} C + 2H_2O \qquad (2)$$

When the graphitization process is finished, a graphite in the silica glass cup must be taken from the sealed tube immediately. The graphite samples were stored in a desiccator.

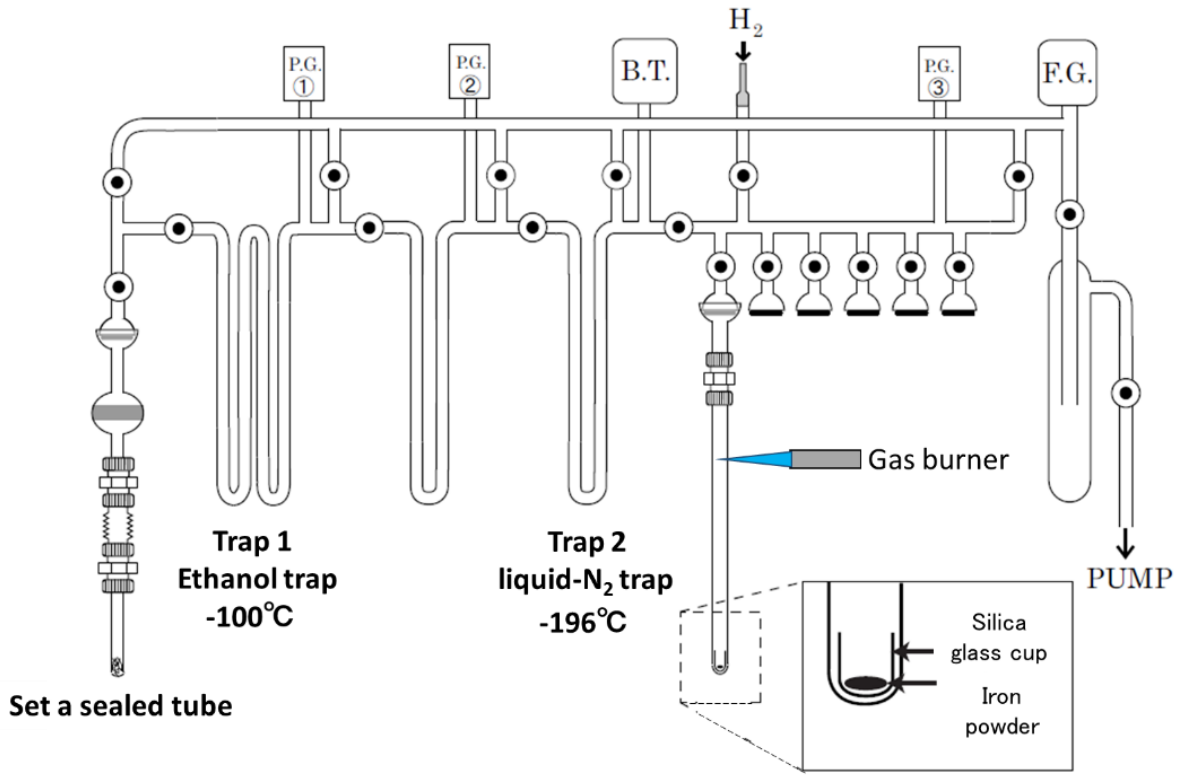

Figure 5-20: The vacuum line for the purification.

5-6 AMS measurement

We measured the ^{14}C content in graphite targets by using an accelerator mass spectrometer (AMS) at the Center for Chronological Research (CCR) in Nagoya University [*Nakamura et al.* 2003]. This AMS is made in the company of High Voltage Engineering Europe (HVEE) in the Netherlands, and consisted of an ion source, an ion accelerator, a mass spectrometry (magnet), and a detector regions. Figure 5-21 shows a schematic illustration of the AMS in Nagoya University.

For the AMS measurement, the graphite sample was pressed (2.0-2.1 kN) in the target holder and the target holders were set in the target wheel. To ionize the carbon atom ($^{12}C^-$, $^{13}C^-$, $^{14}C^-$), the graphite sample in the target holder was exposed by Cs^+ beam which is as narrow as 0.1mm in diameter. If the Cs^+ beam irradiates the only a narrow region on the target surface, the region would become a deep hole and this raises a cause of isotopic fractionation effect. To avoid this effect, the AMS system in Nagoya University introduces a sweeping method, that is, Cs^+ beam irradiates 9 small regions in rotation (figure 5-22).

Although the background isobaric ions such as $^{13}CH^-$ are produced at the time of the ionization of carbon, they are eliminated by the charge-changing canal and the heavy ion detector described below. The negative carbon ions enter to the accelerator section, then are accelerated by high voltage of 1.8-2.5 [MV], and collid with Ar gas in the charge-changing canal. As a consequense of this process, the carbon anions are changed to cations ($^{12}C^{3+}$, $^{13}C^{3+}$, $^{14}C^{3+}$) and the background molecule ions are decomposed. After the particles come out from the accelerator section, they are curved as a function of mass of carbon by the mass spectrometory electromagnet. A large number of $^{12}C^{3+}$and $^{13}C^{3+}$ go to faraday cups, and are measured as a current value. On the other hand, $^{14}C^{3+}$ is counted in a heavy ion detector.

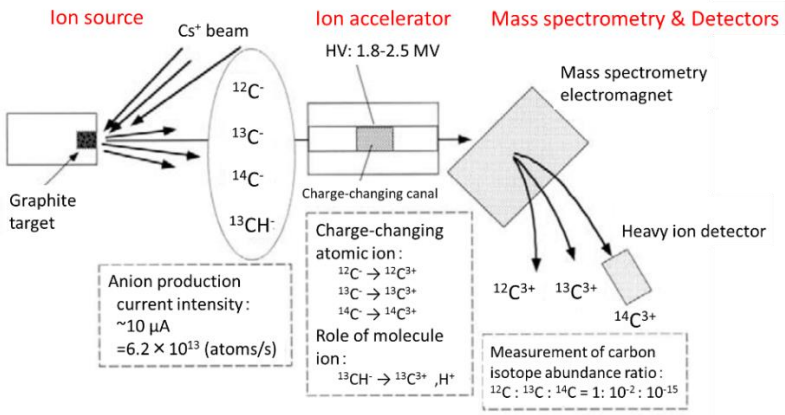

Figure 5-21: Schematic illustration of the AMS in Nagoya University. This is cited from *Nakamura* [2003] (touch up the original one).

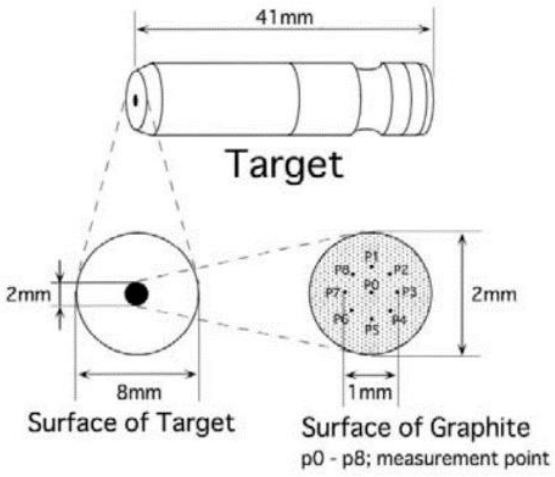

Figure 5-22: Schematic of target holder. Numbers P0-P8 indicate Cs^+ beam irradiation points. This figure is cited from *Nakamura* [2003].

5-7 Oxalic acid samples

Since AMS is a relative measurement, standard samples[9] should be measured in the same batch. Blank samples[10] for determination of the background are also measured. Six NIST standard samples and two blank samples were converted to graphite and their ^{14}C content were measured. The method of pretreatment of oxalic acid samples differ slightly from that of the wood samples. Differences are (1) no usage of sulfix, (2) use of the vacuum line B for evacuating the silica tube, and (3) gasification temperature of 450℃. Since the vapor pressure of oxalic acid is 3×10^{-2} [Pa] for 30℃, we sealed the oxalix acid samples when the pressure in the purification line is around 3×10^{-2} [Pa]. The reaction formula of gasification of the oxalic acid samples is following:

$$(COOH)_2 + CuO \rightarrow 2CO_2 + H_2O + Cu \qquad (3)$$

[9] NIST SRM4990C oxalic acid; the new NBS standard

[10] Commercial oxalic acid from Wako Pure Chemical Industries

5-8 Calculation of $\Delta^{14}C$ and errors

From the AMS measurement, we got a ratio of ^{14}C to ^{12}C ($^{14}C/^{12}C$). The concentration of ^{14}C expressed as $\Delta^{14}C$, which is the age and isotopic fractionation corrected value, was calculated according to the method by Stuiver and Polach [1977]. Details are the followings.

5-8-1 Age correction

Since ^{14}C is radioisotope with a half-life of 5,730 years, ^{14}C collapses as time advances since tree-rings take up CO_2 (tree-ring formation time). In order to know ^{14}C content at the formation time, we apply the age correction.

$$N_0 = N_t \, e^{\frac{t}{T_{1/2}} ln2} \quad , \qquad (4)$$

where N_0, N_t, and $T_{1/2}$ indicate the number of ^{14}C at tree-ring formation, number of ^{14}C after t years, and a half-time of ^{14}C (5730 ± 40 years), respectively.

5-8-2 Isotopic fractionation correction

Carbon is composed of two stable isotopes ^{12}C and ^{13}C, and a radioisotope ^{14}C. Their abundance ratio in nature is $^{12}C : {}^{13}C : {}^{14}C = 0.989 : 0.011 : 1.2 \times 10^{-12}$.

When plants absorb CO_2, difference of absorption rate of carbon isotopes occurs depending on species of plants or a growing environment for plants. This difference is called an isotopic fractionation effect and usually occurrs due to a difference of mass of carbons. The isotopic fractionation against ^{14}C is corrected by using $\delta^{13}C$ value which is shown in eq.(5). In this time, $\delta^{13}C$ is standardized to be the average value of trees, -25‰.

$$\delta^{13}C = \left[\left(\frac{^{13}C}{^{12}C} \right)_{Sample} \Big/ \left(\frac{^{13}C}{^{12}C} \right)_{PDB} - 1 \right] \times 1000 \; [‰] \qquad (5)$$

$$\left(\frac{^{13}C}{^{12}C} \right)_{After} = \alpha \times \left(\frac{^{13}C}{^{12}C} \right)_{Before} \qquad (6)$$

$$\alpha = \left(1 + \frac{-25}{1000} \right) \Big/ \left(1 + \frac{\delta^{13}C}{1000} \right) \qquad (7)$$

Where, α is an isotopic fractionation correction coefficient.

Since the isotopic fractionation effect is considered to be caused by a mass difference of carbon isotopes, we assumed that the effect occurs in ^{12}C : ^{13}C at the same rate as ^{13}C : ^{14}C. Then, that effect is shown as following equations:

$$\left(\frac{^{14}C}{^{12}C}\right)_{After} = \left(\frac{^{14}C}{^{13}C}\right)_{After} \times \left(\frac{^{13}C}{^{12}C}\right)_{After} \quad (8)$$

$$= \alpha^2 \times \left(\frac{^{14}C}{^{13}C}\right)_{Before} \times \left(\frac{^{13}C}{^{12}C}\right)_{Before} \quad (9)$$

$$= \alpha^2 \times \left(\frac{^{14}C}{^{12}C}\right)_{Before} \quad (10)$$

5-8-3 Calculation of $\Delta^{14}C$

Values of $\Delta^{14}C$ are calculated after the corrections of age and isotopic fractionation and stadardization by the intarnational standard value [*Stuiver & Polach* 1977], as shown in equations (11)-(19).

$$R_{Sample} = \left(\frac{^{14}C}{^{12}C}\right)_{Sample} - \left(\frac{^{14}C}{^{12}C}\right)_{Background} \quad (11)$$

$$R_{NIST} = \left(\frac{^{14}C}{^{12}C}\right)_{NIST} - \left(\frac{^{14}C}{^{12}C}\right)_{Background} \quad (12)$$

$$R'_{Sample} = {R_{Sample}}\Big/{\frac{1}{n}\sum_n R_{NIST}} \quad (13)$$

$$R''_{Sample} = \alpha^2 \times R'_{Sample} \quad (14)$$

$$= \left\{\left(1 + \frac{-25}{1000}\right)\Big/\left(1 + \frac{\delta^{13}C_{Sample}}{1000}\right)\right\}^2 \times R'_{Sample} \quad (15)$$

$$\delta^{13}C_{Sample} = \left[\frac{\left(\frac{^{13}C}{^{12}C}\right)_{Sample}}{\frac{1}{n}\sum_n\left(\frac{^{13}C}{^{12}C}\right)_{NIST}\Big/\left(1 + \frac{-17.8}{1000}\right)} - 1\right] \times 1000 \quad (16)$$

$$R'''_{Sample} = R''_{Sample} \times \frac{e^{\frac{y-x}{5730}ln2}}{e^{\frac{y-1950}{5730}ln2}} \times 1000 \quad (17)$$

$$R''''_{Sample} = R'''_{Sample}/0.7459 \quad (18)$$

$$\Delta^{14}C = \left(\sum_i \frac{R''''_{Sample}(i)}{\sigma(i)} \Big/ \sum_i \frac{1}{\sigma(i)^2} - 1\right) \times 1000 \quad (19)$$

Where, *n* is quantity of NIST standards, *i* is day number (measurement time of one day for each sample is ~30 minutes), *x* is date of sample, and *y* is date of measurement. The international ^{14}C standard value is calculated when we multiply 0.7459 to NIST standard sample. Error (σ) is described in next paragraph.

5-8-4 Errors

Since a measurement error of ^{14}C is a statistical error due to ^{14}C counts, an error of unknown sample is calculated by the error propagation of its statistical error and error of NIST standard samples. The total error of NIST standards is chosen to be larger value or the measured standard deviation of several NIST standards and averaged statistical error of the NIST standards (I will discuss later). Here, ^{14}C counts for an unknown sample and a NIST standard are N_{sample} and N_{NIST}, respectively. An error $\sigma_{sample}(i)$ for the day *i* is:

$$\sigma_{Sample}(i) = \sqrt{\left(\sqrt{N_{Sample}(i)}\right)^2 + \sigma^2_{NIST}(i)} \quad (20)$$

$$\frac{\sigma_{Sample}(i)}{R'_{Sample}(i)} = \sqrt{\left(\frac{\sqrt{N_{Sample}}}{N_{Sample}}\right)^2 + \left(\frac{\sigma_{NIST}}{N_{NIST}}\right)^2} \quad (21)$$

Here,

$$\sigma_{NIST} = \sqrt{N_{NIST}} \quad (or\ s.d. = \sqrt{\frac{(N_{NIST} - \overline{N_{NIST}})^2}{n-1}}) \quad (22)$$

$$\frac{\sigma_{Sample}}{R_{Sample}} = \sum_i \frac{1}{\sqrt{\left(\frac{\sigma_{Sample}(i)}{R'_{Sample}(i)}\right)^2}} \quad (23)$$

$$\Delta^{14}C_{error} = (\Delta^{14}C + 1000) \times \frac{\sigma_{Sample}}{R_{Sample}} \quad (24)$$

Chapter 6

Measurements & Results

6-1 The validation of the measurement results

We have judged the validity of ^{14}C measurment by using the follow criteria:

1) current value of ^{12}C

2) stability of several NIST standards

6-1-1 Check of the current values of ^{12}C

The measured current values of ^{12}C vary depending on a condition of the samples (i.e. if pieces of glass are mixed in graphite targets, a current value shows extremely-low). Empirically, less than 70% of mode of ^{12}C current value is often inaccurate, then we have excluded these data. Table 6-1 shows all measurement information, and figure 6-1 shows histgram of ^{12}C current of all measurements.

Table 6-1: Information of all measurement. They show measurement periods and sample number of each measurenet.

Date	Measured period [AD]	Quantity	Remark
Feb. 2010	664-710	24	
May 2010	844-894	26	
July 2010	790-846	29	

Aug. 2010	748-792	29	AD770*4, 772*4
Sep. 2010	644-654, 708-750, 804	29	
Oct. 2010	616-644, 654-666, 676, 686, 688, 698, 706	27	
Nov. 2010	774-780(1-yr), 894, 916, 946, 964-994	27	AD 976*2
Dec. 2010	602-618, 844-882	29	
Apr. 2011	668-706, 990-998(1-yr)	29	
May 2011	712-716, 720-734, 738-746, 752-768, 782-788	29	
June 2011	718, 794-842, 848-852	29	
July 2011	598-614, 620-636, 640-642, 646-652, 656-662	28	
Sep. 2011	767-773, 900-948	29	
Oct. 2011	950-962, 966-974, 978-988, 989-999(1-yr)	29	
Nov. 2011	773-779 (Yaku-A), 770-779 (Yaku-14ANb)	14	
Dec. 2011	1820-1856, 1857-1862(1-yr), 1864-1870	29	Yaku-B
Apr. 2012	594-600 (Yaku-A), 1790-1808, 1809-1816(1-yr), 1818-1822, 1857-1860(1-yr)	29	Yaku-B
May 2012	854-878, 884-894, 998-1016	29	
June 2012	1812-1816(1-yr), 550-596 (Yaku-A)	29	
Sep. 2012	1014-1070	29	
Oct. 2012	1070-1104(Yaku-A), BC701-BC721	29	Chokai
Nov. 2012	BC721-BC777	29	Chokai
June 2013	987-997	10	Iida Hinoki, AMS of Yamagata University

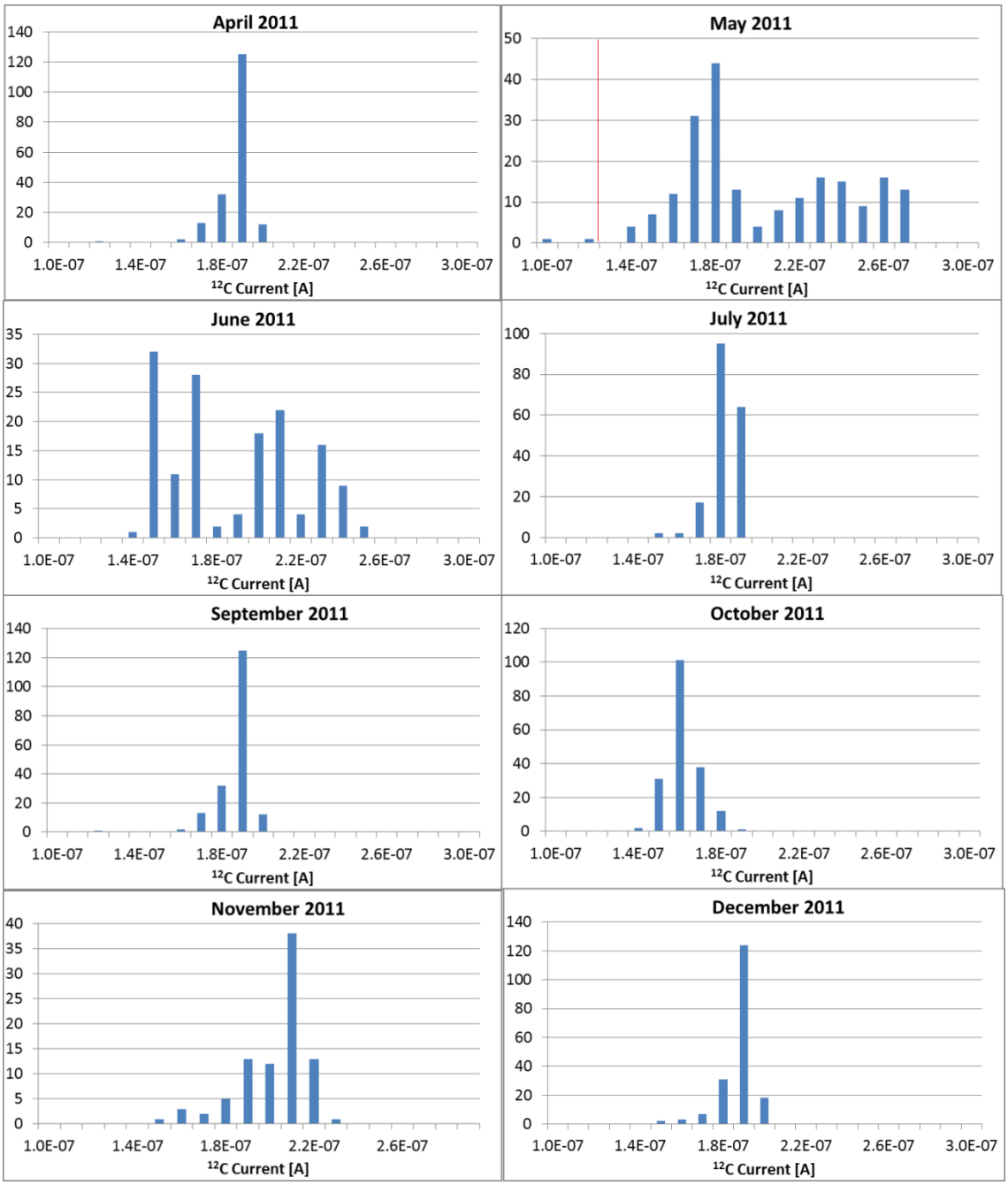
April 2011
140
120
100
80
60
40
20
0
1.0E-07
1.4E-07
1.8E-07
2.2E-07
2.6E-07
3.0E-07
12C Current [A]
May 2011
50
40
30
20
10
0
1.0E-07
1.4E-07
1.8E-07
2.2E-07
2.6E-07
3.0E-07
12C Current [A]
June 2011
35
30
25
20
15
10
5
0
1.0E-07
1.4E-07
1.8E-07
2.2E-07
2.6E-07
3.0E-07
12C Current [A]
July 2011
100
80
60
40
20
0
1.0E-07
1.4E-07
1.8E-07
2.2E-07
2.6E-07
3.0E-07
12C Current [A]
September 2011
140
120
100
80
60
40
20
0
1.0E-07
1.4E-07
1.8E-07
2.2E-07
2.6E-07
3.0E-07
12C Current [A]
October 2011
120
100
80
60
40
20
0
1.0E-07
1.4E-07
1.8E-07
2.2E-07
2.6E-07
3.0E-07
12C Current [A]
November 2011
40
35
30
25
20
15
10
5
0
1.0E-07
1.4E-07
1.8E-07
2.2E-07
2.6E-07
12C Current [A]
December 2011
140
120
100
80
60
40
20
0
1.0E-07
1.4E-07
1.8E-07
2.2E-07
2.6E-07
3.0E-07
12C Current [A]

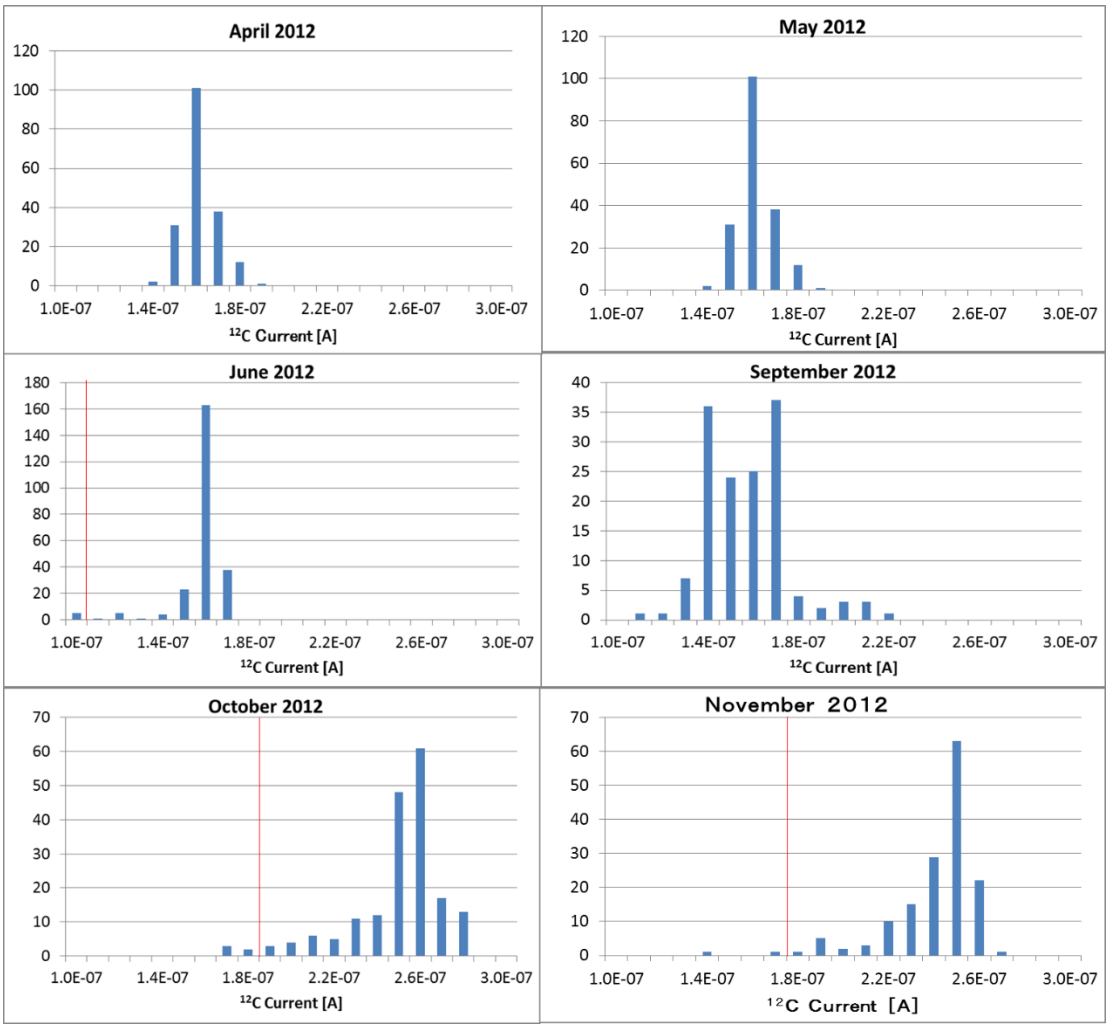

Figure 6-1: Histgrams of the ^{12}C current value. We did not use the data below red lines.

6-1-2 Stability of several NIST standards

Since we measured six NIST standard samples in each measurement run, we can check the stability of each AMS measurement by comparing the averaged statistical errors of NIST standards with the standard deviation of ^{14}C values of six NIST standards. If these two values are almost same, it is considered that the variability of values of standards is due to a statistical error. In other words, if these two values are significantly different, we can say that the AMS measurement is unstable. Table 6-2 shows these two values for all measurement turns.

In order to validate if the variability of NIST standards occurred due to the statistical error, we applied a chi-squared test. A χ^2 value of each NIST standard is calculated as:

$$\left[\left(\Delta^{14}C\ of\ each\ NIST\right) - \left(Averaged\ \Delta^{14}C\ of\ six\ NISTs\right)\right]^2 \Big/ \left(Statistical\ error\ of\ each\ NIST\right)^2$$

We summed χ^2 values of the six NIST standards, and calculated an upper probabilities. Since only the measurement in May 2010 has the upper probability less than 0.05 (= much larger than statistical errors), we did not use this measurement data. The cause of unstable measurement in May 2010 is considered to be due to the AMS trouble. The deviation of six NIST standard samples except for the May 2010 series was consistent with the statistical error.

When we calculate the error of $\Delta^{14}C$, we have used larger value between the averaged statistical errors of six NIST standards and the standard variation of six NIST standards (red-letter one in table 6-2) to avoid estimating the error to be too small.

Table 6-2: An evaluation of variability of NIST standards for each measurement run. Values in upper lines are averaged statistical errors of NIST standards, and those in lower lines are the measured standard deviation of ^{14}C values of NIST standards. We have used larger value (red-letter one) for calculating errors of $\Delta^{14}C$.

Measurement	Day 1	Day 2	Day 3	Day 4	Day 5
Feb. 2010	0.32	0.31	0.30		
	0.47	0.53	0.43		
May 2010	0.30	0.31	0.32	0.31	
	0.89	0.93	0.88	1.00	
July 2010	0.31	0.30	0.29	0.31	
	0.39	0.54	0.33	0.21	
Aug. 2010	0.31	0.31	0.31	0.31	
	0.31	0.46	0.30	0.14	
Sep. 2010	0.33	0.32	0.31	0.32	
	0.29	0.24	0.44	0.32	
Oct. 2010	0.35	0.34	0.33	0.34	
	0.40	0.31	0.23	0.46	
Nov. 2010	0.31	0.30	0.30	0.30	0.33
	0.43	0.35	0.35	0.15	0.65

Dec. 2010	0.31	0.31	0.27	0.35	0.35
	0.13	0.38	0.22	0.64	0.30
Apr. 2011	0.36	0.34	0.34	0.35	0.34
	0.51	0.48	0.35	0.26	0.47
May 2011	0.37	0.35	0.29		
	0.48	0.29	0.36		
June 2011	0.39	0.37	0.34	0.33	
	0.30	0.35	0.44	0.51	
July 2011	0.35	0.35	0.36	0.36	0.36
	0.35	0.31	0.54	0.55	0.27
Sep. 2011	0.37	0.38	0.38	0.36	0.36
	0.47	0.38	0.26	0.40	0.20
Oct. 2011	0.43	0.40	0.38	0.38	0.38
	0.55	0.56	0.38	0.45	0.18
Nov. 2011	0.33	0.32	0.32	0.32	
	0.35	0.28	0.50	0.40	
Dec. 2011	0.36	0.34	0.35	0.35	0.35
	0.35	0.20	0.59	0.63	0.50
Apr. 2012	0.29	0.28	0.28	0.29	
	0.22	0.36	0.31	0.23	
May 2012	0.37	0.36	0.36	0.36	0.37
	0.35	0.16	0.36	0.53	0.34
June 2012	0.39	0.38	0.38	0.38	0.38
	0.28	0.31	0.67	0.25	0.34

Sep. 2012	0.38	0.39	0.36		
	0.62	0.21	0.13		
Oct. 2012	0.29	0.29	0.30	0.30	0.31
	0.50	0.28	0.19	0.31	0.23
Nov. 2012	0.30	0.30	0.31	0.32	
	0.23	0.19	0.26	0.22	

6-2 $\Delta^{14}C$ measurement data

As described above, we have checked the measured data and have excluded the unusual data. Typical precision of single measurements was 2.6 ‰. These obtained data ($\Delta^{14}C$, error of $\Delta^{14}C$, and $\delta^{13}C$) are presented in the Appendix A, and the $\Delta^{14}C$ data for each measurement series are shown in figure 8-1 ~8-3 (in section 8).

Since the data for overlapping years match within measurement errors, these series of measurements are reproducible and we applied weighted averaging for the same year.

Chapter 7

Discussions ~AD 775 event~

7-1 The AD 775 event

We used two individual Japanese cedar trees (Yaku-A, Yaku-B) to investigate the rapid increase from AD 775 to 785 which is shown in the decadal IntCal data [*Reimer et al.* 2009]. We collected two series of measurements of the ^{14}C content in Yaku-A. The first consists of biennial measurements from AD 750 to AD 820. The second consists of yearly measurements from AD 774 to AD 780. The data for overlapping years match within measurement errors, confirming that the two series of measurements are reproducible. The measurement of ^{14}C content in Yaku-14ANb was collected at one-year resolution, from AD 770 to AD 779. The data from Yaku-A and Yaku-14ANb are consistent with the measurement errors.

Figure 7-1 shows the variation of ^{14}C content ($\Delta^{14}C$) for the period from AD 750 to AD 820 after the two series of data were combined. The IntCal98 data [*Stuiver et al.* 1998a] are also shown for comparison. Althouth the IntCal decadal data show the ^{14}C content increase of 7.2‰ over 10 years (AD 775-785), it turns out that this increase was within 1 year from AD 774 to AD 775. The increment from AD 774 to AD 775 is about 12 ‰, which corresponds to 7.2σ against the measurement errors.

7-1-1 Comparison with IntCal dataset

To compare our results with IntCal98 dataset, we averaged the yearly data to obtain a series with decadal time resolution. The result is shown in Figure 1b. The two series are consistent with each other within measurement errors. This event causing elevated ^{14}C content in AD 775 could not have been local, because the IntCal data were obtained from North American and European trees while we used Japanese trees.

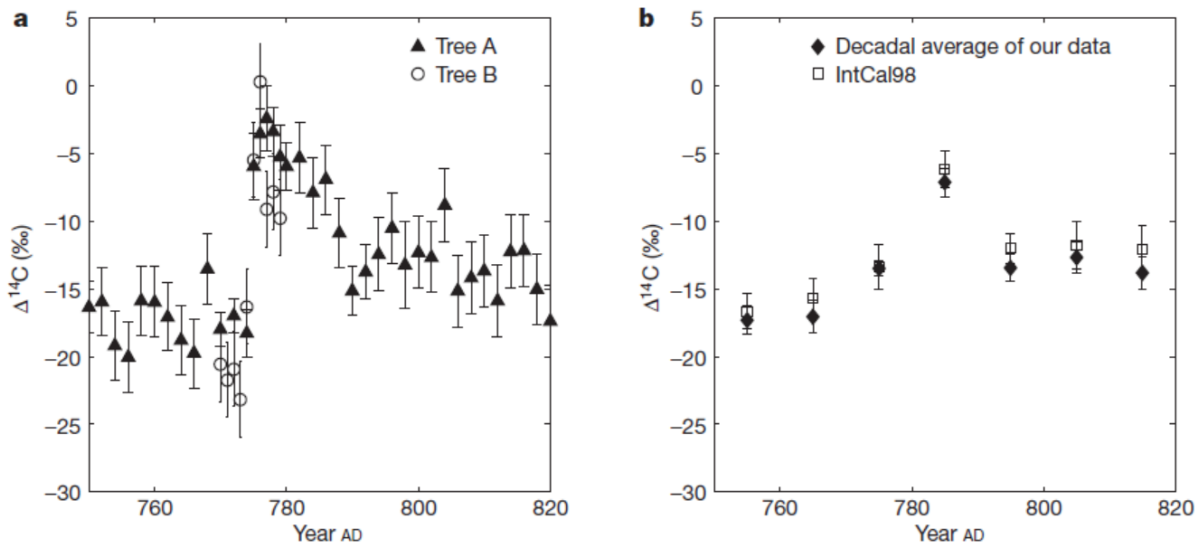

Figure 7-1: Measured data of radiocarbon content and comparison with IntCal. (a) $\Delta^{14}C$ data for Tree-A (triangles with error bars) and Tree-B (circles with error bars) for the period 750-820 AD with 1 or 2 year resolution. The typical precision of a single measurement of $\Delta^{14}C$ is 2.6‰. Most data were obtained by multiple measurements, yielding smaller errors. (b) The decadal average of our data (diamonds with error bars) compared with the IntCal98 data [*Stuiver et al.* 1998a] (squares), which is a standard decadal $\Delta^{14}C$ time series.

7-1-2 European & New Zealander tree

After the discovery of the AD 775 event in the Japanese cedar tree-rings, some have measured the ^{14}C content in other tree rings around AD 775 to verify the existence of this event. *Usoskin et al.* [2013] used German oak (*Quercus*) tree-rings (from the river Main in southern Germany: the German Oak Chronology [*Friedrich et al.* 2004]). And they measured ^{14}C content in two Accelerator Mass Spectrometer (AMS), i.e. Mannheim (MAMS) and ETH zurich (ETH), for the period of AD 770 to AD 780 with one year resolution. *Güttler et al.* [2013, poster] used New Zealander Kauri (*Agathis australis*) tree-rings and German oak tree-rings, and measured ^{14}C content in AMS of ETH, for the period of AD 760 to AD 788. These results are shown in figure 7-2 and figure 7-3, respectively.

Although there are differences in ^{14}C content between these series, especially the New Zealand series shows lower ^{14}C value than the others (this is considered to be due to the offset of Southern Hemisphere), a rapid ^{14}C increase about 15‰ from AD 774 to AD 775 are shown in all measurement series. Also their results are all consistent with each other within measurement errors. Therefore, these measurements made the AD 775 event more reliable, and this event was global and caused by the enhanced production of ^{14}C.

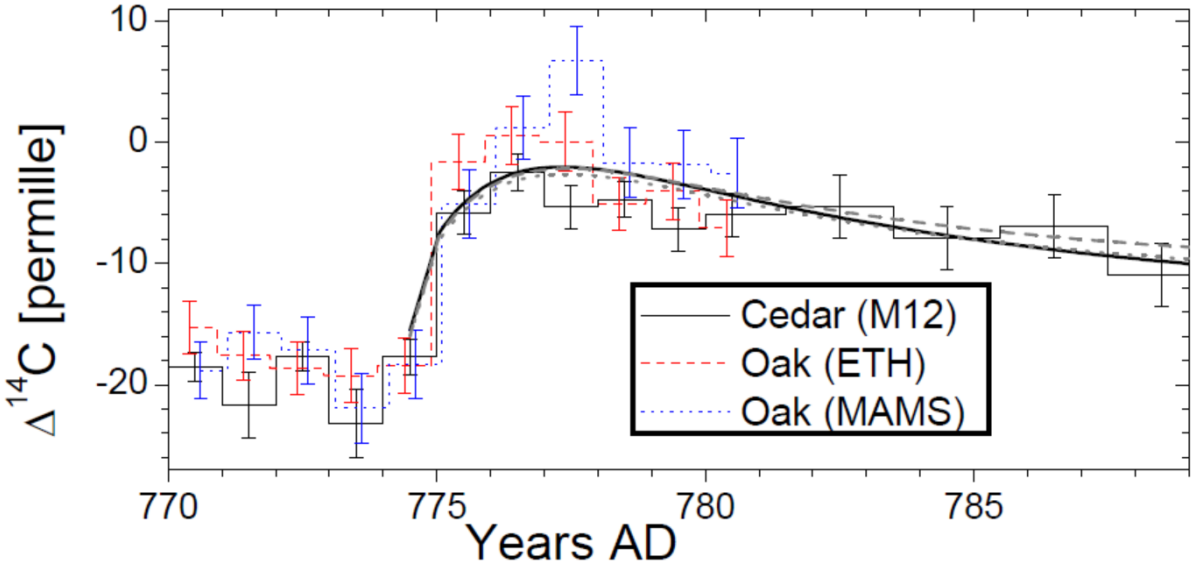

Figure 7-2: The comparison of ^{14}C content in Japanese cedar trees and German oak trees. The lines show best fit series of the calculation of a carbon cycle model. This graph is cited from *Usoskin et al.* [2013].

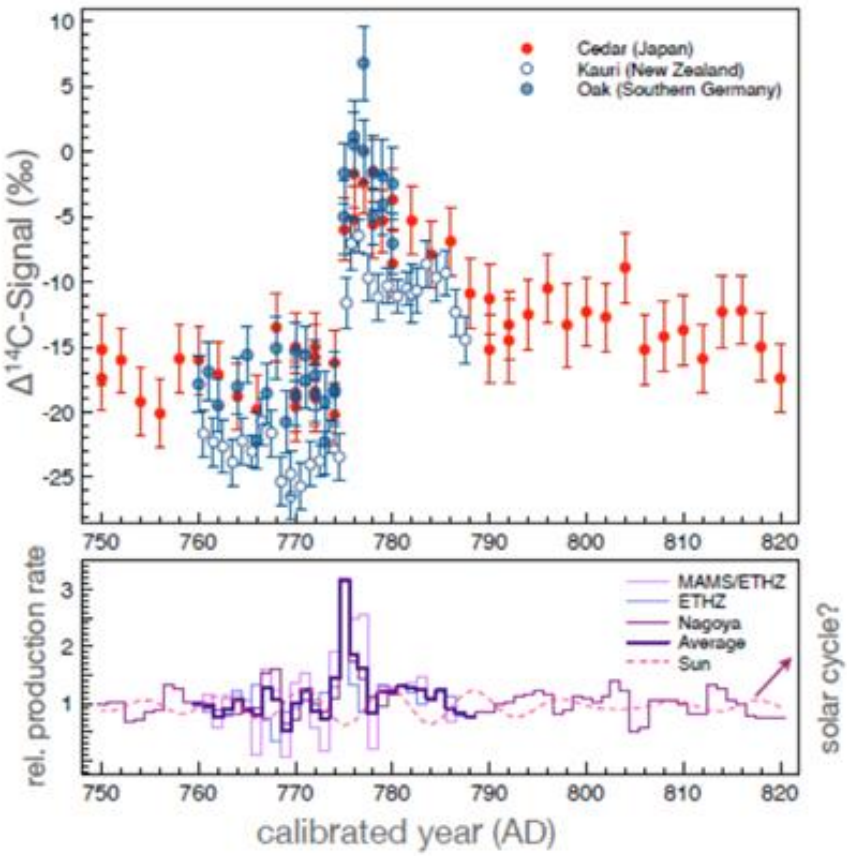

Figure 7-3: The comparison of ^{14}C content in Japanese cedar, German oak and Kauri trees. This graph is cited from the poster by *Güttler et al.* [2013]. They calculate production rate during this period, and compare with a variability of ^{14}C production caused by the Schwabe cycle of about 30% (bottom).

7-1-3 Comparison with ^{10}Be record

In order to produce a large number of ^{14}C nuclei in the atmosphere in AD 775, the cosmic ray intensity must have considerably increased. The decadal record of another cosmogenic nuclide, ^{10}Be, can be obtained in the layers of ice or snow from Dome Fuji in Antarctica. These data include the relevant period, and exhibit a sharp peak in the ^{10}Be flux around AD 775. However, the dating of ice core layers is more ambiguous than tree rings. The age of a layer is determined by locating several well-known volcanic events, and matching the production rate pattern of ^{10}Be with the ^{14}C production record reconstructed using the IntCal data. Figure 7-4 shows ^{10}Be flux data in Dome Fuji and the age matching date between ^{10}Be flux and ^{14}C production rate. While we cannot say with certainty that the ^{10}Be peak in the ice core occurred in AD 775, it is possible that the two peaks have the same cause.

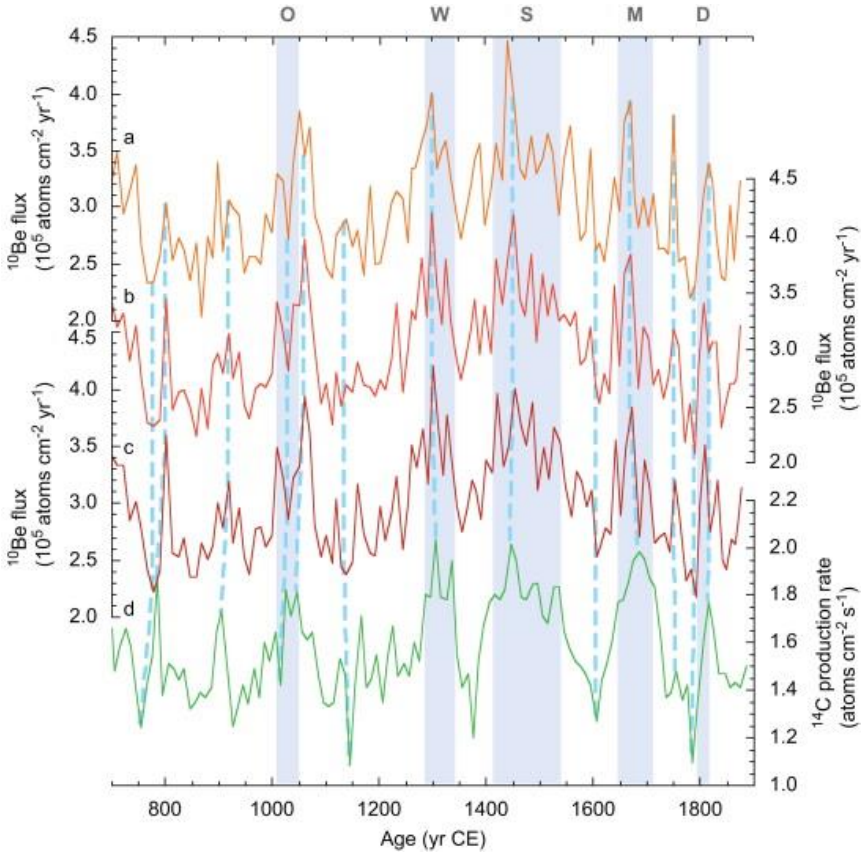

Figure 7-4: Some ^{10}Be flux time profiles (a: three-point averaged, b: five-point averaged, c: corrected by the snow accumulation rate) and ^{14}C production rate (d). The age of the ^{10}Be series is corrected by the ^{14}C production rate (^{10}Be-^{14}C stratigraphic dating). This graph is cited from *Horiuchi et al.* [2008].

7-2 Carbon cycle model

A characteristic variation of the AD 775 event is a rapid ^{14}C increase with 1-yr followed by a decay. The most pronounced increase of atmospheric ^{14}C content in the history was seen in the 1950s to the 1960s. This increase was caused by many tests of nuclear explosion in the atmosphere and is called the "bomb effect" (figure 5-2 in chapter 5). Since a nuclear test in the atmosphere was banned in AD 1963, the ^{14}C content after AD 1963 shows a decay by a global carbon cycle. The shapes of the ^{14}C variation in the bomb effect and that in our data around AD 775 are very similar. Therefore, it is considered that the decay of the AD 775 event is due to the carbon cycle.

In order to model the tree ring data, we simulated the variations of ^{14}C content using a 4-box carbon cycle model with a short-term increase in the ^{14}C production rate, based on the 3-box model [*Nakamura et al.* 1987]. The box of this model consists of the stratosphere, the troposphere, the marine surface, and the biosphere. The exchange coefficient between boxes was decided by the measured ^{14}C value of the Bomb effect peak. We used a current value for the quantity of carbon in each box. Figure 7-5 shows a detail of this model. We input a ^{14}C production into the stratosphere box for a short term, and observed the following ^{14}C variation in the troposphere box as a variation in tree-rings. Figure 7-6 indicates the time profiles of the ^{14}C variation of each box in case that a quantity and a duration of ^{14}C input (Q) are 1.5×10^8 atom/cm^2 and 1 year respectively.

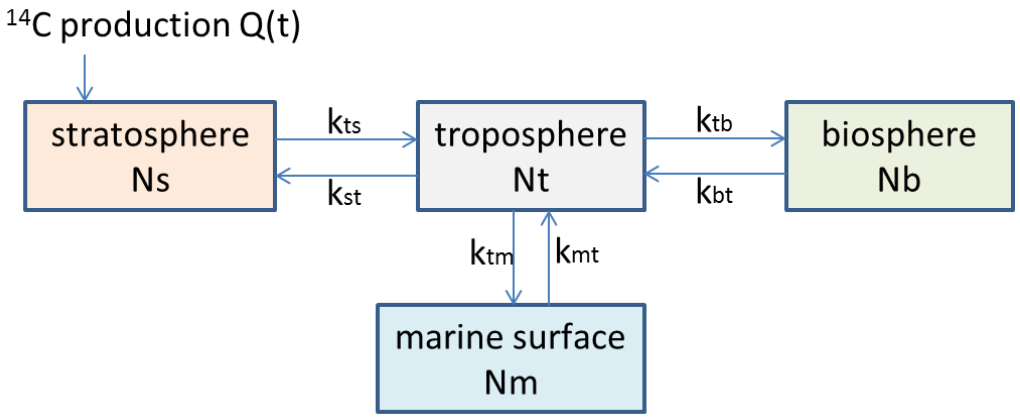

Figure 7-5: The 4-box carbon cycle model which is obtained by adding the stratosphere to the 3-box model [*Nakamura et al.* 1987]. We used the following parameters; k_{ts}=1/3 [1/yr], k_{tb}=1/23 [1/yr], k_{tm}=1/11 [1/yr], N_s/N_a=0.15, N_t/N_a=0.85, N_b/N_a=2.52, N_m/N_a=2, $N_a=N_t+N_s$. Where, N indicate the total amount of ^{12}C. Subscripts t, s, b, and m represent troposphere, stratosphere, biosphere, and surface ocean water, respectively. The transfer coefficient of carbon from one reservoir (i) to another (j) is indicated as k_{ij}, and the mean residence time as $\tau_{ij} = 1/(k_{ij})$.

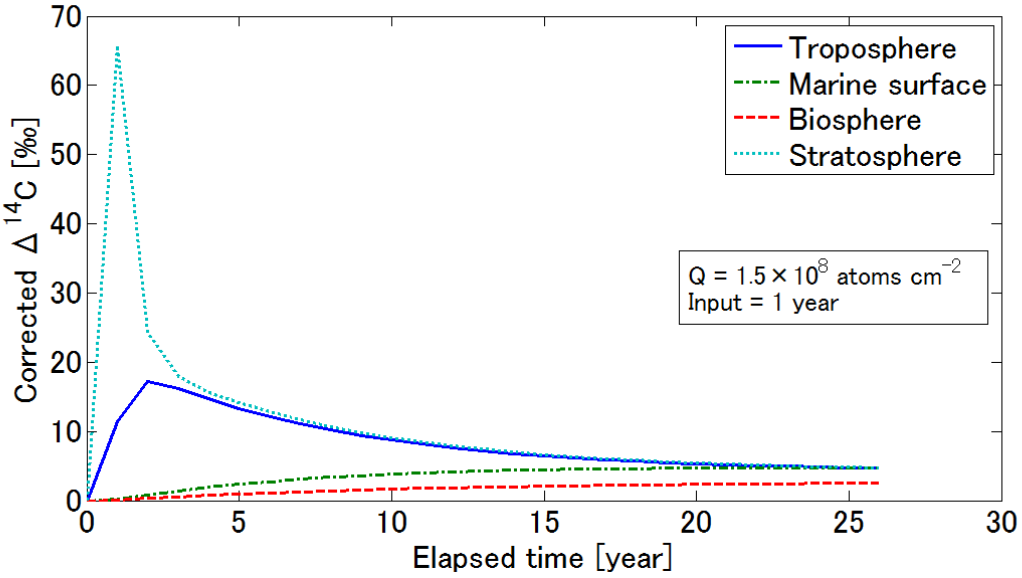

Figure 7-6: The ^{14}C time profiles of the ^{14}C variation of each box (stratosphere, troposphere, biosphere, and marine boxes).

7-2-1 ^{14}C production rate

Using this 4-box model, we can calculate the hypothetical ^{14}C production rates needed to explain a rapid increase in the annual time series, for input durations of 0.1, 0.5, 1, 2, and 3 years. We have used our data from AD 773 to 796 (annual data for AD 773-780, biennual data for 780-796).

We should also consider the period when the tree takes in CO_2. Since the period when a Yaku-cedar fixes carbon in tree-rings is from early-May to mid-November (see chapter 5-3), we calculated ^{14}C content of the model using this period. In addition, we set the event start date in every 2 months, and calculated one-sided probabilities by the chi-squared test for each event start date and each production rate around best fit value (we have valuated the degree of coincidence by a chi-squared test). Five graphs in figure 7-7 show the one-sided probability value against the event start date and the production rate in case that the ^{14}C input period is 0.1, 0.5, 1, 2, 3 years from above. The white lines corresponds to the one-sided probability values are 0.05 confidence level. We can consider this white line as an errors from measurements. The best-fit values of the input ^{14}C production rate and the event start date for each input durations are provided in table 7-1. Figure 7-8 shows comparisons of our data with a 4-box carbon cycle simulation for the input of 0.1, 0.5, 1, 2, 3 years. The models show good agreement with tree ring data for a sudden increase followed by a decay.

Although the best fitted production rates for the input period of 0.1, 0.5, 1, and 2 years show high confidence levels (>0.05), the confidence becomes less than 0.05 in case of the input period is 3 year (probability of the best fitted point is 0.04). Then, we can exclude a case of the ^{14}C input period is more than 3 years for the 775 event. Since as the input period increases, the agreement of the model with the measured data decreases, it is possible that the present data are consistent with a short-term (<~0.1 year), high-energy event. However, we cannot exclude the case of the ^{14}C production lasting 1-2 years. And we cannot assess the duration of this spike in more detail owing to the annual resolution of the ^{14}C data.

Although the best fit values of the event start dates distribute from July, 773 to January, 775 according to the input durations, these values have large errors. In case of the input period is less than 1-yr, the event start date could be from early 774 to early 775.

If the input period of ^{14}C production was 1 year, the production rate must have been 1.5×10^8 atoms cm^{-2} (table 7-1) to explain the effects of this event. This is about 2 times larger than the global average production rate by galactic cosmic rays (that is 6.5×10^7 atoms cm^{-2} [*Masarik & Beer*, 2009]).

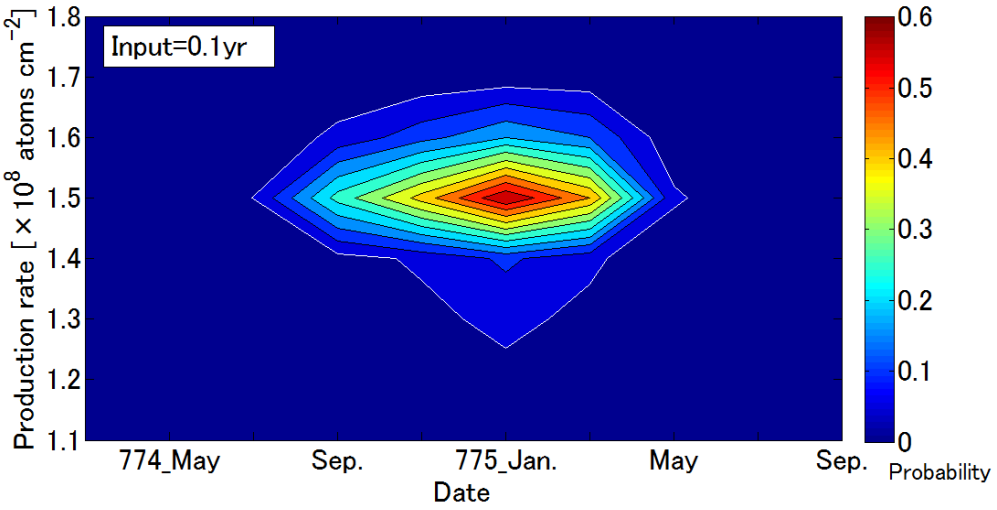

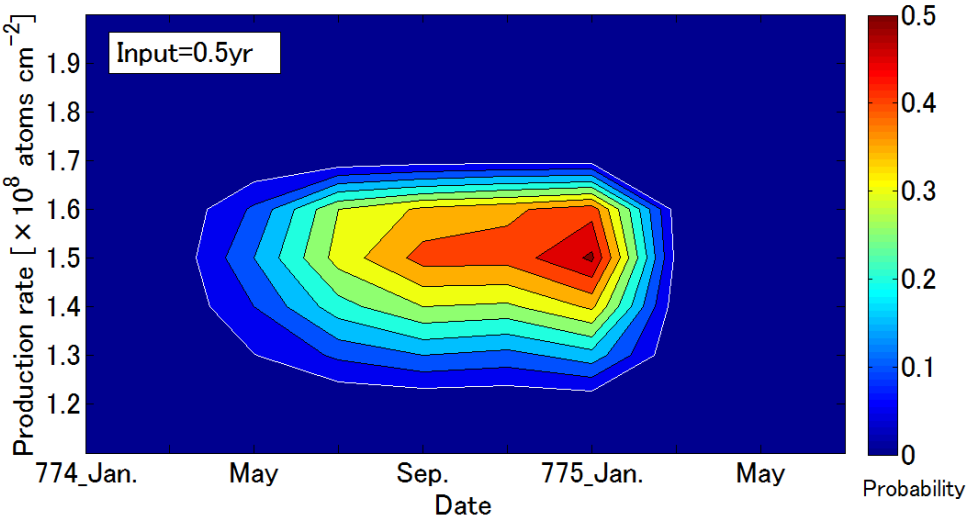
Input=0.5yr
Production rate [× 10^8 atoms cm^-2]
1.9
1.8
1.7
1.6
1.5
1.4
1.3
1.2
774_Jan.
May
Sep.
775_Jan.
May
Date
0.5
0.4
0.3
0.2
0.1
0
Probability

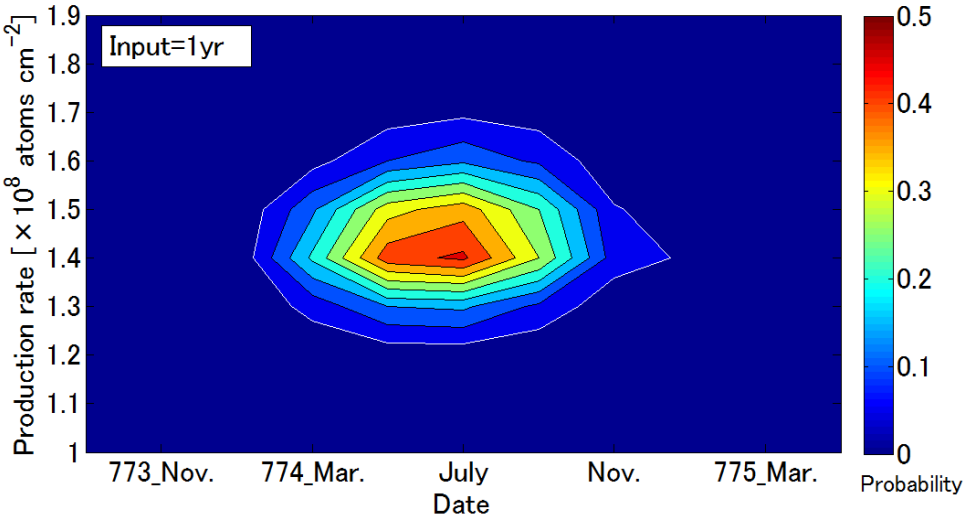
Input=1yr
Production rate [× 10^8 atoms cm^-2]
1.9
1.8
1.7
1.6
1.5
1.4
1.3
1.2
1.1
1
773_Nov.
774_Mar.
July
Nov.
775_Mar.
Date
0.5
0.4
0.3
0.2
0.1
0
Probability

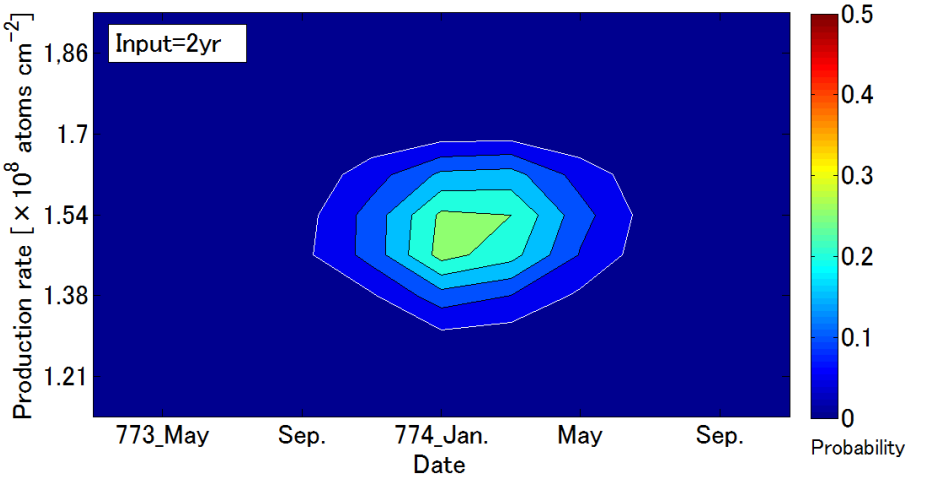
Input=2yr
Production rate [× 10^8 atoms cm^-2]
1.86
1.7
1.54
1.38
1.21
773_May
Sep.
774_Jan.
May
Sep.
Date
0.5
0.4
0.3
0.2
0.1
0
Probability

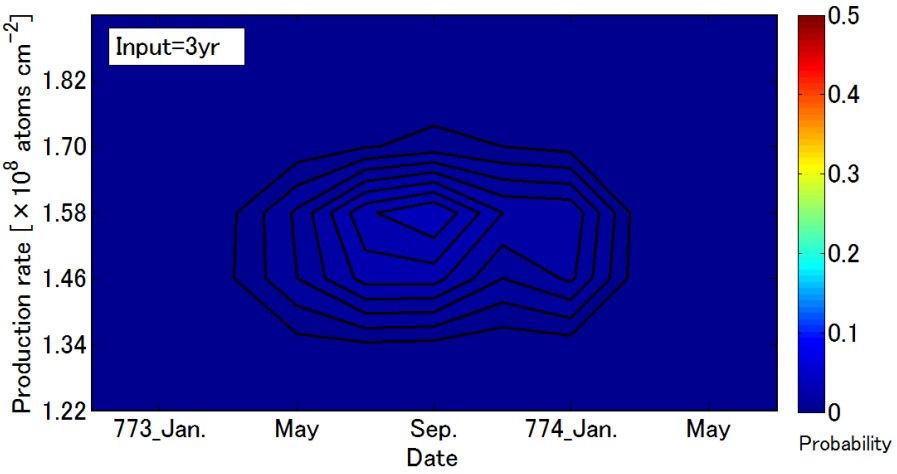

Figure 7-7: One-sided probability value for the ^{14}C input period is 0.1, 0.5, 1, 2, 3 year from above. The horizontal line shows the event start date (input start date), the vertical line shows the production rate, and the color shows one-sided probability value.

Table 7-1: Best fitted production rate of ^{14}C, the one-sided probability value, and the event start date for the ^{14}C input period is 0.1, 0.5, 1, 2, 3 year. The one-sided probability value is calculated by the chi-squared test (DOF=15). The errors of the production rates are obtained as 0.05 significance level.

Input period [yr]	Production rate [atom cm^{-2}]	One-sided probability	Event start date
0.1	$(1.5 \pm 0.2) \times 10^8$	0.60	January, 775
0.5	$(1.5 \pm 0.2) \times 10^8$	0.51	January, 775
1	$(1.5 \pm 0.2) \times 10^8$	0.49	July, 774
2	$(1.5 \pm 0.2) \times 10^8$	0.27	January, 774
3		0.04	September, 773

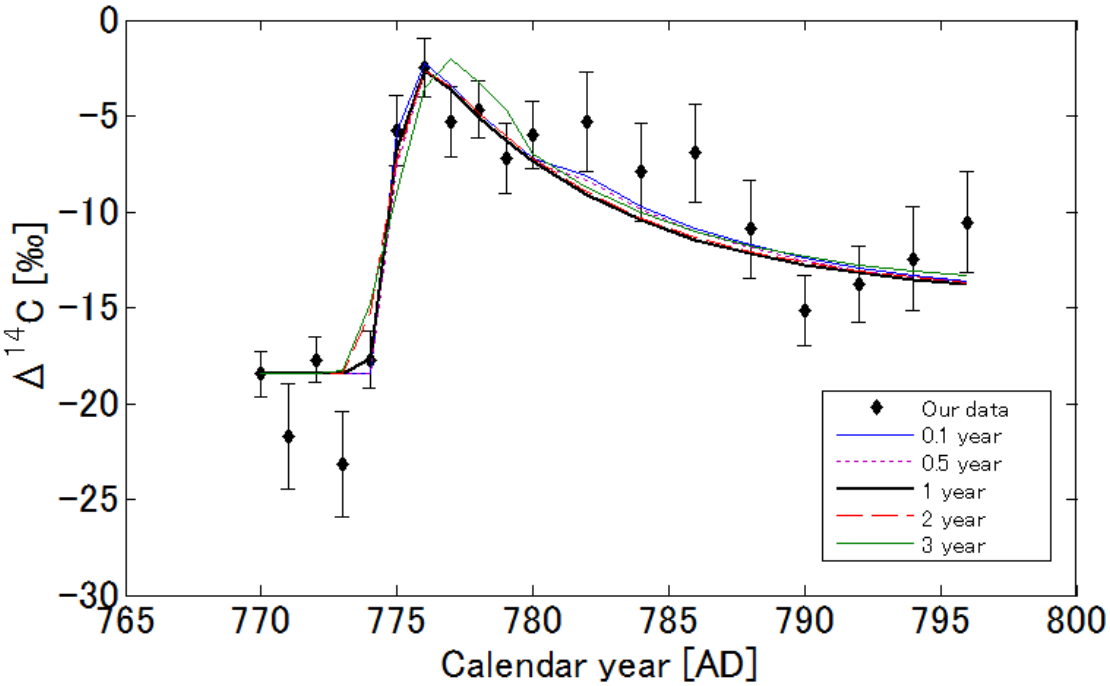

Figure 7-8: Comparison of our data with a 4-box carbon cycle simulation. Diamonds represent $\Delta^{14}C$ of our data and lines represent 4-box carbon cycle simulation. Various lines represent different cosmic-ray input durations of 0.1, 0.5, 1, 2 and 3 years. The $\Delta^{14}C$ value in AD 772 of the simulation is fixed at a value calculated by the weighted average of the three data from AD 770 to 772.

7-2-2 Model by Usoskin et al.

In our original paper [*Miyake et al.* 2012], we calculated the best fitted production rate for the 775 event as 6×10^8 atoms/cm^2. After our paper was published, *Usoskin et al.* [2012, 2013] has revisited the AD 775 event and calculated a ^{14}C production rate for this event using other carbon cycle models. One of their model is five-box model shown in figure 7-9, which consists of a stratosphere, a troposphere, a biosphere, a marine surface, and a deep ocean boxes. This model assumes that 70% of ^{14}C is produced in the stratosphere and 30% is in the troposphere. They claimed that the biggest difference between theirs and our model is having the deep ocean box or not, and a difference of the evaluations of the background ^{14}C level [*Usoskin et al.* 2013, and private communications]. We used a modern ^{14}C level for our carbon cycle model, but they took background ^{14}C level as the mean pre-industrial production rate of 1.6 atoms/cm^2. They concluded that the production rate is $(1.3 \pm 0.2) \times 10^8$ atoms/cm^2 which corresponds to 5 times smaller than our result.

However, the reason of the different result is the definition of the production rate. That is, we calculated the production rate as ^{14}C atoms/(π R^2), while, they calculated as ^{14}C atoms/(4 π R^2). If we calculated using ^{14}C atoms/(4 π R^2), the production rate becomes (1.5 ± 0.2)×10^8 atoms/cm^2, and this value is consistent with the result of *Usoskin et al.* 2013. In this case, the total global production is almost same as their calculation. Therefore, it is considered that following discussions about an energy estimation of the event origin are reasonable one. The calculation method of ^{14}C production rate in section 7-2-1 is ^{14}C atoms/(4 π R^2).

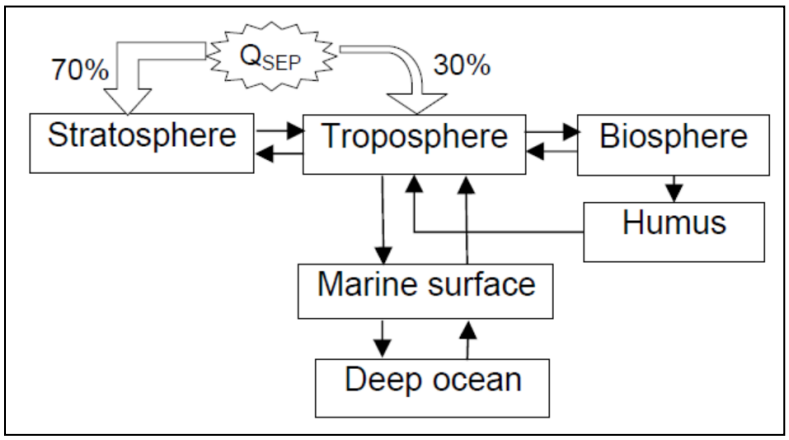

Figure 7-9: The carbon cycle models which is used in *Usoskin et al.* [2013].

7-3 Geant4 simulation

We computed the production rate of ^{14}C which is produced by protons and gamma rays using the GEANT4 simulation code with QGSP-BERT-HP (valid for thermal neutron interactions) [ref. 17]. We put incident particles (protons or gamma-rays) of a single energy to an ideal atmosphere (the U.S. standard atmosphere, 1976) and obtained the number of the generated ^{14}C. Figure 7-10 shows the schematic of our calculation.

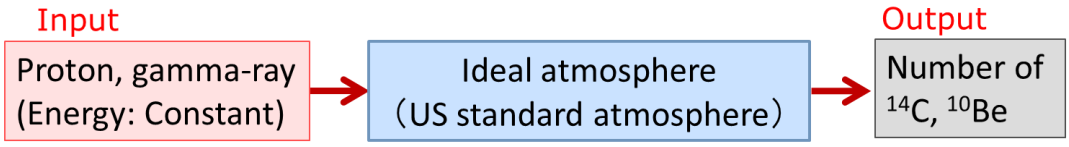

Figure 7-10: Schematic view of the GEANT4 simulation.

We got the production rate (P_1 = produced ^{14}C number / input particle number) for each single energy incidence. These production rates are listed in table 7-2, table 7-3 and are shown in figure 7-11. Our result of the ^{14}C production rate in the case of proton input is consistent with the one of *Castagnoli* [1980] whose result is shown in figure 7-12. I show the reaction process pattern of ^{14}C production in a case of 70MeV proton incidence and the 10,000MeV gamma ray incidence in table 7-4 as an example (I also show reaction process of ^{10}Be production in table 7-4).

After we got the production rate per incident particle number (P_1), we have calculated a production rate per energy [atoms/erg] (=P_2). Figure 7-13 shows the P_2 of the proton case and the gamma-ray case.

Table 7-2: The result of the GEANT4 simulation in case that input particle is set protons. The ^{14}C production rate (P_1) is calculated by number of output ^{14}C particles divided by number of input proton particles.

Input energy [MeV]	Input particles	Output ^{14}C	^{14}C production rate (P_1) [^{14}C Out/In]
50	10,000	43	0.0043
70	100,000	1,064	0.011
100	100,000	2,860	0.029
300	20,000	8,272	0.41
1,000	5,000	15,161	3.0
3,000	2,000	15,923	8.0
10,000	1,500	22,368	14.9
30,000	1,600	36,003	22.5
100,000	800	32,273	40.3

Table 7-3: The result of the GEANT4 simulation in case that input particle is set gamma-rays. The ^{14}C production rate (P_1) is calculated by number of output ^{14}C particles divided by number of input protons.

Input energy [MeV]	Input particles	Output ^{14}C	^{14}C production rate (P_1) [^{14}C Out/In]
15	1,000,000	408	4.1×10^{-4}
20	1,000,000	9057	9.1×10^{-3}
25	2,000,000	29,616	0.015
30	2,000,000	24,946	0.012
40	900,000	6,398	7.1×10^{-3}
50	1,000,000	5,206	5.2×10^{-3}
70	800,000	3,948	4.9×10^{-3}
100	600,000	4,030	6.7×10^{-3}
150	380,000	4,459	0.012
200	250,000	5,014	0.020
500	110,000	6,635	0.060
1,000	120,000	14,466	0.12
10,000	1,000	1,361	1.4

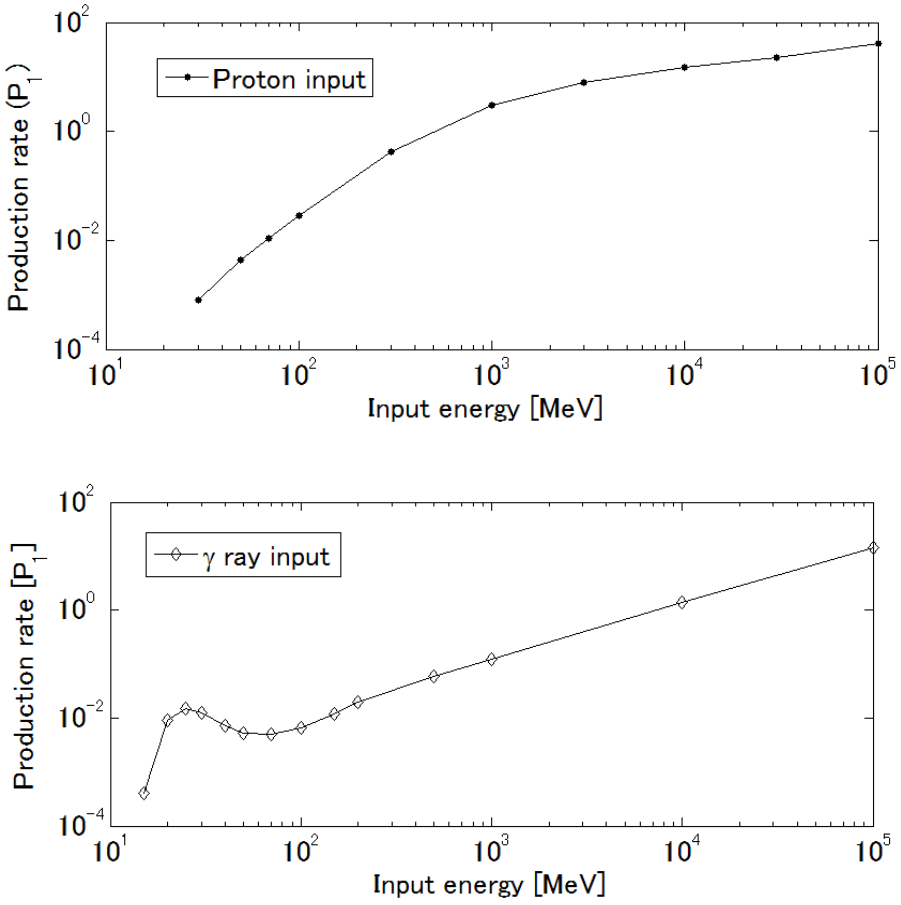

Figure 7-11: ^{14}C production rate P_1 (produced number / input particle number). (Upper) Input particles are protons, and (Lower) Input particles are gamma-ray.

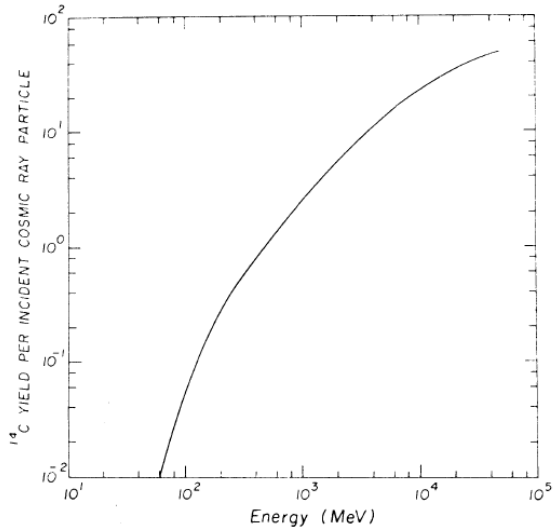

Figure 7-12: The result of ^{14}C production rate for each energy of incident cosmic ray. This graph is cited from *Castagnoli* [1980] and is consistent with our simulation result.

Table 7-4: Reaction process pattern of ^{14}C and ^{10}Be production in a case of 70 MeV proton incidence (upper) and the 10,000 MeV gamma ray incidence (bottom).

＜Input particle: protons＞

Input energy	Input protons	Output ^{14}C (reaction process)	Output ^{10}Be (reaction process)
70 [MeV]	100,000	1004 (n,p)	3 (n,p, α)
		1 (n,p,D)	1 (p,p,p,p, α)
		54 (p,p,p,p)	1 (p,p,p,p,p,n)
		5 (n,p,p,n)	1 (p,p,p,p,D)

＜Input particle: gamma-rays＞

Input energy	Input γ -rays	Output ^{14}C (reaction process)	Output ^{10}Be (reaction process)
10,000 [MeV]	1,000	1334 (n,p)	1 (γ,p,^{3}He)
		23 (γ,p,p)	2 (n,p,p,p,n,n)
		1 (e,p,p)	2 (γ,p,p,p, n)
		3 (n,p,p,n)	1 (n,p,p,n,D)
			1 (n,p,p,p, π^{+},n,n,n,n)
			1 (γ,p,p, α)

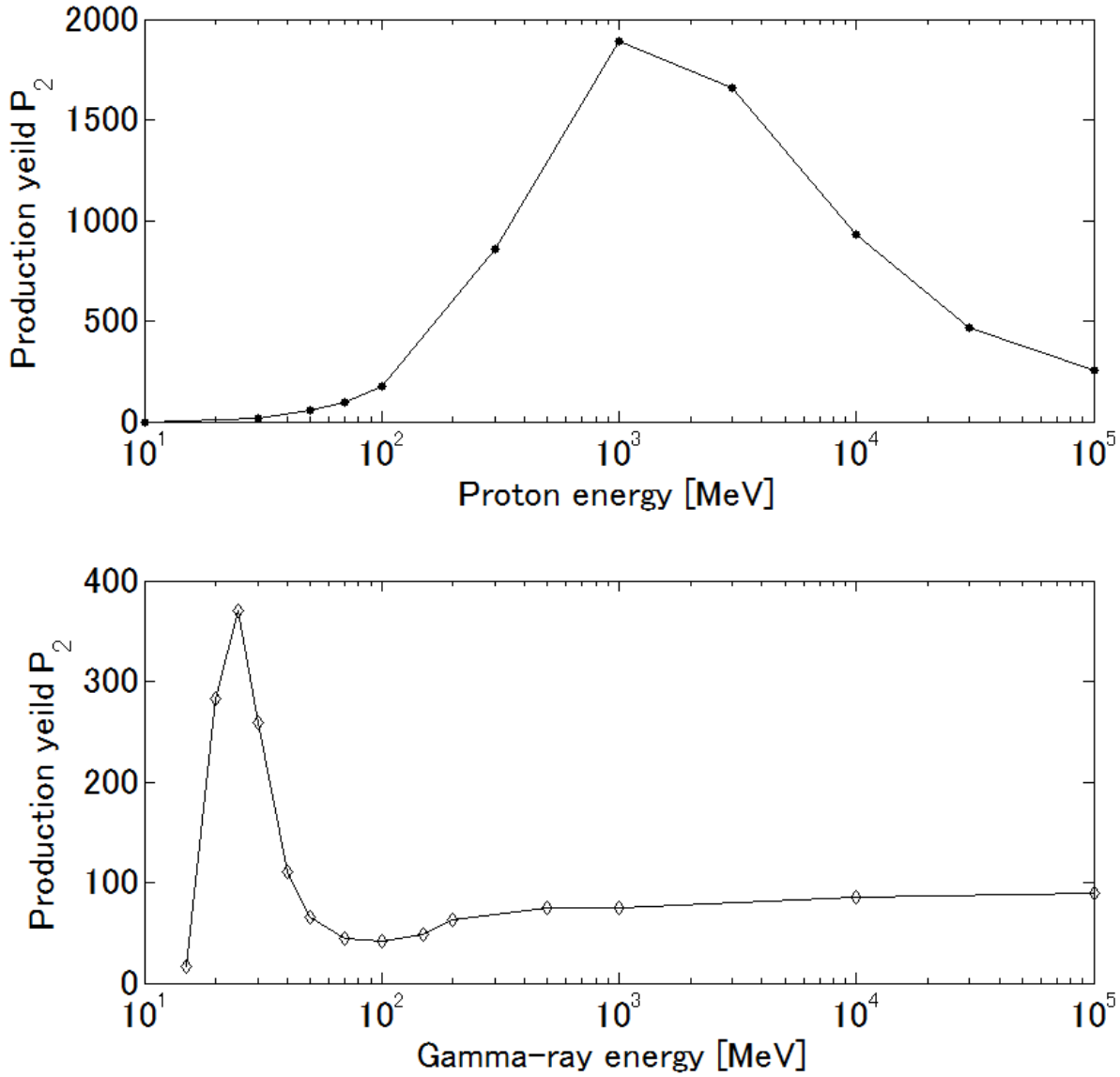

Figure 7-13: The energy distribution of ^{14}C production yield (P_2 [atoms/erg]). A kind of incident particle is proton in upper panel, and is gamma ray in lower panel.

7-4 Origin of the AD 775 event

The increment of ^{14}C content in AD 775 was about 12‰. The source cannot be the solar cycle (i.e., the Schwabe cycle), which on average has an 11-year period and an amplitude of 1.5‰ with respect to its effect on the atmospheric ^{14}C concentration. Compared with the Schwabe cycle, an increase of 12‰ in 1 year is about 20 times larger.

If a magnetic field of the earth magnetosphere largely decreases, the incoming cosmic ray intensity increases largely. Figure 7-14(b) shows differences in ^{14}C production rate by the strength of the geomagnetism. If the geomagnetism becomes 1/10 of the present, the ^{14}C production rate becomes 2-3 times larger. Then it is possible to explain the 775 event by very low level geomagnetism. However, such a decreasing in field intensity (=geomagnetic excursion) usually occurs with the time order of several thousand years. Therefore, it is hard to consider short-term excursion (< 2 years) as a cause of the 775 event. Only two known phenomena are possibly to change the cosmic-ray intensity within 2 years: they are a supernova (SN) explosion and a large solar proton event (SPE).

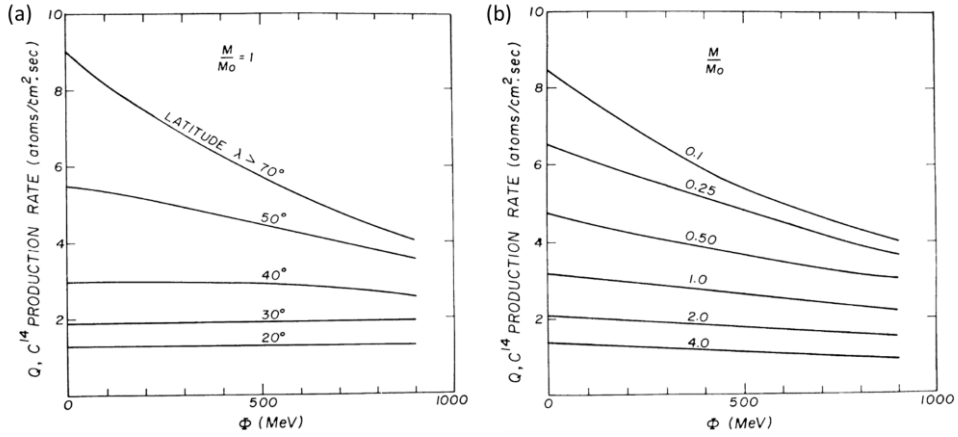

Figure 7-14: (a) ^{14}C production rate for the modulation parameter in case the current geomagnetism (λ : latitude of the earth, Mo: current geomagnetic intensity). (b) Globally averaged ^{14}C production rate for the modulation parameter (M/Mo = 0.1, 0.25, 0.5, 1,2,4). This graph is cited from *Castagnoli* [1980].

7-4-1 Supernova origin

First we consider the increase of ^{14}C content due to a supernova explosion. In this case, gamma rays can produce ^{14}C because gamma-rays are unaffected by the galactic magnetic field, unlike other particles from SN explosions. The production mechanism is the reaction $^{14}N(n,p)\,^{14}C$ from secondary neutrons of 10-40 MeV produced in the cascade by hard gamma-rays in the atmosphere. No detectable increase in the ^{14}C content corresponding to SN1006, SN1054, SN1572 and SN1604, which had brightness that we can see even during daytime, have been measured. Since we detected the AD 775 event by ^{14}C, its apparent magnitude must be brighter and the energy of the AD 775 event at the Earth must be larger than them (chapter 2-2).

We assume that the differential energy spectrum of gamma-ray emission from a supernova is described by a power law with an index of -2.5 ($=E^{-2.5}$). By integrating over gamma-ray energies above 10 MeV, we obtain a ^{14}C production yield P_3 [^{14}C atoms/erg] as:

$$P_3(gamma) = \int_{10MeV}^{1000MeV} P_2(E) \cdot E \cdot E^{-2.5} dE \Big/ \int_{10MeV}^{1000MeV} E \cdot E^{-2.5} dE = 1.2 \times 10^2 \ [^{14}C \ atoms/erg]$$

The simulation of energy interval of P_1 is large (see table 7-3), we applied a linear interporation with a logarithm (10, 20, 30,…100, 200,…MeV) when integrated over gamma-ray energies. Our result of 1.2×10^2 [atoms/erg] is almost same as the result of 1.3×10^2 [atoms/erg] in the estimation by *Menjo et al.* [2006].

Based on this figure, if we use the production rate of our carbon cycle model ($=1.5 \times 10^8$ atoms/cm^2), the incident gamma-ray energy necessary for this increase of ^{14}C content in the atmosphere is about 6×10^{24} erg. If the distance of the supernova were the same as that of SN1006 (2 kpc), the total gamma-ray energy would be 3×10^{51} erg. This energy release is 100 times larger than the gamma-ray energy release from a normal supernova assuming that 1% of total supernova energy goes to gamma-rays and that emission of energy is isotropic (typical total supernova energy is of the order of 10^{51} erg). Therefore, the supernova should be closer than 2 kpc, so that the total gamma-ray energy release is 3×10^{51} erg, which is a typical supernova energy.

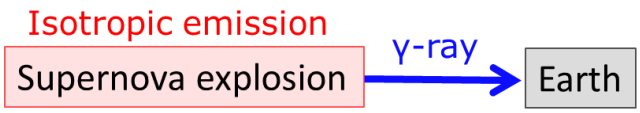

Figure 7-15: Schematic of super nova explosion to th Earth.

Although there are no historical records of a supernova visible in the Northern Hemisphere around AD 775 (European and Chinese SN records [*Stephenson & Clark* 1976], comet lists [*Parkenier et al.* 2008], and auroral reports [*Dall'Olmo* 1979]), there could be historically unrecorded supernova remnants: for example, Cassiopeia A, which was found by radio observations and estimated to have occurred ~300 years ago, or Vela Jr (RX J0852.024622), which was found by the COMPTEL gamma-ray observatory, based on the ^{44}Ti line; the distance to Vela Jr is hundreds of parsecs and its age is 10^3–10^4 years [*Iyudin et al.* 1998; *Katsuda et al.* 2009; *Telezhinsky* 2009]. Furthermore, the remaining historical documentation from 8th century is poor. Therefore, we cannot rule out an undiscovered supernova remnant corresponding to the AD 775 event from above reason.

However, looking at a catalogues of nearby SNR searched by X-ray and radio (catalog by *Green* [2009] and Chandra X-ray [18, 9]), there is no remnants corresponding to SN775. Therefore a supernova in AD 775 may be not probable, because a supernova that occurred relatively recently and

relatively near Earth should still be tremendously bright (in radio, X-rays and ^{44}Ti), and such an object is not observed.

7-4-2 Large SPE origin

Next we consider the case of an SPE. We assume that the rigidity spectrum of proton emission from an SPE can be expressed by exponential: exp(－R/R_0), where R is the rigidity of protons and R_0 is the characteristic rigidity of the SPE. R_0 is set to 78 MV [*Usoskin et al.* 2006] in the following calculation. By integrating over proton energies above 100 MeV (we applied a linear interporation with a logarithm: 100, 200,…1000, 2000,…MeV), we obtain a ^{14}C production yield P_3 [^{14}C atoms/erg] as:

$$P_3(proton) = \int_{100MeV}^{100000MeV} P_2(E)\cdot E\cdot e^{-\frac{R}{R0}}dE \Big/ \int_{100MeV}^{100000MeV} E\cdot e^{-\frac{R}{R0}}dE = 3.8\times 10^2\ [^{14}Catoms/erg]$$

Unlike gamma rays, protons reaching the Earth are blocked by the geomagnetic field. We applied predicted vertical geomagnetic cut-off rigidities on the Earth using EXPACS software [Sato et al. 2008] for an assumed geomagnetic field the same as the present field. Figure 7-16 shows the vertical cutoff rigidities of every latitude and longitude by EXPACS result. We calculated the flux at intervals of 10° in latitude (we used the value that averaged longitude as a representative one of each latitude), and obtained an average ^{14}C production yield P_3'(proton) = 10 [^{14}C atoms / erg]. The total proton energy necessary for this event was estimated to be 8×10^{25} erg at the Earth, which corresponds to 2×10^{35} erg at the Sun in case that SPE particles are isotropically emitted. This energy may be compared to the total proton energy of 10^{29}–10^{32} erg in a normal SPE. However, the real flare particles are not emitted isotropically (I will describe below). So the energy of 2×10^{35} erg is an upper limit of this event. Additionally, real solar energetic particles (SEPs) come along the magnetic field between the sun and the earth. And we should consider the flare position in the sun to make more accurate estimate of the scale of the event.

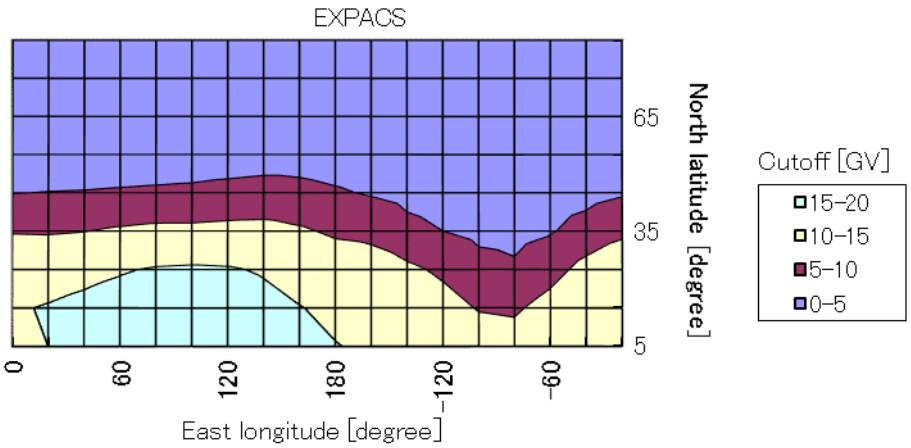

Figure 7-16: Result of the vertical geomagnetic cut-off rigidities using EXPACS software [*Sato et al.* 2008].

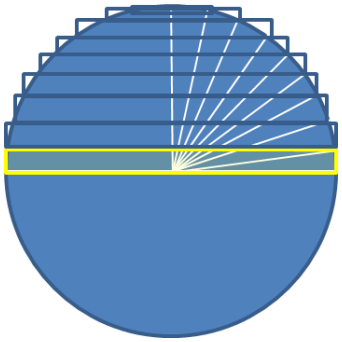

Figure 7-17: Image of intervals of 10˚ in latitude. We calculated by weighting each area which is shown as the box.

After our paper about the AD 775 event was published, there are some attempts to specify the cause of the AD 775 event. *Melott and Thomas* [2012] have reexamined the flare energy of the AD 775 event by assuming a directional flare with opening angle of 24˚, and concluded that implied energy of SPE is reduced to $\sim 10^{33}$ erg. This is about 1/100 energy of our calculation, which presumes that flare particles propagated isotropically. According to their simulation of ozone layer depletion by SEPs (Solar Energetic Particles), the energetic level does not have a serious effect on living matter on the earth (figure7-18). They concluded that SPE appears to be possible cause of the AD 775 event.

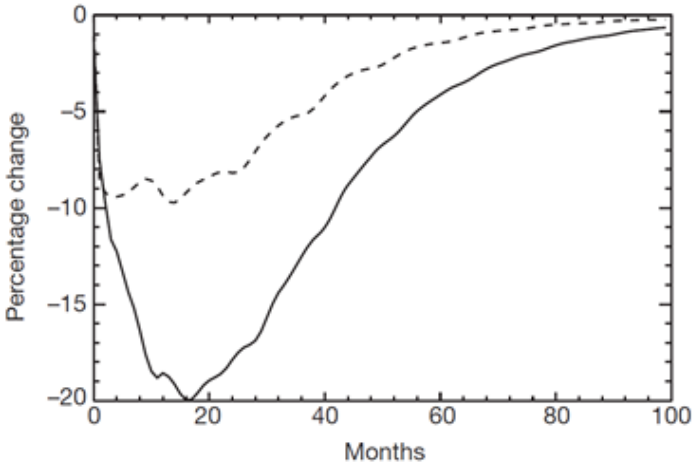

Figure 7-18: Percentage change in globally averaged ozone density. The dashed line represents the origin of the 775 event is short gamma-ray burst case and the solid line represents SPE case. This graph is cited from *Melott & Thomas* [2012].

Other studies also estimated a scale of the 775 event [*Melott and Thomas* 2012; *Usoskin et al.* 2012, 2013; *Thomas et al.* 2013]. Although there are some estimation due to like the energy spectrum of SPE, we can say that this event is at least more than ten times larger than the largest Carrington flare in AD 1859 because the ^{14}C content does not show any increase around the Carrington event (in a case that an ^{14}C increment of the Carrington event is same order as the measurement error). I have to mention that the 775 event can be explained not only by such a large SPE, but also by some smaller SPEs which intermittently-occurred over 1-2 years.

Usoskin et al. [2013] reported some historical records which support higher auroral activities in the 770s. The records are red-cross in the sky (Angro saxon chronicle, England, AD 774 or 776?) [*Allen* 2012], two inflamed shields in the sky (Germany, AD 776) [*Gibbons & Werner* 2012], and some auroral records in China (AD 770 (twice), AD773 and AD775) [*Keimatsu* 1973; *Yau et al.* 1995]. If a large SPE occur, global aurora would be observed. For example, aurorae were observed around the world (even the Caribbean) in the Carrington flare. Therefore, these records can show the higher solar activity in the 770s and may be a proof of the SPE origin.

Eichler et al. [2013] also supported a large SPE origin, but they tried to explain that a super-flare occurrs by a cometary encounters with the sun.

7-4-3 Short gamma-ray burst origin

For gamma-ray events, supernova explosions and gamma-ray bursts (GRBs) can be considered. The supernova remnants corresponding to AD 775 has not been detected and historical documentation has not been found (chapter 7-4-1), so a supernova origin is quite unlikely. Although we considered only the normal supernova origin in the litelature [*Miyake et al.* 2012], *Hambaryan & Neuhauser* [2013] claimed that a short gamma-ray burst (<2s) can explain the AD 775 event.

Gamma-ray burst is the extremely energetic event in the galaxy, and is clasified into two types, a long gamma-ray burst and a short gamma-ray burst. The difference between these two kinds of GRBs is the duration of gamma-ray emission (long GRB: > 2 seconds, short GRB: < 2 seconds) and the energy spectrum of gamma-rays (long GRB: soft spectrum, short GRB: hard spectrum). This is known by the observation of GRBs (figure 7-19). The origin of short and long GRB are considered as a merger of binary of neutron stars (or black hole) and a core-collapse large supernova, respectively. Figure 7-20 represents the most favoured model of the formation of short GRBs.

In case of a short GRB, its spectral hardness is consistent with the differential production rates of ^{14}C and ^{10}Be, and the absence of historical records of a supernova or a supernova remnant is consistent with a short GRB, they claimed.

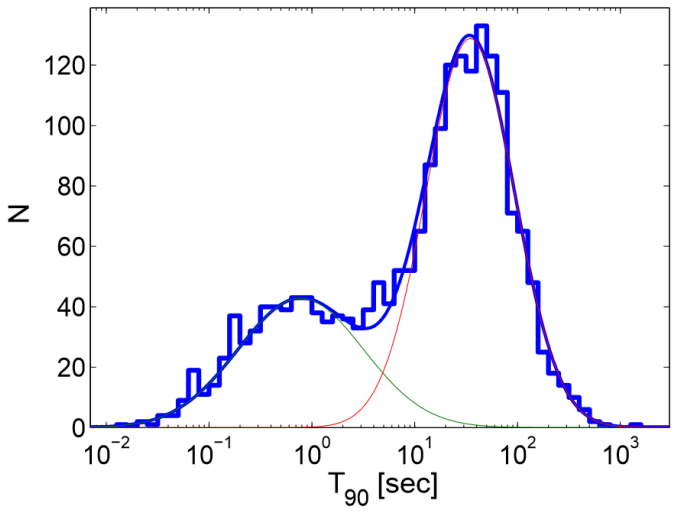

Figure 7-19: T_{90} distribution (T_{90} is duration encompassing the 5-95 percentiles of the total counts in the energy range 20-2000 keV) of the entire BATSE GRBs. The distribution divides into two groups in 2 sec. This graph is cited from *Nakar* [2008].

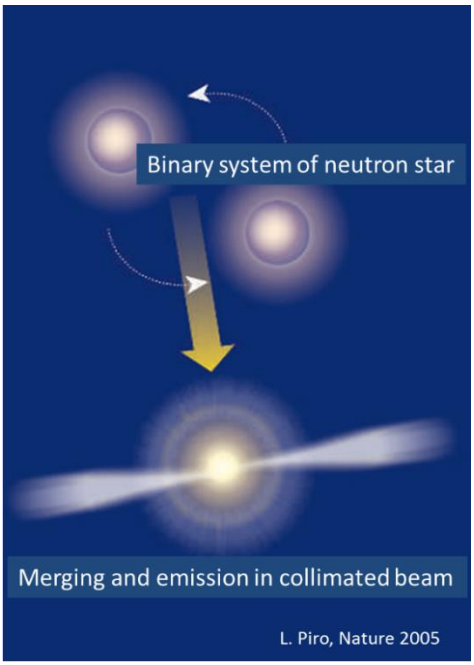

Figure 7-20: The model of the formation of short gamma-ray bursts. This graph is cited from *Piro* [2005].

Chapter 8

Discussions ~AD 994 event~

8-1 Expansion of the measurement period

Although the cause of the AD 775 event can be explained by a large SPE [*Mellot & Thomas* 2012; *Usoskin et al.* 2012, 2013; *Eichler* 2013] or a short GRB [*Hambarian & Neuhauser* 2013], a more detailed discussion of the cause is difficult because the rate of occurrence of such rapid ^{14}C events remains unknown. We need to know whether more events similar to the AD 775 event exist in the past ^{14}C record. Although the ^{14}C increment around AD 775 is the largest class in the last three millennia from the IntCal09 data [*Reimer et al.* 2009], there are a large number of period when the ^{14}C content has not been measured with 1-year resolution. Therefore, it is possible that smaller increases than the AD 775 event are hidden in these unmeasured periods. We needed to measure yearly ^{14}C content of expanded periods.

When we chose the expanded measurement periods, we had the purpose of not only searching for other rapid events like the AD 775 event, but also investigating the Schwabe cycle length of our Sun during the 7th century grand solar Minimum (AD 650-720). Although I will not describe the details of the 7th century Minimum in this thesis, it has been detected that the Schwabe cycle length durig this Minimum becomes longer by appling periodic analyses on our ^{14}C data. Please see *Miyake et al.* [2013b] about the discussion of the Schwabe cycle in detail.

8-2 The AD 994 event

After the finding of the AD 775 event, we have measured the ^{14}C content in Yaku-A during extended periods from AD 550 to 760 and from AD 822 to 1,100 to search other ^{14}C increase events. As a result, we found another rapid ^{14}C increase from AD 993 to 994. Although the age of second ^{14}C event is described from AD 992 to AD 993 in *Miyake et al.* [2013a], it turns out that the age determination mistake was found (that is, two rings of AD946-947 had been recognized as one annual ring including a false ring. [*Miyake et al.* 2013c]). Then, the second event should have occurred from AD 993 to 994.

The increment from AD 993 to 994 is 9.1 ‰, which corresponds to 5.1 sigma against the measurement errors. A comparison of the AD 775 and the AD 994 events is shown in figure 8-1. The shapes of the two series are very similar, that is, a rapid ^{14}C increase within 1 year followed by a decay owing to the carbon cycle. The scale of the AD 994 event is 0.6 times as large as the AD 775 event.

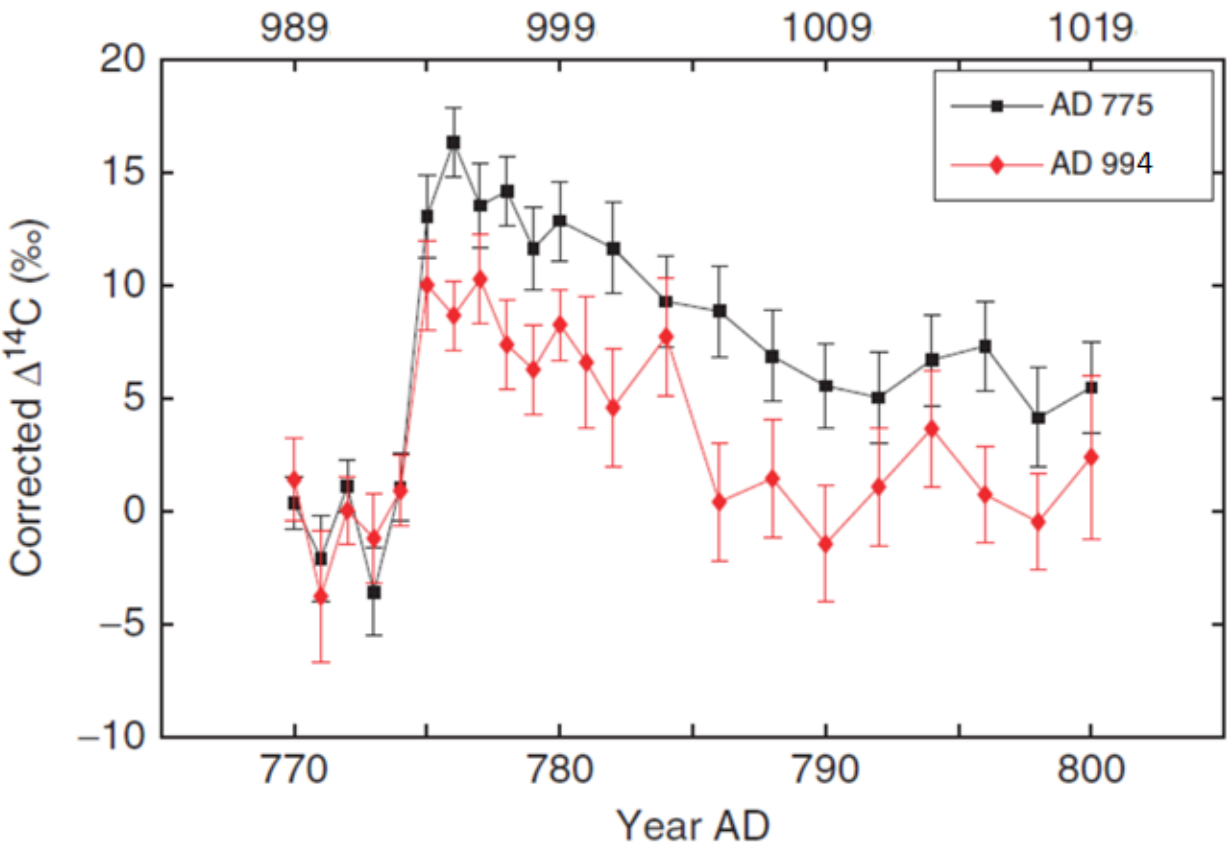

Figure 8-1: Comparison of the AD 775 and the AD 994 peaks. Squares show the AD 775 series from AD 770–800, and diamonds show the AD 994 series from AD 989–1019. The zero level of the vertical axes is shifted to be the weighted mean value of AD 770–774 for the AD 775 series and AD 989–993 for the AD 994 series.

8-2-1 Comparison with IntCal dataset

Although the quasi-decadal IntCal09 data set shows a small ^{14}C enhancement around AD 994 (3 permil increase from AD 980 to 995), this increase is hardly distinguishable from many other variations. Therefore, this implies that small increases like the AD 994 event will not be detected until after 1-year resolution measurements.

8-2-2 Comparison with ^{10}Be data

Another cosmogenic nuclide, ^{10}Be, in the Antarctic Dome Fuji ice core also shows increases in the flux corresponding to around AD 775 and AD 994 [*Horiuchi et al.* 2008]. Figure 8-2 shows ^{10}Be flux data for AD 700-1100. The ages of the ^{10}Be data are determined by matching the production rate pattern of ^{10}Be with the ^{14}C production [*Horiuchi et al.* 2008]. The increasing rates are 7.2×10^3 [atoms cm^{-2} yr^{-1} /yr] from AD 770 to 785, and 6.2×10^3 [atoms cm^{-2} yr^{-1} /yr] from AD 985 to 995. The scale of the increase around AD 994 is 0.86 times as large as that around AD 775. This value is consistent with the ratio for ^{14}C events (=0.6 times larger) because ^{10}Be data have a lower time resolution (~10 years resolution) than that of ^{14}C data. If the causes of two events are different, the difference between the ratios of ^{14}C and ^{10}Be production rates is expected. This difference is caused by energy spectrums or particle species of the origin events. From the consistency of increasing ratio of AD 775 and AD 994 between ^{14}C and ^{10}Be, the cause of two events must be same.

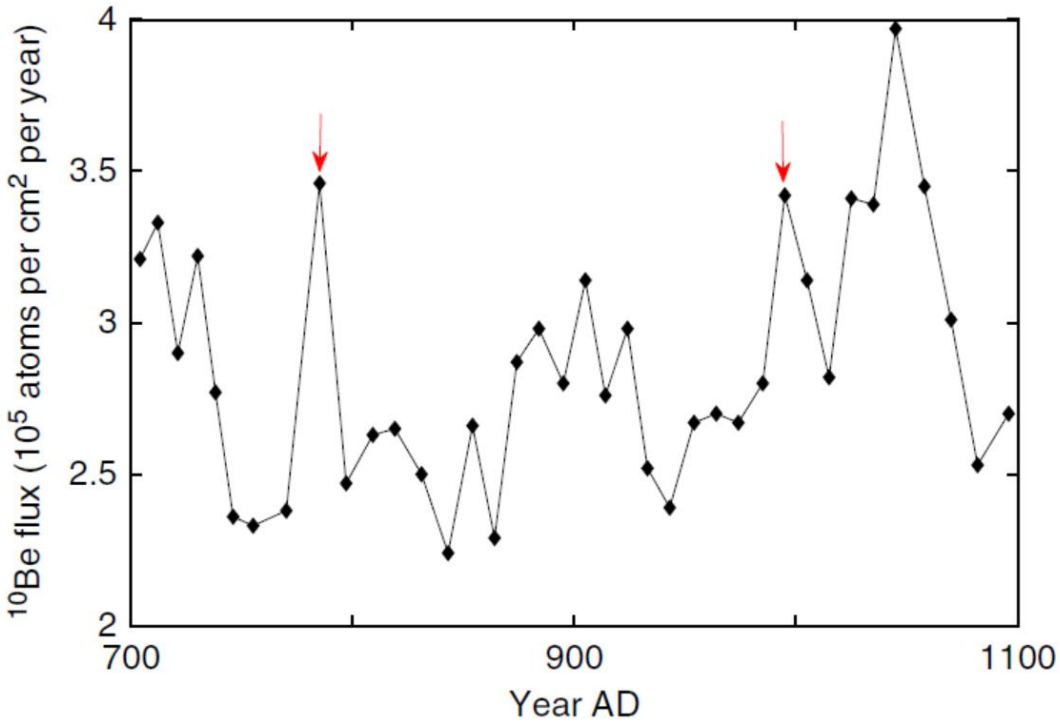

Figure 8-2: ^{10}Be data from ice core of Dome Fuji in Antarctica. The vertical axis represents the ^{10}Be flux, which is calculated from the snow accumuration rate, estimated by the three-point (1.5 m: B30 years) averaged δ^{18}O [*Horiuchi et al.* 2008]. The horizontal axis represents the calendar year. Each point is corrected by a ^{10}Be–^{14}C correlation age model. The two arrows show the ages of AD 785 and AD 995. The ^{10}Be flux increments of the two data is 1.08×10^5 (atoms per cm^2 per year) from AD 770 to 785 and is 0.72×10^5 (atoms per cm^2 per year) from AD 985 to 995. The large increase from AD 1010~1040 is caused by the solar magnetic activity (Oort grand solar minimum).

8-2-3 Iida Hinoki tree

The AD 775 event was confirmed by some different trees, but the AD 994 event was detected by only one Japanese cedar tree. So it is better to confirm this result more reliable by measuring ^{14}C content in another tree sample. Hinoki cypress tree sample (*Japanese cypress*, from Iida city, Nagano prefecture, figure 8-3) was supplied by T. Mitsutani from National Research Institute for Cultural Properties. Then we measured the ^{14}C content in this sample from AD 988 to 997 with one year resolution. We produced the cellulose from the wood samples in Nagoya University, and the following sample preparation processes, i.e. the purification, the graphitization, and the AMS measurement, were conducted in Yamagata University.

New measurements using a Japanese cypress tree also shows a significant increase from AD 993 to AD 994, a result of which is shown in figure 8-4. Then, it is considered that the second event would more likely occur in AD 993 to AD 994 [*Miyake et al.* 2013c].

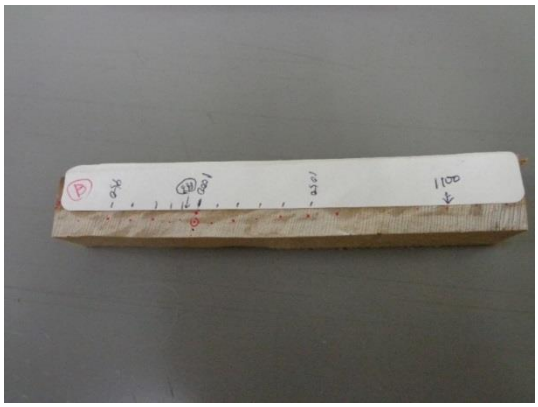

Figure 8-3: Picture of the Hinoki cypress sample. The age determination of this sample was done by T. Mitsutani using the dendro chronology.

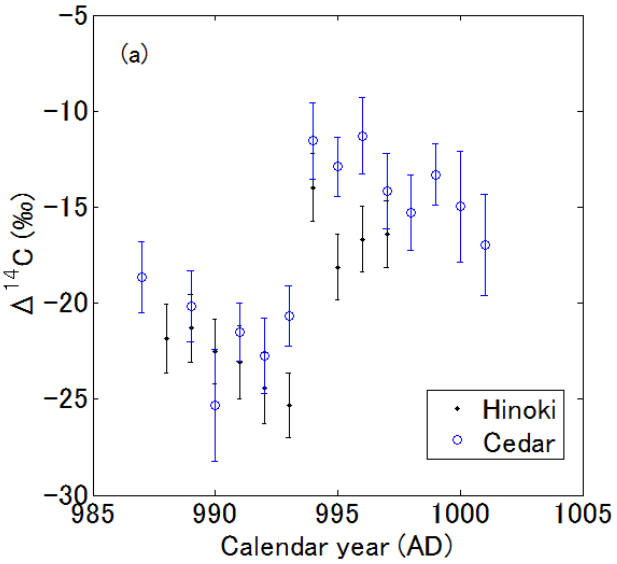

Figure 8-4: The Comparison between our new result (Hinoki cypress, Miyake et al. 2013c) and our old result (Yaku cedar, *Miyake et al.* 2013a) from AD 987 to AD 1001. The increment of the Hinoki sereis from AD 993 to 994 is 11.3‰ (5.5σ against the mean errors of AD 993 and AD 994). The dots show our new data using Hinoki cypress tree-rings, the open circles show our old data using thee Yaku-cedar tree-rings.

8-3 Cause of ^{14}C rapid events

Although *Hambaryan & Neuhäuser* [2013] claim that the observed rate of short GRBs (one event in 3.75×10^6 years) and that of ^{14}C events (one ^{14}C event in 3000 years) are consistent within 2.6σ, the finding of the 2nd ^{14}C event makes a ^{14}C event rate large and the consistency between the observed rate of short GRBs and the ^{14}C event rate becomes worse (the probability of a short GRB rate with one ^{14}C event in 1500 years is 0.04%). Adding to this, it is possible that the ^{14}C event rate is larger because there are many periods without a one year resolution measurement of ^{14}C content in the 3000 year period.

The actual ^{14}C event rate should be 1/800yrs (detected event / measured period with 1-2 yr resolution), and the probability is 0.02%. *Melott and Thomas* [2012] also discuss the event rate of short GRB (a probablility of order 10^{-4} over 1250 years), however, their rate is lower than that of Hambaryan and Neuhauser. Then, the short GRB is less likely to be the cause. In addition, *Hambaryan and Neuhäuser* [2013] claim that it is possible that more short GRBs exist than those observed, which would explain the inconsistency in the event rate between the obsereved short GRB rate and the ^{14}C event rate; however, additional studies are necessary to confirm this claim.

Next, we consider the SPE origin. An emergence of SPE is considered to be closely bound to solar activity such as solar flares and CMEs. To know the solar activity during the 8-10th centuries, we have examined the IntCal dataset [*Reimer et al.* 2009]. The period from the late 13th century to the early 19th century is known as 'little ice age', which includes the Wolf, Spörer, Maunder, and Dalton solar minima (figure 3-2). On the other hand, the 8-10th centuries have no grand solar minimum. There have been some attempts to reconstruct the solar activity by using ^{14}C dataset [*Solanki et al.* 2004; *Usoskin et al.* 2006b], and they showed higher solar activity level during the 8-10th centuries than that during the 13-19th centuries, on average. This fact may explain why the 8-10th centuries has two rapid increases of ^{14}C content and after the 11th century there were no such events.

Based on a reassessment of an energy spectrum of SPE, production calculations of ^{14}C and ^{10}Be, and a deposition model, *Usoskin et al.* [2012, 2013] claimed that the AD 775 event can be explained by an extreme SPE that was about 50 times larger than the largest SPE in AD 1956. From this aspect, the AD 994 event is about 30 times larger than SPE1956. Also, according to *Usoskin et al.* [2012], the occurrence rate of the SPE775 event is 10^{-4} per year and that of the SPE994 event is 10^{-3} per years. It is possible that these events occur within 200 years assuming that SPEs are mutually independent. Although they claimed that there is no apparent relation between the occurrence of SPE and the solar activity level, or it is proposed that large SPEs occur more likely during grand solar minima [*Barnard & Lockwood* 2011; *Barnard et al.* 2011; *Owens et al.* 2011], we doubt these claims because the two events occurred in the non-solar minimum period.

Considering the ^{14}C event rate and higher solar activity in the 8-10th centuries, a solar origin is a plausible cause of ^{14}C increase events.

8-4 Prospects for the future

Detection of the second ^{14}C event indicates the possibility that a lot of smaller ^{14}C increase events are hidden in the periods when the ^{14}C content has not been measured with one-year resolution.

Indeed, there are some smaller gaps (not only increases but also decreases) in yearly measured period (for example, AD 630, 638, 820, 1005, and so on). They are not enough significance against the errors, however, it is possible that they are smaller ^{14}C events. Figure 8-5 shows the flare frequency against the energy. It shows that the higher a flare energy is, the smaller the flare frequency becomes with the power-law. If the cause of the ^{14}C events are large SPEs and the frequency of the large SPEs obeys to this frequency of lower energy range, a lot of smaller ^{14}C events than the AD 775 event must exist.

Then, we are going to reduce the measurement errors for these small events by multiple ^{14}C measurements, and for detection of more such events.

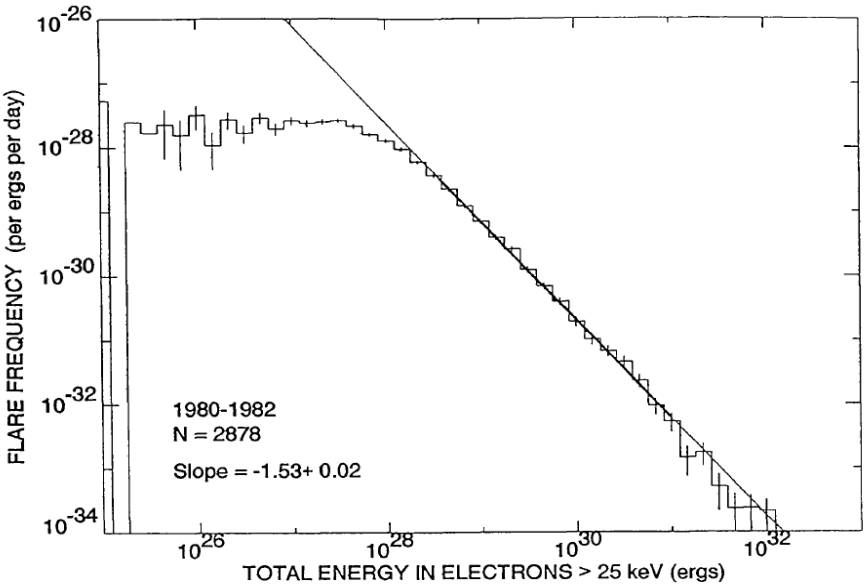

Figure 8-5: Solar flare frequency of electrons. [*Crosby et al.*1993].

It will also be necessary to conduct investigations of ^{14}C records during additional unmeasured periods with a one year resolution to search for other ^{14}C events. Figure 8-6 shows the IntCal09 data for the last 12,000 years, however, more than 10,000 years period have not measured with one-year resolution. During this period, there are some terms when ^{14}C content increased rapidly of a magnitude of more than 3.5‰/10years, which are indicated by the arrows in figure 8-6. Espeially, the ^{14}C content around BC 5500 (thick arrow) has a large increase rate (=5.4‰/10years). Then, it is possible that these increases are cosmic-ray events. As well as such a large ^{14}C increase, we need to detect the small event such as the AD 994 event. Therefore, we are going to measure ^{14}C content for this 10,000 years with one-year resolution, complete the data, and investigate when such ^{14}C events occurred. We expect that the occurrence rate of large SPEs will become apparent from our future measurements.

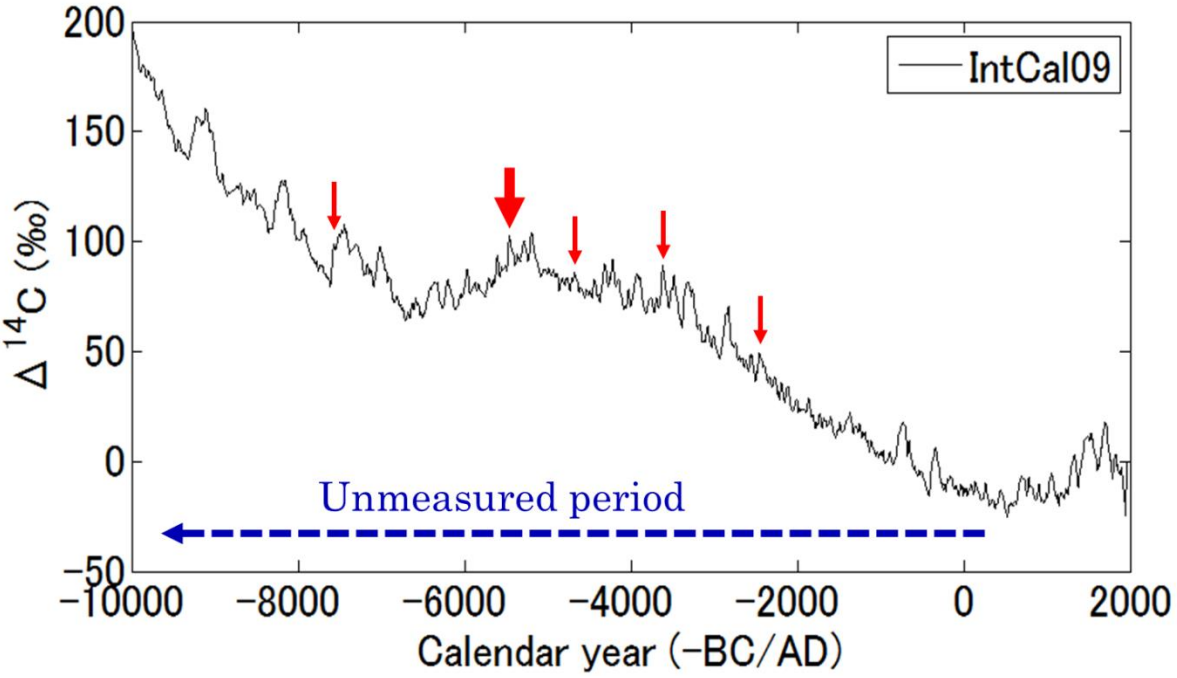

Figure 8-6: IntCal09 data for the last 12,000 years. The arrows show the period when the ^{14}C content largely increased by a magnitude of more than 3.5‰/10years. The thick arrow indicates the largest ^{14}C increase during this 12,000 years.

Chapter 9

Conclusion

We have measured the ^{14}C content in some Japanese tree-rings from AD 550 to AD 1100, and have found two rapid increases in AD 775 and AD 994. The AD 775 event is the first clear detection of an increase in ^{14}C content on time scales of one year. Only two ^{14}C events (AD 775 and AD 994) have been found at the moment. The immediate and subsequent variation in ^{14}C content can be explained by a short-term increase in the ^{14}C production rate followed by a decrease over several years due to the global carbon cycle. These events were also detected by other ^{14}C measurements, such as the decadal IntCal dataset based on North American and European trees, and the yearly data from German and New Zealander trees.

There are sharp ^{10}Be increases in the Antarctic Dome Fuji ice core corresponding to these two events. Since the increase ratio of $^{10}Be/^{14}C$ between two events are consistent with each other, the cause of the detected events must be same. The ^{14}C event rate is estimated to be 1 event per 800 years based on the yearly ^{14}C measurements. Considering the ^{14}C event rate and higher solar activity in the 8-10th centuries, a large solar proton event (SPE) is a more plausible cause of these ^{14}C increase events. The scale of the 775 event can be estimated as more than 10 times larger than the Carrigton flare. This indicates the possibility that such large SPEs will occur in the future.

Detection of the second ^{14}C event means the possibility that a lot of smaller ^{14}C increases are hidden in the periods when the ^{14}C content has not been measured with a 1-year resolution. In the future, it will be necessary to conduct investigations of ^{14}C records during additional unmeasured periods with a 1-year resolution. In parallel to the long-time scale ^{14}C yearly measurement, we should investigate other cosmogenic nuclides in some ice cores to specify the cause of these rapid events.

Appendix

Continuous ^{14}C dataset

The measurement period is AD 550-1101 and this long continuous dataset with 1 or 2 year resolution is comparable to Stuiver's representative yearly dataset from AD 1510-1954 [*Stuiver et al.* 1998b]. Continuous ^{14}C datasets are very useful for not only investigating the past cosmic ray intensity or the solar activity but also for a wide-ranging field such as the geological field or the archaeometry (especially, it is possible that we can determine the absolute date if there is a rapid ^{14}C increase like the AD 775 event). I'm going to publish the ^{14}C data list elsewhere. In this section, I'd like to show the figure of our all ^{14}C data.

A-1 All measurement results

Figure A1 shows the $\Delta^{14}C$ results of my all measurement runs. Add to my results, the Menjo series, the Kuwana series, and the IntCal09 are shown in these figures. Figure A2(a) shows the consolidated $\Delta^{14}C$ data with measurement errors of some series for the period of AD 550 to 1101, and the figure A2(b) shows the magnitude of the errors in figure A2(a).

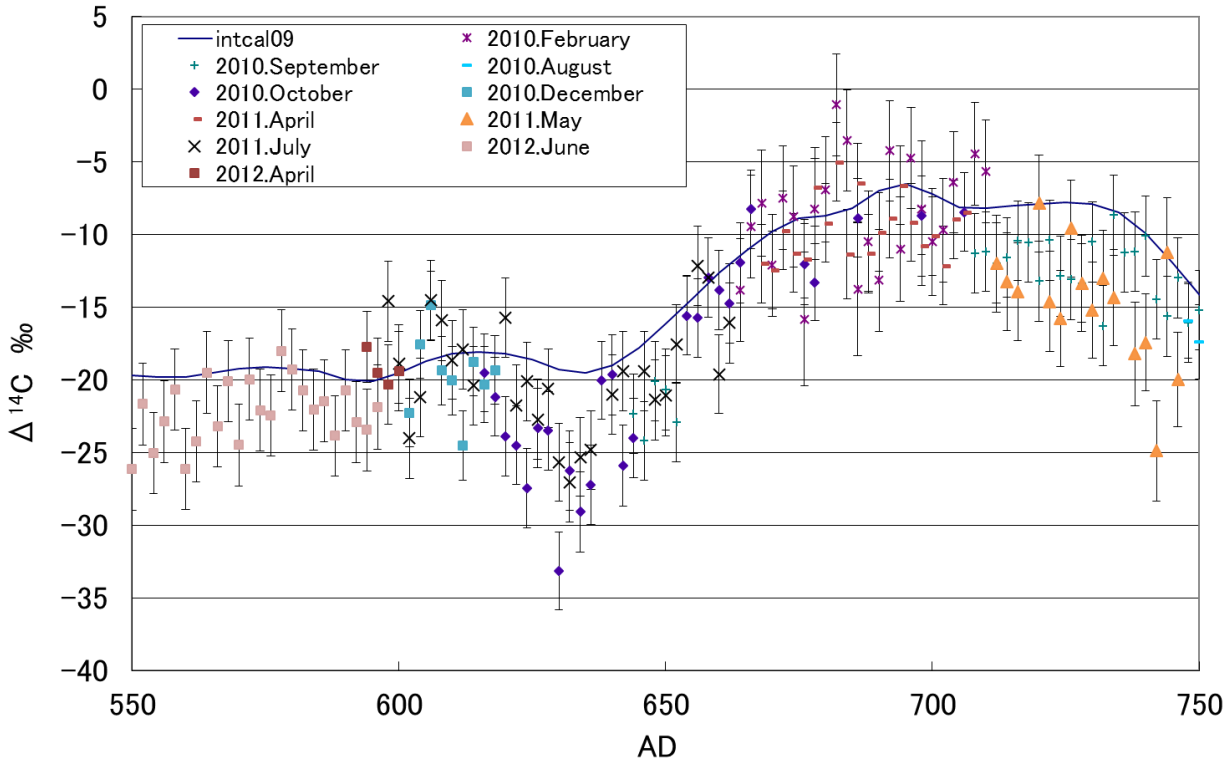

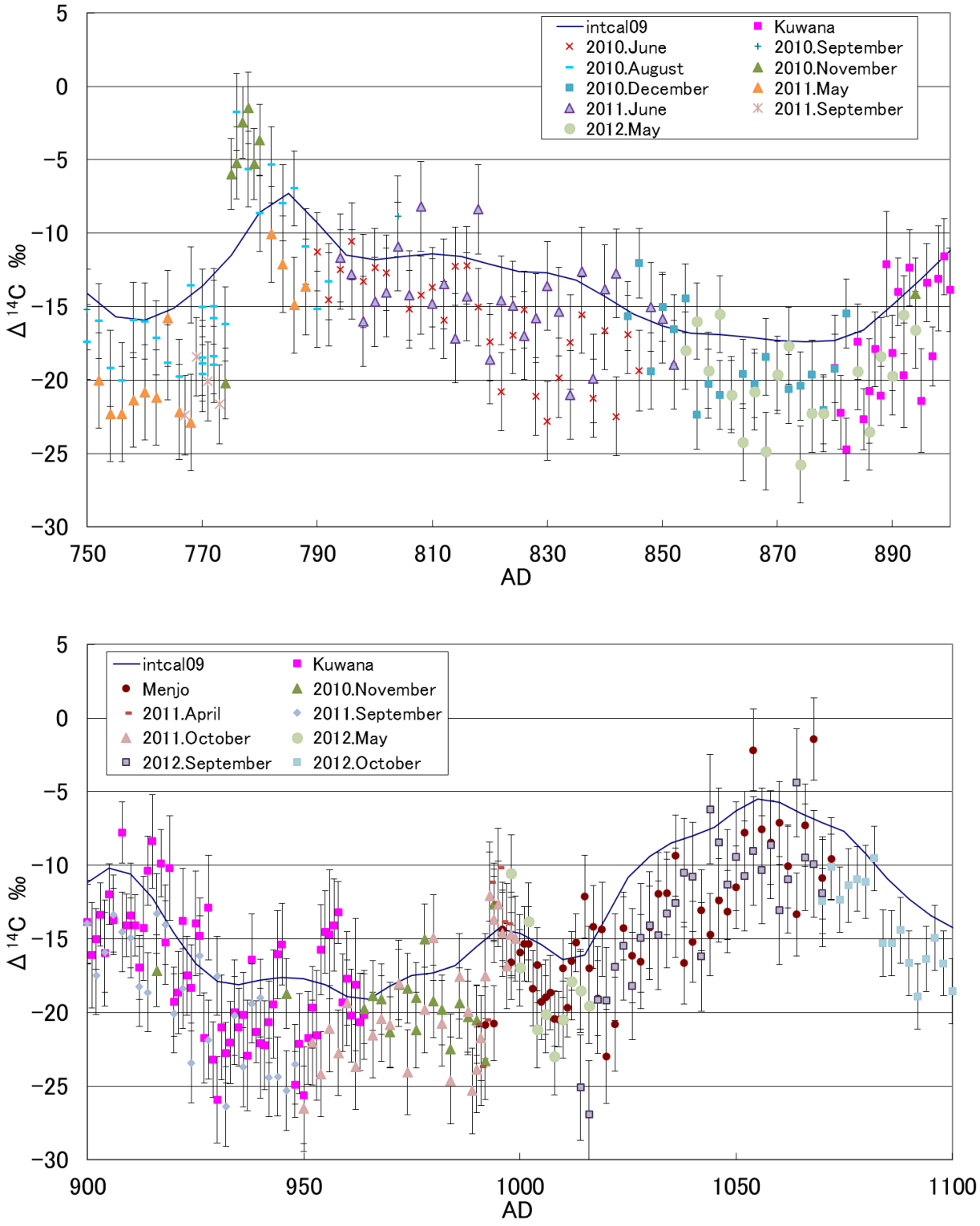

Figure A1: Our all ^{14}C measurement results from AD 550-1101. Each kind of marks indicates each measurement run. Add to our measurements, the data of the Menjo series [*Menjo et al.* 2006] and the Kuwana series [*Miyahara et al.* 2008] are plotted in these graphs. The blue line shows the IntCal09 data [*Reimer et al.* 2009].

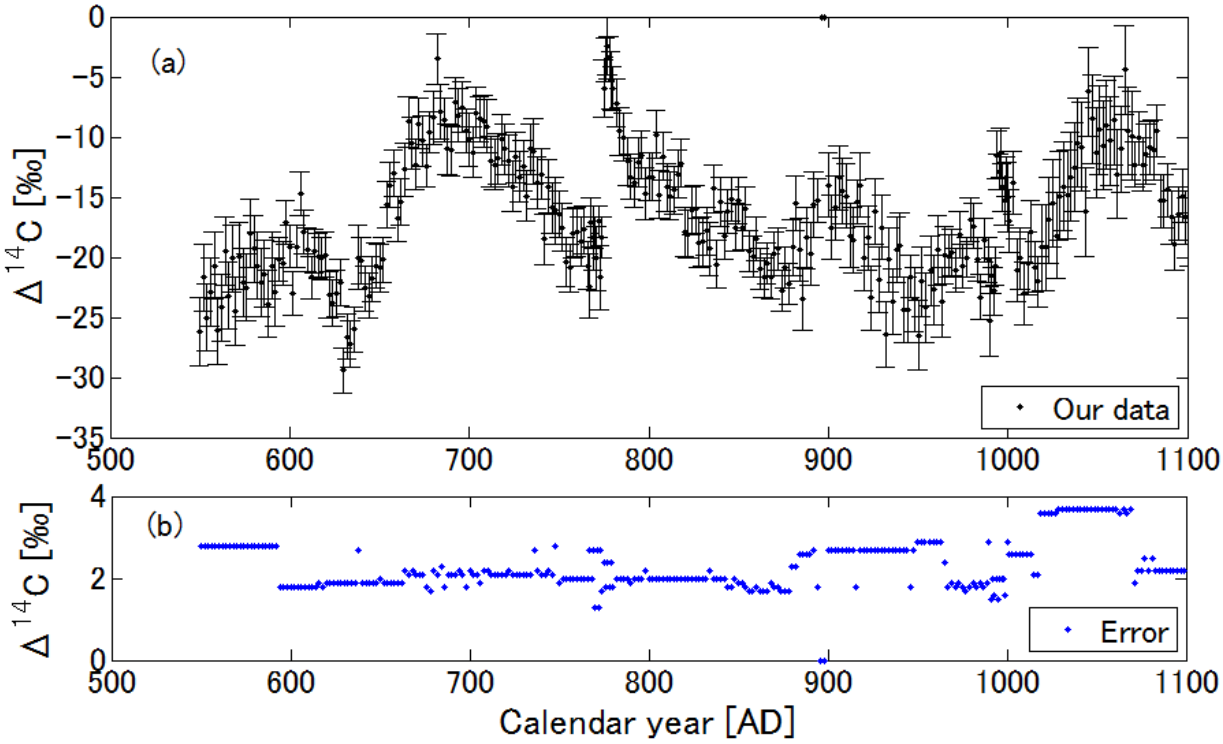

Figure A2: Consolidated $\Delta^{14}C$ data (Miyake series) and its measurement errors. (a) $\Delta^{14}C$ data from AD 550-1101. (b) A series of the consolidated measurement errors.

A-2 Comparison with the IntCal data

In order to compare our results (obtained from Japanese trees) with IntCal98 (obtained from North American and European trees) [*Stuiver et al.* 1998a], we averaged the yearly data to obtain a series with a decadal time resolution. The comparison of our data and the decadal IntCal98 data is shown in figure A3, and the result of decadal average of our data and IntCal98 from AD 555 to 1095 is shown in Figure A4.

The two series show similar variations to each other, however, our results are 2.2 ‰ smaller than IntCal98 on average (this is 8.4σ significance level). This is considered as a regional effect. Because Yaku-Island, where our sample trees had lived, is located in southern Japan, it is considered that atmosphere in Yaku-Island is affected by marine low ^{14}C level gas [*Nakamura et al.* 2013]. It is known that the ^{14}C content in the Southern Hemisphere is lower than the Northern Hemisphere due to the area of sea. The IntCal age calibration curve is used for the Northern Hemisphere, whereas SHCal caliblation curve is used for the Southern Hemisphere. Figure A5 shows the comparison between ^{14}C

ages[11] of our data (Yaku-Island), the IntCal09 dataset [*Reimer et al.* 2009], and the SHCal04 dataset [*McCormac et al.* 2004]. The ^{14}C content of our result locates between the IntCal09 and the SHCal04, and this supports the hypothesis of the atmosphere in Yaku-Island is affected by southern marine [*Nakamura et al.* 2013].

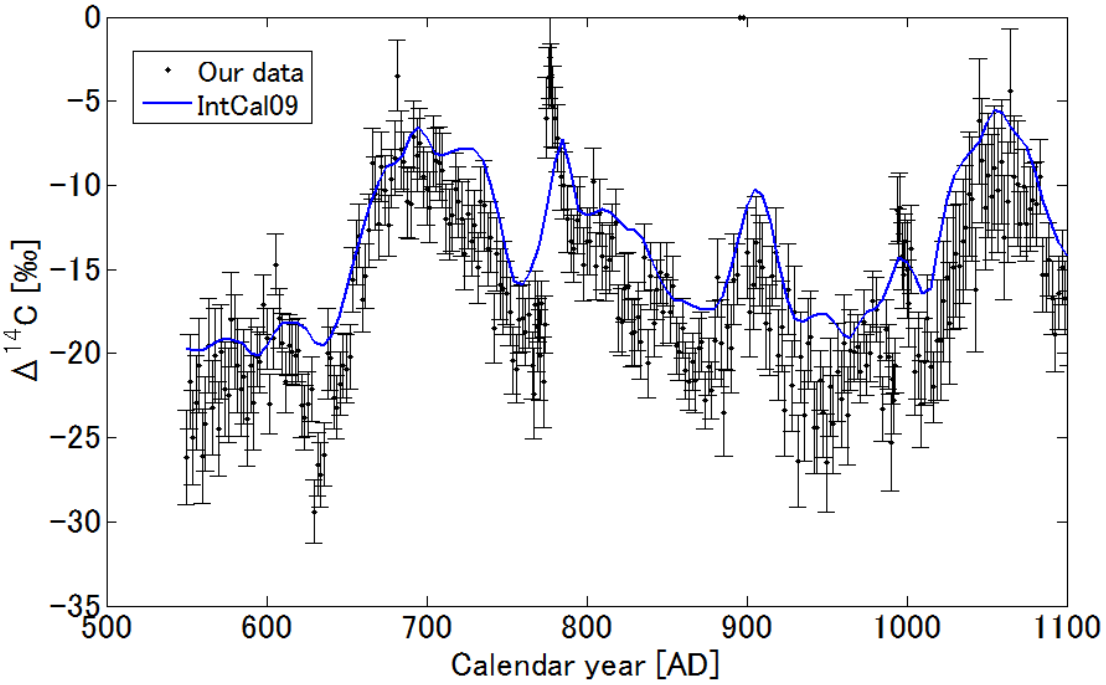

Figure A3: Comparison of our result with IntCal98 data. The vertical axis represents the ^{14}C content (by $\Delta^{14}C$), and the horizontal axis represents the calendar year. The dots show our measurement data and the blue line shows the IntCal98 data (AD 550–1101).

[11] ^{14}C age is expressed as "before present" (=BP) which means time before AD 1950.

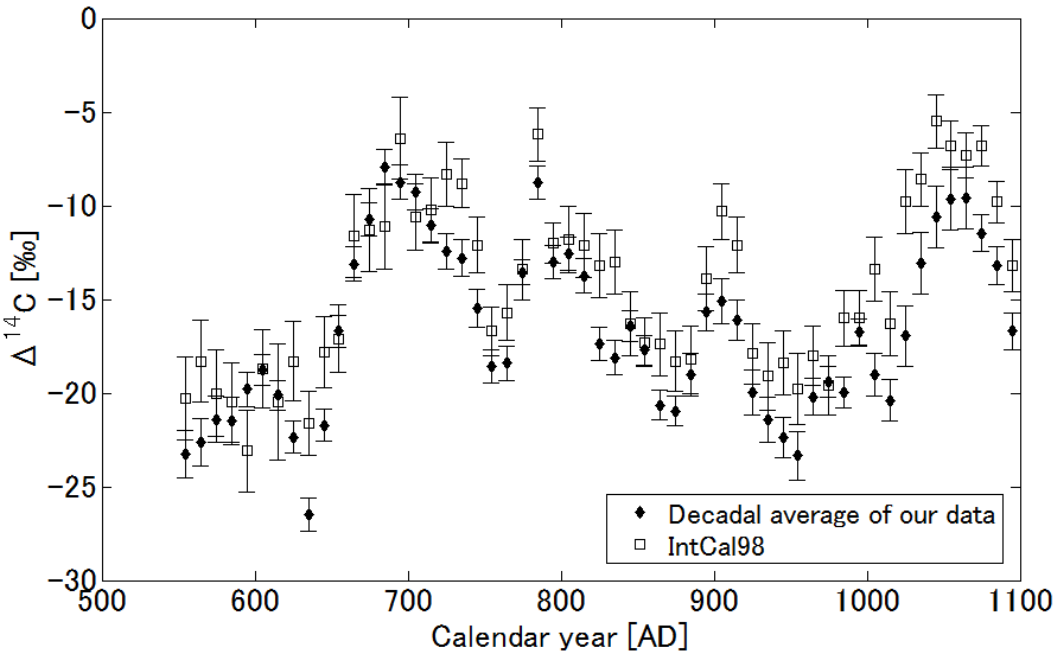

Figure A4: Comparison of decadal average of our result with IntCal98 data. The vertical axis represents the ^{14}C content (by $\Delta^{14}C$), and the horizontal axis represents the calendar year. Open squares show the IntCal98 data and filled diamonds show the decadal average of our biennual data from AD 550 to 1101.

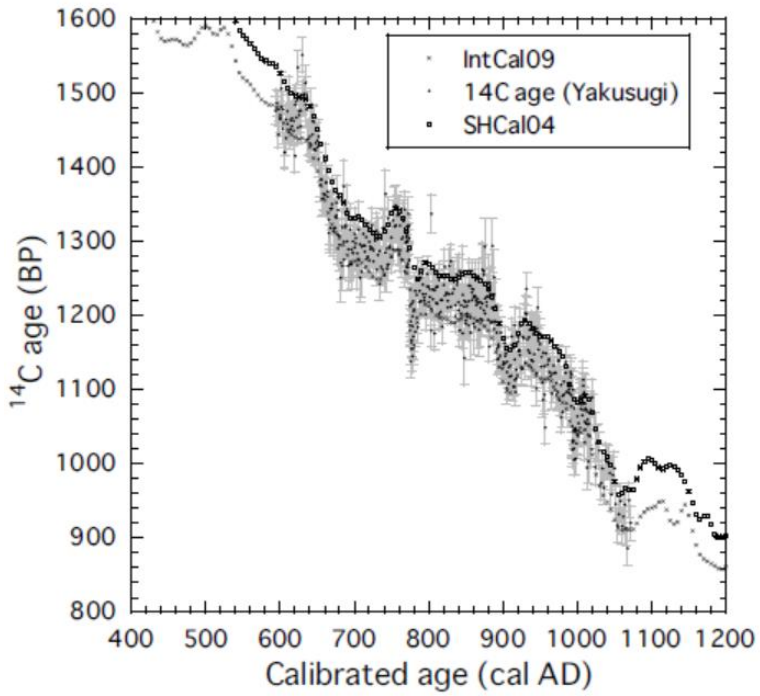

Figure A5: Comparison between ^{14}C ages of our tree rings from AD 589–1072, the IntCal09 and SHCal04 standard data sets. Our results locate between these two standard data sets. This graph is cited from *Nakamura et al.* [2013].

Acknoledgements

This work has been achieved by many supports. I would particularly like to express the deepest appreciation to my supervisor, Assosiate Prof. Kimiaki Masuda who gave me this work, many useful discussions, and warm encouragements. I would also like to express my gratitude to Prof. Yoshitaka Itow, Prof. Toshio Nakamura, and Prof. Kanya Kusano for giving insightful comments and suggestions.

I am deeply grateful to the CR laboratory staffs, Emeritus Prof. Yasushi Muraki, Prof. Hiroyasu Tajima, Associate Prof. Yutaka Matsubara, Associate Prof. Fumio Abe, Assistant Prof. Takashi Sako, Assistant Prof. Hiroaki Menjo, and Associate Prof. Takahiro Sumi (Osaka University) who gave me useful comments and discussions.

I would like to express my gratitude to Prof. Ilya Usoskin (University of Oulu) and Hiroko Miyahara (Musashino Art University) for useful discussions about the production rate of ^{14}C.

I would like to thank Prof. Katsuhiko Kimura (Fukushima University) for providing Yaku-14ANb sample and for dating the Yaku cedar sample tree rings by dendrochronology, and also thank Prof. Takumi Mitsutani (Nara National Research Institute for Cultural Properties) for providing the Hinoki sample and dating. I would like to thank Associate Prof. Fuyuki Tokanai and Assistant Prof. Kazuhiro Kato (Yamagata University) for the AMS measurement at Yamagata University. I also thank the members of center for chronological Research for their cooperation. Especially, Ms. Akiko Ikeda and Mr. Takahiro Yoshimitsu (graduate) helped my sample preparation, and Dr. Masataka Hakozaki gave me very useful comments about dendrochronology, and the collaboration research. I would like to thank Dr. Takahiro Aze (Tokyo Institute of Technology) to gave me the information about the growing of Yaku-cedar.

I would like to express my gratitude to Dr. Kentaro Nagaya (graduate) who was a C14 group member and taught me a lot of things like a sample treatment methods and useful discussions. I would like to thank the members of CR labolatory, especially thanks to my contemporaries Mr. Yuya Nagai, Mr. Kentaro Kawade and Mr. Hiroyoshi Uchida, and thanks to my roommates Ms. Choi Koun, Ms. Asami Suzuki, Ms. Eri Matsubayashi for an amusing conversation. I also thank Ms. Tomoyo Kainai for my office works. This work is supported by a Research Fellowship of the Japan Society for the Promotion of Science. Without their help, this thesis would not have been possible.

Finally I would like to offer my special thanks to my parents for their financial support, and very useful comments and discussions for my study. And my heartfelt appreciation goes to my husband.

References

1. Allen, J. Clue to an ancient cosmic-ray event? Nature 486, 473 (2012).
2. Anderson, E. C, et al., Radiocarbon from cosmic radiation. Science 105, 576-577 (1947).
3. Baker, D. N. in Space Weather: The Physics Behind a Slogan (eds Scherer, K., Fichtner, H., Heber, B. & Mall, U.) 3 (Lecture Notes in Physics, Vol. 656, Springer, 2004).
4. Barnard, L. & Lockwood, M. A survey of gradual solar energetic particle events. J. Geophys. Res. 116, A05103 (2011).
5. Barnard, L. et al. Predicting space climate change. Geophys. Res. Lett. 38, L16103 (2011).
6. Brakenridge, G. R. Core-collapse supernovae and the Younger Dryas/terminal Rancholabrean extinctions. Icarus 215, 101–106 (2011).
7. Burrows, A. Supernova explosions in the Universe. Nature 403, 727–733 (2000).
8. Castagnoli, G. & Lal, D. Solar modulation effects in terrestrial production of carbon-14. Radiocarbon 22, 133-158 (1980).
9. http://hea-www.harvard.edu/ChandraSNR/snrcat_gal.html (Chandra Supernova Remnant Catalog).
10. Crosby, N. B., Aschwanden, M. J. & Dennis, B. R. Frequency distributions and correlations of solar X-ray flare parameters. Solar Phys. 143, 275-299 (1993).
11. Cuntz, M., Saar, S. H. & Musielak, Z. E. On stellar activity enhancement due to interactions with extrasolar giant planets. Astrophys. J. 533, L151–L154 (2000).
12. Dall'Olmo, U. An additional list of Auroras from European sources from 450 to 1466 A.D. J. Geophys. Res., 84, 1525-1535 (1979).
13. Damon, P. E., Kaimei, D., Kocharov, G. E., Mikheeva, I. B. & Peristykh, A. N. Radiocarbon production by the gamma-ray component of supernova explosions. Radiocarbon 37, 599–604 (1995).
14. Damon, P. E. & Peristykh, A. N. Radiocarbon calibration and application to geophysics, solar physics, and astrophysics. Radiocarbon 42, 137–150 (2000).

15. Delaygue, G. & Bard, E. An Antarctic view of Beryllium-10 and solar activity for the past millennium. Clim. Dyn. 36, 2201 (2011).

16. Eicher, D. & Mordecai, D. Comet Encounters and Carbon 14. Astrophys. J. Lett. 761, L27, doi:10.1088/2041-8205/761/2/L27 (2013).

17. GEANT4. http://www.geant4.org/geant4.

18. Gibbons, G. W. & Werner, M. C. More medieval clues to cosmic-ray event. Nature 487, 432 (2012).

19. Green, D. A. A revised Galactic supernova remnant catalogue. Bull. Astr. Soc. India 37, 45–61 (2009).

20. Güttler, D. et al. Worldwide detection of a rapid increase of cosmogenic ^{14}C in AD 775. Nuclear Physics in Astrophysics VI, 19-24, poster, May 2013 (2013).

21. Hambaryan, V. V. & Neuhäuser, R. A galactic short gamma-ray burst as cause for the ^{14}C peak in AD 774/5. Mon. Not. R. Astron. Soc. 430, 32–36 (2013).

22. Horiuchi, K. et al. Ice core record of ^{10}Be over the past millennium from Dome Fuji, Antarctica: a new proxy record of past solar activity and a powerful tool for stratigraphic dating. Quat. Geochronol. 3, 253–261 (2008).

23. Hua, Q., Barbetti, M., Jacobsen, G. E., Zoppi, U. & Lawson, E. M. Bomb radiocarbon in annual tree rings from Thailand and Australia. Nucl. Instr. Meth. B 172, 359-365 (2000).

24. Hoyt, D. V. & Schatten, K. H. Group sunspot numbers: A new solar activity reconstruction. Sol. Phys. 181, 491-512 (1998).

25. Ip, W. H., Kopp, A. & Hu, J. H. On the star-magnetosphere interaction of close-in exoplanets. Astrophys. J. 602, L53–L56 (2004).

26. Iyudin, A. F. et al. Emission from ^{44}Ti associated with a previously unknown Galactic supernova. Nature 396, 142–144 (1998).

27. Katsuda, S., Tsunemi, H. & Mori, K. Is Vela Jr. a young supernova remnant? Adv. Space Res. 43, 895–899 (2009).

28. Keimatsu, M. A chronology of aurorae and sunspots observed in China, Korea and Japan, Part IV, Vol. 13 (Ann. Sci. College of Liberal Arts, Kanazawa University) (1973).

29. Konstantinov, B. P. & Kocharov, G. E. Astrophysical Events and Radiocarbon (NASACR-77812, ST-CMG-AC-10430, 1965).

30. http://cometography.com (G.W. Kronk's Cometography Web Site).

31. Lanza, A. F. Hot Jupiters and stellar magnetic activity. Astron. Astrophys. 487, 1163–1170 (2008).

32. LaViolette, P. A. Evidence for a solar flare cause of the Pleistocene mass extinction. Radiocarbon 53, 303–323 (2011).

33. Maehara, H. et al. Superflares on solar-type stars. Nature 485, 478–481 (2012).

34. Masarik, J. & Beer, J. An updated simulation of particle fluxes and cosmogenic nuclide production in the Earth's atmosphere. J. Geophys. Res. 114, D11103, doi.org/10.1029/2008JD010557 (2009).

35. McCormac, F. G. et al. SHCal southern hemisphere calibration, 0-11.0 cal kyr BP. Radiocarbon 46, 1087-1092 (2004).

36. McCracken, K. G., Dreschhoff, G. A. M., Zeller, E. J., Smart, D. F. & Shea, M. A. Solar cosmic ray events for the period 1561–1994: 1. Identification in polar ice, 1561–1950. J. Geophys. Res. 106, 21585–21598 (2001).

37. McCracken, K., McDonald, F., Beer, J., Raisbeck, G. & Yiou, F. A. Phenomenological study of the long-term cosmic ray modulation, 850–1958 AD. J. Geophys. Res. 109, A12103 (2004).

38. Melott, A. L. et al. Did a gamma-ray burst initiate the late Ordovician mass extinction? arXiv:astro-ph/0309415v3 (2004).

39. Melott, A. L. & Thomas, B. C. Causes of an AD 774–775 ^{14}C increase. Nature 491, E1–E2 (2012).

40. Menjo, H. et al. Possibility of the detection of past supernova explosion by radiocarbon measurement. in Proc.29th Int. Cosmic Ray Conf. Vol.2 (ed. Acharya, B. S.) 357–360 (Tata Institute of Fundamental Research, Mumbai, 2005).

41. Miyahara, H. et al. Cyclicity of solar activity during the Maunder Minimum deduced from radiocarbon content. Sol. Phys. 224, 317–322 (2004).

42. Miyahara, H. Solar Cycle during the Maunder and Spoerer Minima. Ph. D. thesis, Nagoya University, Nagoya, Japan (2005).

43. Miyahara, H., Masuda, K., Muraki, Y., Kitagawa, H. & Nakamura, T. Variation of solar cyclicity during the Spoerer Minimum. J. Geophys. Res. 111, A03103 (2006).

44. Miyahara, H., Yokoyama, Y. & Masuda, K. Possible link between multi-decadal climate cycles and periodic reversals of solar magnetic field polarity. Earth Planet. Sci. Lett. 272, 290-295 (2008).

45. Miyahara, H. et al. Is the sun heading for another Maunder minimum? Precursors of the grand solar minima. J. Cosmol. 8, 1970–1982 (2010).

46. Miyake, F., Nagaya, K., Masuda, K. & Nakamura, T. A signature of cosmic-ray increase in AD 774–775 from tree rings in Japan. Nature 486, 240–242 (2012).

47. Miyake, F., Masuda, K. & Nakamura, T. Another rapid event in the carbon-14 content of tree rings. Nat. Commun. 4:1748 doi:10.1038/ncomms2873 (2013).

48. Miyake, F., Masuda, K. & Nakamura, T. Lengths of Schwabe cycles in the 7th and 8th centuries indicated by precise measurement of carbon-14 content in tree rings. J. Geophys. Res. in press.

49. Motizuki, Y. et al. An Antarctic ice core recording both supernovae and solar cycles. Preprint at http://arXiv.org/abs/0902.3446 (2009).

50. Nagaya, K. et al. Variation of the Schwabe cycle length during the grand solar minimum in the 4th century BC deduced from radiocarbon content in tree rings. Sol. Phys. 280, 223-236 (2012).

51. Nagaya, K. Variation of the Schwabe cycle length during the grand solar minimum in the 4th century BC deduced from radiocarbon content in tree rings, Ph. D. thesis, Nagoya University, Nagoya, Japan (2012).

52. Nakamura, T., Nakai, N. & Ohishi, S. Applications of environmental ^{14}C measured by AMS as a carbon tracer. Nucl. Instrum. Methods B 29, 355–360 (1987).

53. Nakamura, T., E. Niu, H. Oda, A. Ikeda, M. Minami, H. Takahashi, M. Adachi, L. Pals, A. Gottdang, and N.Suya, The HVEE Tandetron AMS system at Nagoya University, *Nucl. Instrum. Methods B*, **172**, 52-57 (2000).

54. Nakamura, T., 加速器質量分析（AMS）による環境中およびトレーサ放射性同位体の高感度測定, *Radioisotopes*, **52**, 144-171 (2003) in Japanese.

55. Nakamura, T. *et al.* High precision ^{14}C measurements and wiggle-match dating of tree rings at Nagoya University. *Nucl. Instr. Meth. B* **259,** 408–413 (2007).

56. Nakamura, T. et al. Radiocarbon ages of annual rings from Japanese wood: Evident age offset based on IntCal09. Radiocarbon 55, 408–413 (2013).

57. Naker, E. Short-Hard Gamma-ray bursts. Phys. Rep. 442, 166-236 (2007).

58. Owens, M. J., Lockwood, M., Barnard, L. & Davis, C. J. Solar cycle 24: Implications for energetic particles and long-term space climate change. Geophys. Res. Lett. 38, L19106 (2011).

59. Parkenier, D. W., Xu, Z., & Jiang, Y. Archaeoastronomy in East Asia : Historical Observational Records of Comets and Meteor Showers from China, Japan & Korea. Cambria Press (2008).

60. Piro, L. Astrophysics: Short-burst sources. Nature, 437, 822-823 (2005).

61. Reimer, P. J. et al. IntCal04 terrestrial radiocarbon age calibration, 0-26 cal kyr BP. Radiocarbon 46, 1029–1058 (2004).

62. Reimer, P. J. et al. IntCal09 and marin09 radiocarbon age calibration curves, 0–50,000 years cal BP. Radiocarbon 51, 1111–1150 (2009).

63. Rood, R. T., Sarazin, C. L., Zeller, E. J. & Parker, B.C. X- or γ -rays from supernovae in glacial ice. Nature 282, 701-703 (1979).

64. Sato, T., Yasuda, H., Niita, K., Endo, A. & Sihver, L. Development of PARMA: PHITS based Analytical Radiation Model in the Atmosphere. Radiat. Res. 170, 244–259 (2008).

65. Schaefer, B. E., King, J. R. & Deliyannis, C. P. Superflares on ordinary solar-type stars. Astrophys. J. 529, 1026–1030 (2000).

66. Schwabe, M. T. Die Sonne. Asron. Nachr. 20, 283-288, doi: 10.1002/asna.18430201706 (1843).

67. Schweingruber, F. H. Tree Rings. –Basics and Applications of Dendrochronology–. D. Reidel Publishing Company (1987).

68. Solanki, S. K., Usoskin, I. G., Kromer, B., Schuessler, M. & Beer, J. An unusually active Sun during recent decades compared to the previous 11,000 years. Nature 431, 1084–1087 (2004).

69. Stephenson, F.R. & Clark, D.H. Historical Superovas. Scientific American, 234, 100-107 (1976).

70. Stephenson, F. R. A revised catalogue of pre-telescopic galactic novae and supernovae. Q. J. R. Astr. Soc. 17, 121–138 (1976).

71. Storm, R. G. "Guest stars", sample completeness and the local supernova rate. Astron. Astrophys. 288, L1-L4 (1994).

72. Struck, C., Cohanim, B. E. & Wilson, L. A. Continuous and burst-like accretion on to substellar companions in Mira winds. Mon. Not. R. Astron. Soc. 347, 173–186 (2004).

73. Stuiver, M. & Polach, H. A. Discussion: reporting of ^{14}C data. Radiocarbon 19, 355–363 (1977).

74. Stuiver, M., & Quay, P. D. Changes in atmospheric carbon-14 attributed to a variable Sun, Science 207, 11-19 (1980).

75. Stuiver, M., & Braziunas, T. F. Atmospheric ^{14}C and century-scale solar oscillations, Nature 338, 405-408 (1989).

76. Stuiver, M. et al. INTCAL98 Radiocarbon age calibration, 24,000–0 cal BP. Radiocarbon 40, 1041–1083 (1998a).

77. Stuiver, M., Reimer, P. J. & Braziunas, T. F. High-precision radiocarbon age calibration for terrestrial and marine samples. Radiocarbon 40, 1127–1151 (1998b).

78. Takahashi, Y. et al. Variation of C-14 concentrations of single-yr tree rings at the rapid change in 2600-yrBP. in Proc. 30th Int. Cosmic Ray Conf. Vol. 1 (ed. Caballero, R.) 673–676 (Universitad nacional autonoma de Mexico, 2007).

79. Telezhinsky, I. A new model for Vela Jr. supernova remnant. Astropart. Phys. 31, 431–436 (2009).

80. Thomas, B. C., Melott, A. L., Arkenberg, K. R. & Snyder B.R. II. Terrestrial effects due to possible astrophysical sources of an AD 774-775 increase in ^{14}C production. Geophys. Res. Lett. 40, 1-4, doi: 10.1002/grl.50222 (2013).

81. Usoskin, I. G., Solanki, S. K., Kovaltsov, G. A., Beer, J. & Kromer, B. Solar proton events in cosmogenic isotope data. Geophys. Res. Lett. 33, L08107, doi.org/10.1029/2006GL026059 (2006a).

82. Usoskin, I. G., Solanki, S. K. & Korte, M. Solar activity reconstructed over the last 7000 years: The influence of geomagnetic field changes. Geophys. Res. Lett. 33, L08103 (2006b).

83. Usoskin, I. G., Solanki, S. K., & Kovaltsov, G. A. Grand minima and maxima of soar activity: new observational constraints. Astron. Astrophys. 471, 301-309 (2007).

84. Usoskin, I. G. & Kovaltsov, G. A. Occurrence of extreme solar particle events: assessment from historical proxy data. Astrophys. J. 757, 92, doi:10.1088/0004-637X/757/1/92 (2012).

85. Usoskin, I. et al. The AD775 cosmic event revisited: the Sun is to blame. A&A 552, L3, doi: 10.1051/0004-6361/201321080 (2013).

86. Voss, H., Kurths, J. & Schwarz, U. Reconstruction of grand minima of solar activity from $\Delta^{14}C$ data: Linear and nonlinear signal analysis. J. Geophys. Res. 101, 15,637-15,643 (1996).

87. Willson, L. A. & Struck, C. Hot flashes on Miras? J. Am. Assoc. Variable Star. Obs. 30, 23–25 (2001).

88. Wolff, E. W. et al. The Carrington event not observed in most ice core nitrate records. Geophys. Res. Lett. 39, L08503, doi: 10.1029/2012GL051603 (2012).

89. Yasue, K. *et al.* Dendroclimatological study of *Picea glehnii* growing in the Teshio experimental forest of Hokkaido University. *Bulletin of the Hokkaido University forests*, **51(2)**, 243-266 (1994).

90. Yau, K., Stephenson, F. & Willis, D. A catalogue of auroral observations from China, Korea and Japan (193 B.C. - A.D. 1770), Technical Report RAL-TR-95-073, Chilton, Oxfordshire: Rutherford Appleton Laboratory (1995).